

Electronic spectroscopy  
of metal terminated carbon chains.

**Inauguraldissertation**

zur

Erlangung der Würde eines Doktors der Philosophie

vorgelegt der

Philosophisch-Naturwissenschaftlichen Fakultät

der Universität Basel

von

Egor A. Chasovskikh

aus Novosibirsk, Russland

Basel, 2008

Genehmigt von der Philosophisch-Naturwissenschaftlichen Fakultät

auf Antrag von

Prof. Dr. John P. Maier und Prof. Dr. Markus Meuwly

Basel, den 12. November 2008

Prof. Dr. Eberhard Parlow

Dekan

To my parents

# Acknowledgments

I would like to thank Prof. John P. Maier for giving me the opportunity to work in his group. The excellent working environment and the essential resources to learn and do research during the period of my study are greatly acknowledged. I would also like to thank Prof. Markus Meuwly for his courteous agreement to act as my co-referee.

I indeed enjoyed the time when Prof. Alan Knight was on his sabbatical in Basel. I am enchanted by his openness and willingness to spend his time thinking on your question.

I am also particularly indebted to Dr. Evan Johnowitz for his supervision and contribution to preparation and presentation of scientific results described in this work.

My special thanks are directed to Dr. Corey Rice for his unlimited friendliness, patience, permanent willingness to help, and perfect English.

I am grateful to my colleagues and friends for providing a friendly working environment and good team spirit.

I am also grateful to the people who were technically involved in the experiment for their effort and patience. My special thanks are directed to Dieter Wild, Grischa Martin, Franz Haefeli from the mechanical workshop for their service and skills in constructing sophisticated technical devices. I express my gratitude to Georg Holderied for his extraordinary skills in constructing electronic devices. I also feel indebted to Jacques Lecoultre for synthesizing of exotic substances. And I would like to thank Esther Stalder and Daniela Tischauser for their guidance through the chaos and confusions of living in foreign country.

EGOR CHASOVSKIKH

Basel, Switzerland  
November 12, 2008

# Contents

<b>Acknowledgments</b>	<b>iv</b>
<b>Chapter 1 Introduction</b>	<b>1</b>
1.1 Motivation. . . . .	1
1.2 Molecular nanowires . . . . .	2
1.3 The astronomical relevance of spectroscopical research. . . . .	4
1.3.1 Stars. . . . .	6
1.3.2 Interstellar gas. . . . .	10
1.3.3 Interstellar Dust. . . . .	11
1.3.4 Nebulas. . . . .	11
1.4 Diffuse Interstellar Bands. . . . .	13
1.4.1 The structure of DIB. . . . .	15
1.4.2 Doppler splitting. . . . .	16
1.4.3 Reddening. . . . .	17
1.4.4 Families of DIB. . . . .	18
1.5 Review of the proposed carriers. . . . .	19
1.5.1 Solid particle-not favorite carrier anymore. . . . .	19
1.5.2 Gas-phase molecules. . . . .	20
1.5.3 Linear carbon chains. . . . .	22
1.5.4 Polycyclic Aromatic Hydrocarbons - PAHs. . . . .	23
1.5.5 Fullerenes. . . . .	24
1.6 Conclusion. . . . .	24

<b>Chapter 2</b>	<b>Experimental Setup</b>	<b>26</b>
2.1	Introduction . . . . .	26
2.2	Laser Induced Fluorescence Concept . . . . .	26
2.3	Overview of the experiment . . . . .	28
2.4	Molecular sources . . . . .	31
2.4.1	Discharge source . . . . .	31
2.4.2	Laser ablation source . . . . .	32
2.4.3	Free jet expansion . . . . .	39
2.4.4	Ablation source design . . . . .	45
2.5	Optical system . . . . .	48
2.5.1	Baffle system . . . . .	48
2.5.2	Optical system . . . . .	49
2.5.3	Radiation sources . . . . .	52
2.5.4	Wavelength calibration . . . . .	52
2.6	Data acquisition. . . . .	53
2.7	Expansion temperature profile . . . . .	54
2.8	Molecular beam number density . . . . .	58
<b>Chapter 3</b>	<b>Preliminary experiments</b>	<b>61</b>
<b>Chapter 4</b>	<b>Vibrational analysis of the <math>\tilde{C} \ ^2B_2 \leftarrow \tilde{X} \ ^2A_1</math> electronic transition of AlC<sub>2</sub></b>	<b>70</b>
4.1	Introduction . . . . .	70
4.2	Theoretical calculation . . . . .	70
4.3	Experimental . . . . .	72
4.4	Results . . . . .	73
4.5	Conclusion . . . . .	77
<b>Chapter 5</b>	<b>The further investigation of the vibronic spectrum observed in <math>A \ ^1\Pi \leftarrow X \ ^1\Sigma^+</math> electronic transition AlCCH</b>	<b>80</b>
5.1	Introduction . . . . .	80

5.2	Theoretical calculation . . . . .	81
5.3	Experiment. . . . .	81
5.4	Results. . . . .	82
5.5	Discussion . . . . .	85
5.6	Conclusion. . . . .	89
<b>Chapter 6</b>	<b>Electronic spectrum of the AlC<sub>2</sub> radical</b>	<b>90</b>
<b>Chapter 7</b>	<b>Electronic spectra of the MgC<sub>4</sub>H and MgC<sub>6</sub>H radical</b>	<b>95</b>
<b>Chapter 8</b>	<b>Rotationally resolved <math>A \ ^2\Pi - X \ ^2\Sigma^+</math> electronic transition of MgC<sub>4</sub>D</b>	<b>100</b>
	<b>Bibliography</b>	<b>106</b>
	<b>Curriculum Vitae</b>	<b>114</b>

# Chapter 1

## Introduction

### 1.1 Motivation.

Metal containing carbon chains have proven themselves interesting in a number of different areas. Carbon chains, in general, have been of astrophysical interest ever since Douglas [1] first proposed them as the carriers of the diffuse interstellar bands in 1977.

In more terrestrial applications, metal capped carbon chains are relevant in industrial purposes, both as nanowires and in the fields of catalysis. Thus their spectroscopic study neatly ties together the fundamental study of spectroscopy with applied materials research: a unique and powerful combination. This thesis thus concerns itself with understanding the most basic metal capped carbon species (3-6 atoms) containing aluminum and magnesium atoms, which may make up the simplest molecular wires.

Electronic structure ultimately determines the structural, physical, and chemical properties of an molecules and solids. Consequently, studying the size evolution of various cluster properties, such as equilibrium geometries, stability, bonding nature, and ionization potentials is an attractive and challenging problem, which takes on particular importance in the fields of heterogeneous catalysis, surface chemistry, and solid-state physics.



## 1.2 Molecular nanowires

The miniaturization of electronics has naturally led toward the investigation of single molecules as components for electronic devices, opening up the field known as "molecular electronics". Compared to even the smallest possible silicon circuits, these molecular structures are on a scale still hundreds of times smaller. Molecular wires, as used in molecular- and opto-electronics, may one day replace siliconbased wires in semiconductor devices,[2] thus one-dimensional carbon chains are ideal model systems for studying electronic structure, due to their potential application in nanoscience and molecular device design. [3]

While still in the early stages of research, single molecule electronics have already been found to perform a number of tasks previously associated with semiconductor materials. [4, 5] The simplest electronic device, the one-dimensional wire, has the basic motif of a conjugated  $\pi$ -bonding system, allowing the conduction of electricity [6] as an electrical field electively mixes the ground and excited states of the molecule. Thus promotion of an electron across the band-gap of the free molecule plays a crucial role, and it is this fundamental parameter (band-gap energy) that is essential to the behavior of the molecular device.

Optical spectroscopy offers a straightforward method to measure this bandgap, [7, 8] as well as the ionization potentials and electron affinities of the wires, in addition to their bonding and physical structures. The aim of the research program is to elucidate how the electronic structure of prototypical molecular electronic components evolve when bound to a metal atom, as in the form  $MC_n$ , where M represents the metal capping the carbon chain. This allows detailed studies of the organic-inorganic conducting junction, providing a link between the applied research in molecular electronics and the simplified models of theorists in the field, thereby facilitating the development of "advanced materials". The trends observed in the spectra demonstrate the effect of binding various systems to metal atoms and how it alters the electronic structure of the  $\pi$ -conjugated systems. Meanwhile, spectroscopic investigations of small metal clusters have significantly enhanced the level of understanding in several areas of chemistry, including chemical bonding and

the catalytic behavior of certain metals. [9, 10] The availability of laser vaporization sources has stimulated many studies on small metal clusters, and the diversity of their electronic structures has been the subject of several experimental and theoretical studies.

Using a variety of custom developed techniques the electronic spectra of various metal containing carbon chain radicals and ions are to be examined for the first time. This thus neatly combines the application of molecular spectroscopy, a field traditionally associated with fundamental research, to applied molecular electronics. Earlier the spectra of the  $\text{H}(\text{CC})_n\text{H}$  chains were measured with increasing size and the  $\pi - \pi$  absorption maxima, corresponding to the HOMO-LUMO gap, tends toward a limit [11], indicating that the infinite chain is not a conductor, but an insulator. This behavior was also observed with nitrogen terminated nanochains, such as  $\text{NC}_{16}\text{N}$ , where the species also exhibits bond alternation throughout the chain [3]. Further studies on sulfur capped chains  $\text{H}(\text{CC})_n\text{S}$ , where even bond lengths are distributed, demonstrated no tendency toward a band-gap limit. [12]

Thus, contrary to the pure and nitrogen terminated wires, sulfur terminated chains are predicted to be good conductors. The differing valencies of the non-metallic endcaps in the sulfur versus nitrogen terminated wires is clearly responsible: therefore there is something not well understood regarding how the bonding in these systems varies upon attachment to a metal end-cap (organic-inorganic junction). This will be examined by bonding metal atoms such as Mg, Fe and Al to  $\text{C}_n$  and  $\text{C}_n\text{H}$  chains.

The fact that aluminum has only three valence electrons per atom makes it an appropriate candidate for theoretical treatment, as opposed to transition metal clusters where the density of states increases to the point that accurate molecular orbital calculations are impractical. After an understanding of Al clusters are understood, more complicated and larger metal species can be investigated, such as  $\text{FeC}_n$ .

Apart from clusters of alkali metals (Na and K in particular), aluminium clusters are perhaps the most extensively examined simple metal systems: such studies include experimental measurements of ionization potentials, electron affinities, photoelectron spectra, polarizabilities, and dissociation energies.[13, 14, 15] Aluminum is of particular interest in cluster physics due to the appearance of so called "magic clusters", which are chemically

inert and exhibit closed shell structures with relatively high electron affinities. Well-known examples of magic clusters include  $C_{60}$  and  $Al_{13}^-$ . The fact that aluminum has only three valence electrons per atom makes it an appropriate candidate for theoretical treatment, as opposed to transition metal clusters where the density of states increases to the point that accurate molecular orbital calculations are impractical.

The ablation products have already been shown to include abundant clusters of targeted species, such as carbon and aluminum. Spectroscopic trends will be revealed which have important implications on the band structure of metal containing clusters, which is of considerable interest in the formation of thin films, nanoparticles and nanotubes and thus provide the crucial steps toward understanding their practical application.

### **1.3 The astronomical relevance of spectroscopical research.**

The spectroscopy itself offers a probe not only in the electronic and physical structures of the studied species themselves, but also a means for their nonterrestrial identification, along with the conditions surrounding these radicals when found in flames, plasmas and interstellar space.

The Big Bang theory describes the universe as having formed from a tremendous explosion. The matter and energy released from this explosion evolved into the present stars and galaxies. Edwin Hubble provided the foundation for the Big Bang theory by showing that the universe is expanding from a common origin. This theory, in turn, spawned an analogous theory called the Big Crunch theory, which proposes that gravity in a closed universe will eventually pull all this material back together to recreate the original massive dense object. When scientist looked for evidence to support the Big Crunch theory, what they discovered was that the stars and galaxies instead of slowing down were actually accelerating outward from the origin. As a result, the existence of invisible dark matter, whose gravitational force caused this acceleration, was theorized. In order to understand the structure of the universe, it is important to understand the basic elements the universe consists of. Besides the stars, the interstellar medium itself

has a complicated structure. It consists of an extremely dilute (by terrestrial standards) mixture of ions, atoms, molecules, larger dust grains, cosmic rays, and (galactic) magnetic fields [16]. The matter consists of about 99% gas and 1% dust by mass. Densities range from a few thousand to a few hundred million particles per cubic meter with an average value in the Milky way galaxy of a million particles per cubic meter. As a result of primordial nucleosynthesis, the gas is roughly 90% hydrogen and 10% helium by number of nuclei, with additional heavier elements ("metals" in astronomical parlance) present in trace amounts.

The interstellar medium ISM plays a crucial role in astrophysics precisely because of its intermediate role between stellar and galactic scales. Stars form within the densest regions of the ISM, molecular clouds, and replenish the ISM with matter and energy through planetary nebulae, stellar winds, and supernovae. This interplay between stars and the ISM helps determine the rate at which a galaxy depletes its gaseous content, and therefore its lifespan of active star formation. The interstellar gas is more or less ionized by cosmic rays and electromagnetic radiation, therefore it strongly interacts with the magnetic fields. The magnetic field effects the ions which pass this influence through collision to neutral atoms and dust particles. Indeed, these particles themselves can be charged due to UV radiation or the attachment of electrons, and thus the magnetic field can effect them directly. Cosmic rays and electromagnetic radiation are absorbed by gas and dust particles, heating them and causing ionization. Interstellar gas and dust then emit the electromagnetic radiation from long wave radio frequency region to hard gamma-wave radiation.

In the ISM the cosmic rays present are capable of ionizing many of the gas molecules present. Thus the interaction of the dust particles and gas molecules found in the ISM with the cosmic rays and magnetic fields also present plays a significant role in the large scale dynamics observed. It is interesting to note that the interstellar gas, which contains a variety of ionic and neutral species, at the same time can increase the magnetic field present due to its participation in galactic rotation. Thus, the cosmic rays can effect the magnetic fields found in the ISM, which in its own way, will lead to the perturbation of itself.

The other source of perturbation is when the stars, originally formed from interstellar gas, return a portion of mass back to the interstellar medium. As the result of this exchange the interstellar medium becomes rich by heavy elements, usually produced in the stars core. The stars, as well, supply the interstellar medium with electromagnetic radiation and cosmic rays (especially through supernova explosion). When matter is ejected into interstellar medium, the hot gas affects ionization processes in the ISM and its dynamics as well.

Speaking about interstellar medium next objects one should define:

Stars.

Nebulas

Interstellar Gas.

Interstellar Dust.

### **1.3.1 Stars.**

A star begins as a collapsing cloud of material composed primarily of hydrogen, along with helium and trace amounts of heavier elements. Once the stellar core is sufficiently dense, some of the hydrogen is steadily converted into helium through the process of nuclear fusion. In astronomy, stellar classification is based initially on photospheric temperature and its associated spectral characteristics. There are two main classification system. The first is the one-dimensional Harvard classification system, where physically, the classes indicate the temperature of the star's atmosphere and are normally listed from hottest to coldest, as is done in the Table 1.1.

The mass, radius, and luminosity listed for each class are appropriate only for stars on the main sequence portion of their life cycle and so are not appropriate for red giants. The spectral classes O through M are subdivided by Arabic numerals (09). For example, A0 denotes the hottest stars in the A class and A9 denotes the coolest ones. The Sun is classified as G2. Our Sun itself is yellow-white. It is sometimes called a yellow star (spectroscopically, relative to Vega), and may appear yellow or red (viewed through the

Class	Temperature K	Conventional color	Mass (solar masses)	Radius (solar radius)	Luminosity	Hydrogen lines	% of all % Main Sequence star
O	30,000–60,000 K	blue	64 $M_{\odot}$	16 $R_{\odot}$	1,400,000 $L_{\odot}$	Weak	0.00003 %
B	10,000–30,000 K	blue white	18 $M_{\odot}$	7 $R_{\odot}$	20,000 $L_{\odot}$	Medium	0.13 %
A	7,500–10,000 K	white	3.1 $M_{\odot}$	2.1 $R_{\odot}$	40 $L_{\odot}$	Strong	0.6 %
F	6,000–7,500 K	yellowish white	1.7 $M_{\odot}$	1.4 $R_{\odot}$	6 $L_{\odot}$	Medium	3 %
G	5,000–6,000 K	yellow	1.1 $M_{\odot}$	1.1 $R_{\odot}$	1.2 $L_{\odot}$	Weak	7.6 %
K	3,500–5,000 K	orange	0.8 $M_{\odot}$	0.9 $R_{\odot}$	0.4 $L_{\odot}$	Very weak	12.1 %
M	2,000–3,500 K	red	0.4 $M_{\odot}$	0.5 $R_{\odot}$	0.04 $L_{\odot}$	Very weak	76.45 %

Table 1.1: The Harvard spectral classification. The Conventional color descriptions are traditional in astronomy, and represent colors relative to Vega, a star that is perceived as white under naked eye observational conditions, but which magnified appears as blue. The Apparent color [17] descriptions is what the observer would see if trying to describe the stars under a dark sky without aid to the eye, or with binoculars.

atmosphere), or appear white (viewed when too bright for the eye to see any color). Astronomy images often use a variety of exaggerated colors partially founded in faint light conditions observations, partially in conventions. But the Sun’s own intrinsic color is white (aside from sunspots), with no trace of color, and closely approximates a black body of 5780 K . This is a natural consequence of the evolution of our optical senses: the response curve that maximizes the overall efficiency against solar illumination will by definition perceive the Sun as white.

Another classification system (Yerkes spectral classification Figure 1.1) is based on spectral lines sensitive to stellar surface gravity, which is related to luminosity, as opposed to the Harvard classification which is based on surface temperature. Later, in 1953, after some revisions of the list of standard stars and classification criteria, the scheme was named MK [18]. Because the radius of a giant star is much larger than a dwarf star, while their masses are roughly comparable, the gravity and thus the gas density and pressure on the surface of a giant star are much lower than for a dwarf. These differences manifest themselves in the form of luminosity effects which affect both the width and the intensity of the spectral lines which can then be measured. Denser stars with higher surface gravity will exhibit greater pressure broadening of spectral lines.

The condensation of gas into a star is accompanied by its considerable temperature increase and continues until the balance between the gravitational attraction and the hot gas pressure is reached. In the 19th century Lord Kelvin discovered that the heat produced by gravitational compression would be sufficient for our Sun to radiate with the current

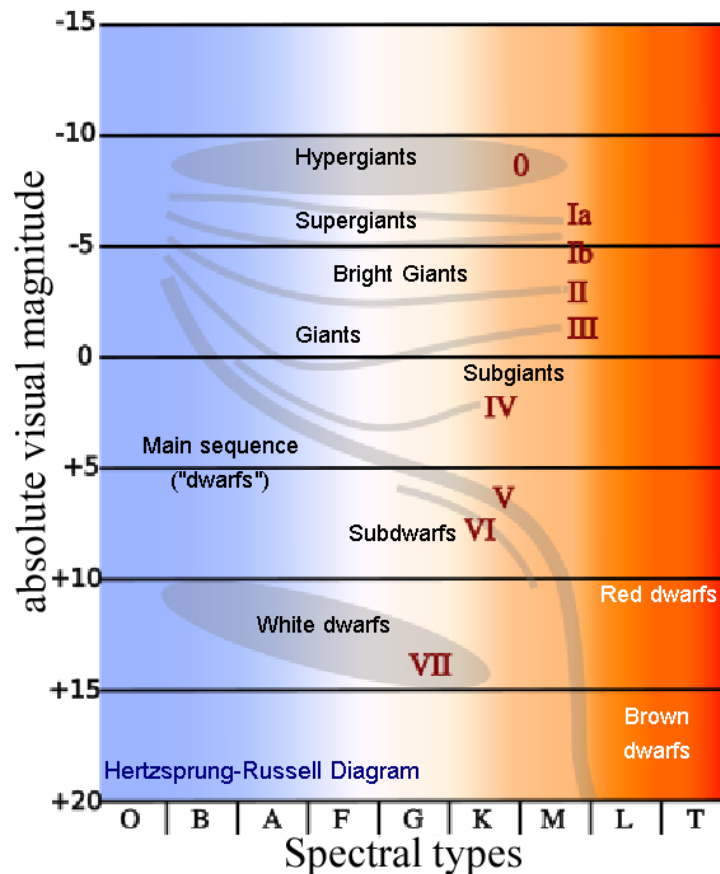


Figure 1.1: Yerkes spectral classification.

rate for no more than 1 million years. Nevertheless, there was already much evidence that the Sun is several billion years old and did not experience any dramatic changes of its parameters during this time. This problem, known as Kelvins paradox, was solved in the 20th century, when the missing source of energy was found. The solution was nuclear reactions, which are responsible for energy production in stars. Stars consist mostly of hydrogen, and during 90% of their lifetimes the conversion of it into helium acts as an energy source. Other nuclear reactions need higher temperatures and therefore occur only at the last stage of the stars life. After hydrogen in the core region is completely exhausted, the star contracts, and new reactions can start due to an increase in temperature. The smallest mass possible for a star is about 8% that of the Sun (80 times the mass of the planet Jupiter), otherwise nuclear reactions do not take place. Objects with less than critical mass shine only dimly and are termed brown dwarfs or a large planet(Figure 1.2).

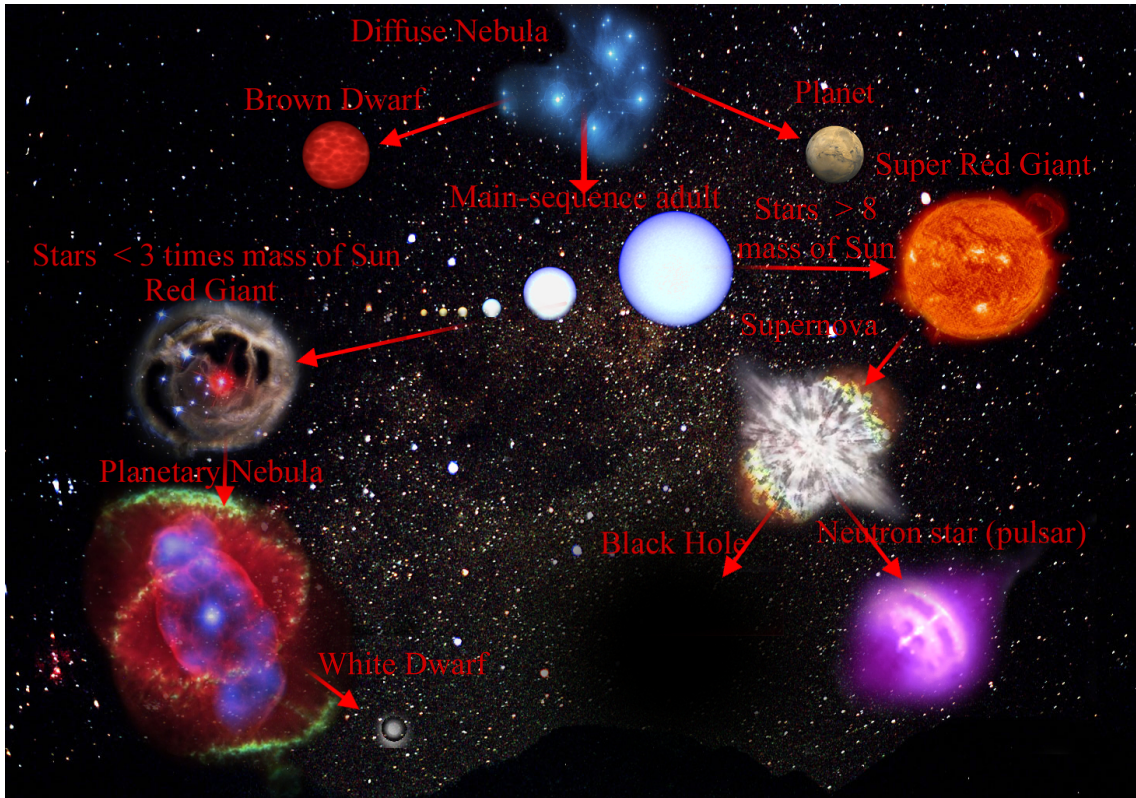


Figure 1.2: Life Cycle of a Star. Stars are born in nebulae. Huge clouds of dust and gas collapse under gravitational forces, forming protostars.

Stars are born in nebulae, when huge clouds of dust and gas collapse under gravitational forces, forming protostars. These young stars undergo further collapse, forming main sequence stars.

Stars expand as they grow old. As the core runs out of hydrogen and then helium, the core contracts and the outer layers expand, cool, and become less bright. This is a red giant or a red super giant (depending on the initial mass of the star). It will eventually collapse and explode. Its fate is determined by the original mass of the star; it will become either a black dwarf, neutron star, or black hole. A star like the Sun swells up into a red giant, before losing its outer layers as a Planetary Nebula and finally shrinking to become a white dwarf.



### 1.3.2 Interstellar gas.

It is considered that only two chemical elements were produced as a result of the Big Bang, namely hydrogen and helium. They are still the two most common elements in the Universe, which can be seen in Figure 1.3 where the relative cosmic abundances of elements are plotted on a logarithmic scale [19]. This information about elements in the ISM was obtained spectroscopically. In the case of our galaxy (Milky Way) only 10 % of the mass of our galaxy exists in the form of gas; dust is present in about 0.1 % and the rest 90 % is in stars. Stars can thus be considered as giant space factories of the chemical elements heavier than He.

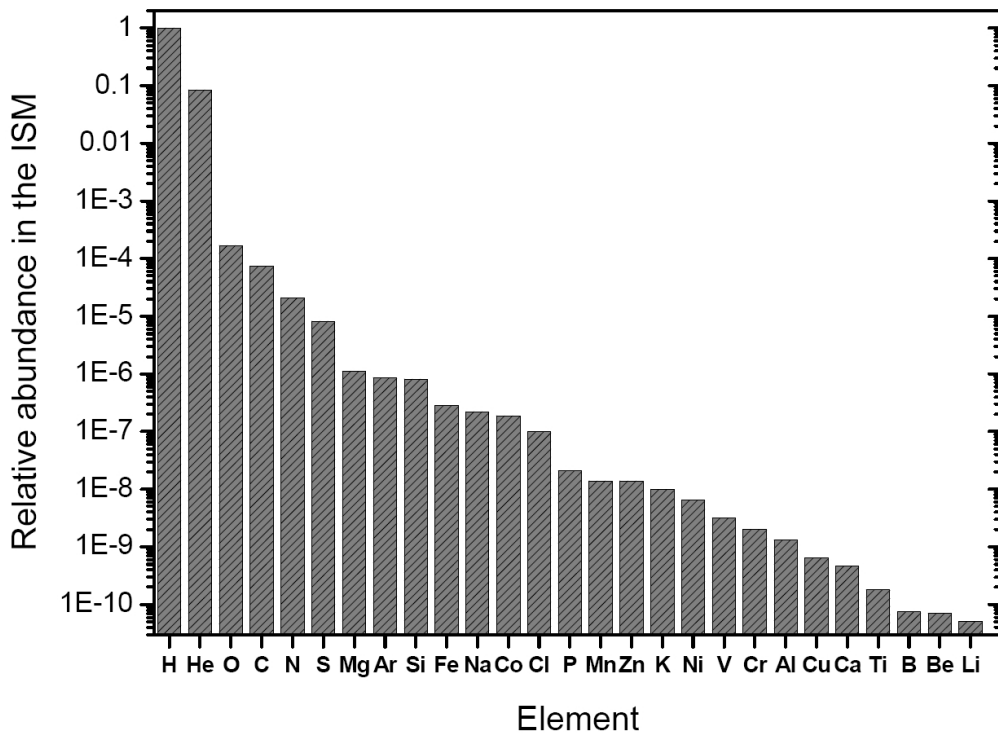


Figure 1.3: Relative abundances of elements in the ISM (Interstellar Medium) [19]). The bar chart is plotted in logarithmic scale, assuming that the abundance of H is 1. Only upper estimates are available for Co, V, Cr and Be.

### 1.3.3 Interstellar Dust.

Cosmic dust was once solely an annoyance to astronomers, as it obscures objects they wish to observe. When infrared astronomy began, those so-called annoying dust particles were observed to be significant and vital components of astrophysical processes. For example, cosmic dust can drive mass loss when a star is nearing the end of its life, playing a part in the early stages of star and planets formation [20]. In our own solar system, dust plays a major role in the zodiacal light, Saturn's B Ring spokes, the outer diffuse planetary rings in Jupiter, Saturn, Uranus and Neptune, the resonant dust ring of the Earth, and comets.

### 1.3.4 Nebulas.

Another fascinating astronomical objects are nebulas. The notion nebula was invented around 200 years ago, when astronomers realized that there are some other object beside stars and comets at the sky. These objects, due to their hazy appearance, were called nebula(from Latin: "mist" ). The French astronomer Charles Messier, in order to make his comet observation easy, made the first catalog of those objects. The first version of Messier's catalogue contained 45 objects and was published in 1774 in the journal of the French Academy of Sciences in Paris. By the time the final version of the catalogue was published in 1781, the list of Messier objects had grown to 103. On several different occasions between 1921 and 1966, astronomers and historians discovered evidence of another seven deep-sky objects that were observed either by Messier or his friend and assistant Pierre Mechain shortly after the final version was published. These seven objects, M104 through M110, are accepted by many astronomers as "official" Messier objects. The objects' designations, from M1 to M110, are still in use by professional and amateur astronomers today. Another astronomer, William Herschel, increased the number of such object by above two thousand, and he was the first who distinguish different from his point of view nebulas.

Many nebulae form from the gravitational collapse of diffuse gas in the ISM. As the material collapses under its own weight, massive stars may form in the center, and their

ultraviolet radiation ionizes the surrounding gas, making it visible at optical wavelengths. An example of this type of nebula is the Rosette Nebula or the Pelican Nebula. The size of these nebulae, known as HII regions, varies depending on the size of the original cloud of gas, and the number of stars formed can vary too. As the sites of star formation, the formed stars are sometimes known as a young, loose cluster.

Most nebulae can be described as diffuse nebulae, which means that they are extended and contain no well-defined boundaries [21]. In visible light these nebulae may be divided into emission nebulae and reflection nebulae, categorizing the light created. Emission nebulae contain ionized gas (mostly ionized hydrogen) that produces spectral line emission [22]. These emission nebulae are often called HII regions; the term "HII" is used in professional astronomy to refer to ionized hydrogen. In contrast to emission nebulae, reflection nebulae do not produce significant amounts of visible light by themselves but instead reflect light from nearby stars [22].

The Horsehead Nebula, is an example of a dark nebula. Dark nebulae are similar to diffuse nebulae, but they are not seen by their emitted or reflected light. Instead, they are seen as dark clouds in front of more distant stars or in front of emission nebulae.

Planetary nebulae are those that form from the gaseous shells that are ejected from low-mass asymptotic giant branch stars when they transform into white dwarfs [22]. These nebulae are emission nebulae with spectral emission that is similar to the emission nebulae found in star formation regions [22]. Technically, they are a type of HII region because the majority of hydrogen will be ionized. However, planetary nebulae are denser and more compact than the emission nebulae in star formation regions. Planetary nebulae are so called because the first astronomers who observed these objects thought that the nebulae resembled the disks of planets, although they are not at all related to planets [23]. A protoplanetary nebula (PPN) is an astronomical object which is at the short-lived episode during a star's rapid stellar evolution between the late asymptotic giant branch (LAGB) phase and the subsequent planetary nebula (PN) phase [24]. A PPN emits strong in-infrared radiation, and is a kind of reflection nebula. The exact point when a PPN becomes a (PN) is defined by the temperature of the central star.

Supernova remnants are when a high-mass star reaches the end of its life and nuclear fusion ceases in the core of the star, collapsing inward upon itself. The contracting gas either rebounds or gets so strongly heated that it expands outwards from the core, thus causing the star to explode [22]. The expanding shell of gas forms a supernova remnant, a special type of diffuse nebula. Although much of the optical and X-ray emission from supernova remnants originates from ionized gas, a substantial amount of the radio emission forms non-thermal emission called synchrotron emission [22]. This emission originates from high-velocity electrons oscillating within magnetic fields.

## 1.4 Diffuse Interstellar Bands.

Diffuse interstellar bands(DIBs), as well as any other interstellar absorption features, may be formed in many clouds along any line of sight towards distant stars. They are, as a rule, observed in the featureless spectra of early type stars. These young objects are certainly very recently formed out of some dense interstellar clouds and may be still immersed in their remnants. The DIBs represent a large number of absorption lines between 4000 and 10000 Å. Since the discovery of the first two DIBs in the 1920s [25, 26], their identification remains one of the oldest mysteries in stellar spectroscopy. They were always considered as an interstellar feature, but it was not confirmed until the work of Merrill [27, 28]. He and his collaborators collected observational data which allowed them to derive several conclusions of basic importance for the future investigations of DIBs. It was demonstrated that these features did not participate in the velocity variations of spectroscopic binaries, and furthermore, their strength increased with distance and with the degree of the interstellar reddening of the star that furnished the background continuum. Many carriers of DIBs have been proposed over the years. They ranged from dust grains to free molecules of different kinds, and to more exotic specimens, like hydrogen negative ion. Unfortunately, a single carrier cannot be responsible for all known DIBs. However, it is very hard to estimate how many carriers can produce the observed DIBs.

The most convenient objects for study in a DIBs are spectra of the slightly reddened,

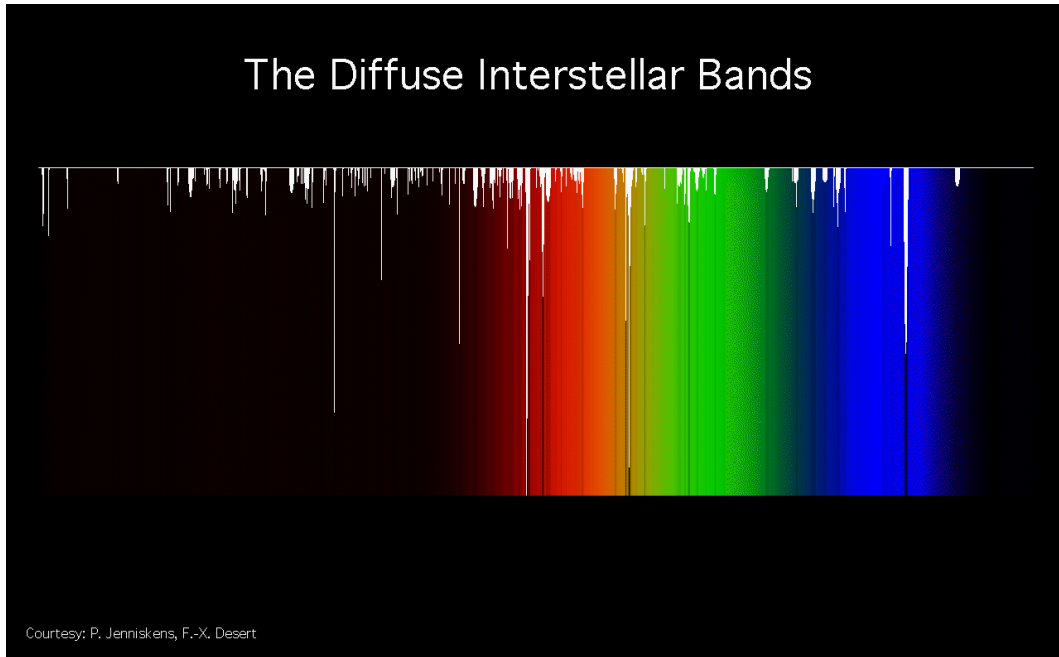


Figure 1.4: Diffuse interstellar bands are absorption features seen in the spectra of astronomical objects in our galaxy. From [<http://leonid.arc.nasa.gov/pjenniskens.html>].

bright stars. These stars are most likely to be obscured by single clouds and one can presume that the obscuring medium is homogeneous, i.e., characterized by a narrow range of physical parameters (temperature, column density, velocity, inner structure, shape and size of dust grains, chemical composition, etc). Bright, near-by stars obscured by one cloud would be the most appropriate candidates for the study of DIBs, however, the number of such stars is limited. It is essential to mention that accessible early type stars are usually either very distant or slightly reddened, thus the molecular features of spectra are either formed in several clouds along any line of sight or are too weak to be measured with proper precision. When several clouds are situated along a sightline, astronomers record "averaged spectra" and their interpretation is difficult. The next problem, which must be taken under consideration, is contamination of interstellar spectra with so called "telluric lines". Telluric features are atmospheric absorption lines inherent in the Earth's atmosphere. When an astronomer observes something from the Earth, such as a star, the starlight passes through the atmosphere and these telluric absorption features appear superimposed with the stellar spectrum. Telluric features in the IR region of the

spectrum are mainly the result of absorption by ozone ( $O_3$ ), gaseous oxygen ( $O_2$ ), and water vapor ( $H_2O$ ). Other lines include the sodium-D lines and Carbon dioxide ( $CO_2$ ). Of these lines,  $H_2O$  proves the most problematic, varying not only with air mass but with humidity levels within the atmosphere as well. Water vapor lines are also abundant within the IR region of the spectrum. When the spectrum of the object is taken in several different exposures, the telluric features will not be identical in each spectrum [29].

In the last 80 years since the first survey of DIBs was published [28], DIBs have been observed towards more than 100 hot stars. In the year of 1975 the major survey of DIBs was published by Herbig [30]. It contained 39 DIBs (twenty of them were observed for the first time) detected in the range of 4400 - 6700 Å. All these features were clearly seen in the spectrum of the heavily reddened star HD183143. The use of solid state detectors (CCDs) instead of photographic emulsion has resulted in the detection of many new DIBs. The initial set of a few features known in 1930s is now much bigger numbers, around three hundred [26, 31]. In his later work, [32] Herbig placed over 130 features and Krelowski [33] added to this wealth of data yet another 52 weak DIBs. As was said before, there exist about 300 DIBs, however, the existence of some of them is not sufficiently proved. On the other hand, many features still wait for their discovery.

#### 1.4.1 The structure of DIB.

Generally speaking, the clouds may differ in physical properties such as temperature or density as well as in chemical composition, dust content, molecular content etc. Local dense clouds may be rich in core-mantle grains and numerous molecules, which need protection against UV radiation. On the other hand, truly interstellar diffuse clouds may contain small grains and free atoms. In such a case their optical parameters may differ strongly; any of the observed absorption features could then be an ill-defined average over all clouds situated along a particular line of sight. The main parameters describing DIBs are:

$\lambda$  - the wavelength of the feature (approximately central wavelength of band in Å )

$A_c$  - the central depth of the band (described by percent of the continuum level),

FWHM - the full width (in  $\text{\AA}$ ) of the band at its half-maximum,

$W_\lambda$  - the equivalent width in  $\text{\AA}$  or  $\text{m\AA}$ , (describes width of a hypothetical line of the same area, of a rectangular profile, and normalized to unity).

The ratio of equivalent width reflects the ratio of the oscillator strength when DIBs are due to one carrier. The majority of DIBs possess relatively narrow profiles (their FWHM is usually of the order of few  $\text{\AA}$ ), wider bands also can be found in some spectra. As an example in the spectrum of HD183143 star [34, 30] the broad (FWHM  $30 \text{\AA}$ ) DIB around  $6177 \text{\AA}$  can be observed. Most of the DIBs are located at wavelengths longer than  $4430 \text{\AA}$ . The central depths of the majority of DIBs are of the order of 1-2% of continuum, but there are few exceptions, e.g. the central depth of 5780 DIB in some spectra [35] [36] reaches 30%. The parameters describing DIBs are not stable and vary from one line of sight to another: the survey of DIBs [37] showed that the value of the equivalent width may change drastically. For the strong 5780 DIB it varies from 0.11 (target star - HD30614) to 0.72 (target star HD183143). It should be noted that there are also differences in values of the parameters obtained by different authors. Comparison of equivalent widths of DIBs collected by Jenniskens and Desert [37] with the data of Herbig [32] shows a small systematic difference.

### 1.4.2 Doppler splitting.

Doppler splitting itself is one piece of evidence that DIBs are features of interstellar origin. Profile determinations of the diffuse interstellar bands could only be adequately addressed after new solid state detectors were widely available to record the astrophysical spectra. The first attempt was made by Snell and Van den Bout [38], who measured several high resolution and high S/N spectra covering a very narrow range, around the 5780 DIB, at the

McDonald Observatory. Their analysis was not, however, accompanied with that of other identified interstellar features; e.g. sodium or ionized calcium lines, which are known to be composed of many Dopplershifted single cloud profiles. The latter apparently originating in several clouds along the same line of sight. Doppler splittings could, in principle, also change the DIB profiles, but this broadening is not very likely to happen in the case of the analyzed 5780 feature, as this DIB is quite broad. Reasonable Doppler shifts, which are expected towards relatively nearby objects, cannot change a line profile substantially.

Thus, the broad profiles of the bands are only slightly altered, and only in the case of very sharp DIBs can the Doppler splitting be observed. In spite of the fact that astronomers do not really know a true assignment of the DIB carriers in the individual clouds, precise analysis of the interstellar lines is a very useful method of determine alteration in the DIB profiles.

The Doppler effect is not the one and only cause of broadening of DIBs [39]. The exceptionally broad DIB profiles around 5780 Å were found in the spectra of the stars belonging to the Orion Trapezium. The broadening of the bands in this case can not be explained by the Doppler effect. It is assumed that the matter surrounding these stars differs substantially in physical and chemical properties from that producing normal diffuse interstellar bands, and therefore it is this material that is directly responsible for the broadening profile observed there.

### 1.4.3 Reddening.

The colour excess, also called reddening, is defined as a difference in the value of extinction measured in two photometrical bands. It occurs due to light scattering off dust and other matter in the interstellar medium. The first careful correlation analysis of dependence of the DIB strength on reddening was carried out by Deeming and Walker [40]. The color excess  $E_{B-V}$  is related to the B-V (Blue-Visible in the UBV photometric system where color filters used include B-442 nm, V-540 nm ) color by:

$$E_{B-V} = (B - V)_{observed} - (B - V)_{intrinsic}$$

It is a popular and convenient quantity characterizing the interstellar matter.



### 1.4.4 Families of DIB.

Originally, it was quite natural to try to interpret the whole diffuse spectrum as being caused by the same carrier. High S/N spectra proved, however, that even the intensities of the strongest DIBs simply do not relate to each other in different spectra [41]. Thus several families of diffuse bands were proposed; members of any of them showing the same intensity ratios in every reddened spectrum. A family seems likely to be caused by one agent, different to those of other families. Of course an agent may be abundant in one cloud and scarce in another - thus the ratios of DIBs belonging to different families may vary strongly. The most extensive survey [42] of diffuse bands led to their division into three families, based on the DIB intensity ratios observed in several relatively nearby stars. The proposed families may be characterized as follows (Figure 1.5) :

- 1). The family of very broad and shallow bands, (the typical member: 4430), very

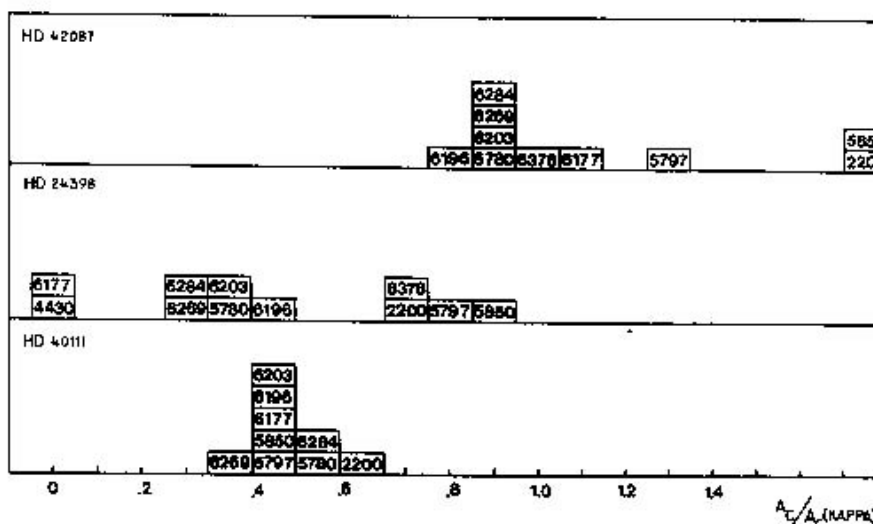


Figure 1.5: The histogram of Krelowski and Walker(1987) illustrating the division of DIBs into 3 families.

sensitive to varying physical parameters of single clouds, precise determinations of E.W.'s very difficult due to blending with numerous stellar lines and uncertain setting of continua;

- 2). The family of DIBs characterized by relatively symmetric profiles, some of them rather strong, sensitive to varying physical conditions in single clouds, the typical member:

5780, precise determinations of intensities relatively easy; possibly a couple of very shallow features also belong to this family ;

3). The family of relatively sharp, but usually also asymmetric features; seemingly less sensitive to the physical conditions inside the intervening clouds, but certainly absent in some of the clouds, the typical member: 5797, precise determinations of intensities not very easy due to wide shallow red wings.

## 1.5 Review of the proposed carriers.

Despite extensive laboratory studies, except for  $C_2$  [43] the carriers of the DIBs still have yet to be identified. Even the debate whether to assign the DIBs to gas-phase molecules or to solid particles has not yet been fully resolved. The carriers may be crucially important in interstellar chemistry: they may constitute a significant fraction of all chemically bonded matter in the interstellar gas, and many may be molecules larger than any so far identified. One theory suggest that long carbon chains or polycyclic aromatic hydrocarbons may be the carrier. Although additional theory and astronomical observations are needed, the identity of the carriers is now essentially a problem in laboratory astrophysics. Here is a brief review of the proposed carriers. Some of them are rather outdated, while others (e.g. carbon chains or PAHs) are still intensively studied and investigated as potential carriers. However, even in that case, no convincing proof has been found so far.

### 1.5.1 Solid particle-not favorite carrier anymore.

Dust particles were proposed as the first carrier of the DIBs. Theoretical calculations [44] predict the blue emission wing which should be observed in spectral features originating in solid particles. This postulated feature has never been observed in high S/N spectra which makes the hypothesis unlikely. The origin of DIBs in the dust grains would cause also substantial changes in the rest wavelengths and intrinsic widths of the feature due to the varying temperature of the solid particles. This should lead to changes of the observed

DIB pattern with those of the general shape of the extinction curve. Such a phenomenon is not observed anywhere in the galaxy [45]. If large particles are responsible for the DIBs, they should cause changes of polarization inside DIB profiles. Nevertheless no changes of polarization have been observed inside the DIB profiles despite several efforts. The relation between the DIB ratio and the far-UV extinction shown above can, however, allow one to consider once again the origin of DIBs in small size dust grains which would not cause any polarization.

### 1.5.2 Gas-phase molecules.

The detection of the first interstellar diatomic molecules (CN and CH) came a few years after the first observation of the DIBs. Stimulated by that discovery, a number of specific molecular carriers were proposed. Some of these proposals were based on near-agreement with gas-phase laboratory wavelengths, while others have come from a less direct reasoning. The list of specific molecules that have been suggested is very long, however, none of these have received enthusiastic support. Only few molecules have been detected in the ISM so far (Table 1.2). The reason to favour gas-phase molecular carriers is the possibility to explain the diffuseness of DIBs. It is very reasonable to suspect that the widths of the DIBs represent unresolved rotational structure. If so, then the excited rotational levels of the lower state must remain populated at the temperatures and densities found in diffuse clouds. Another argument for the molecular origin of DIBs comes from observations of the emission of the Red Rectangle nebula located around the carbon rich HD 44179 star. The background of the broad emission band from the Red Rectangle is superimposed by several quite narrow emission features situated in close vicinities of the known DIBs [46] [47]. The emissions seen in the Red Rectangle, do not resemble all observed DIBs but only some of them. It is in accordance with that fact that DIBs are not all of the same origin. The molecules responsible for the emission features in the Red Rectangle, must be able to fluoresce, which puts some constraint on the possible class of species to be considered as DIB carriers.

2 atoms	3 atoms	4 atoms	5 atoms	6 atoms	7 atoms
H <sub>2</sub>	C <sub>3</sub>	c-C <sub>3</sub> H	C <sub>5</sub>	C <sub>5</sub> H	C <sub>6</sub> H
AlF	C <sub>2</sub> H	l-C <sub>3</sub> H	C <sub>4</sub> H	l-H <sub>2</sub> C <sub>4</sub>	CH <sub>2</sub> CHCN
AlCl	C <sub>2</sub> O	C <sub>3</sub> N	C <sub>4</sub> Si	C <sub>2</sub> H <sub>4</sub>	CH <sub>3</sub> C <sub>2</sub> H
C <sub>2</sub>	C <sub>2</sub> S	C <sub>3</sub> O	l-C <sub>3</sub> H <sub>2</sub>	CH <sub>3</sub> CN	HC <sub>5</sub> N
CH	CH <sub>2</sub>	C <sub>3</sub> S	c-C <sub>3</sub> H <sub>2</sub>	CH <sub>3</sub> NC	CH <sub>3</sub> CHO
CH <sup>+</sup>	HCN	CH <sub>3</sub>	C <sub>4</sub> H <sup>-</sup>	c-H <sub>2</sub> C <sub>3</sub> O	C <sub>6</sub> H <sup>-</sup>
O <sub>2</sub>	HCP	C <sub>2</sub> H <sub>2</sub>	H <sub>2</sub> CCN	CH <sub>3</sub> OH	CH <sub>3</sub> NH <sub>2</sub>
CN	HCO	NH <sub>3</sub>	CH <sub>4</sub>	CH <sub>3</sub> SH	c-C <sub>2</sub> H <sub>4</sub> O
CO	HCO <sup>+</sup>	HCCN	HC <sub>3</sub> N	HC <sub>3</sub> NH <sup>+</sup>	H <sub>2</sub> CCHOH
CO <sup>+</sup>	HCS <sup>+</sup>	HCNH <sup>+</sup>	HC <sub>2</sub> NC	HC <sub>2</sub> CHO	
CP	HOC <sup>+</sup>	HNCO	HCOOH	NH <sub>2</sub> CHO	
SiC	H <sub>2</sub> O	c-SiC <sub>3</sub>	H <sub>2</sub> COH <sup>+</sup>	H <sub>2</sub> CCNH	
SiH	c-SiC <sub>2</sub>	HNCS	H <sub>2</sub> CNH	C <sub>5</sub> N	
HCl	H <sub>2</sub> S	HOCO <sup>+</sup>	H <sub>2</sub> C <sub>2</sub> O	l-HC <sub>4</sub> H	
KCl	HNC	H <sub>2</sub> CO	H <sub>2</sub> NCN	l-HC <sub>4</sub> N	
NH	HNO	H <sub>2</sub> CN	HNC <sub>3</sub>		
NO	MgCN	H <sub>2</sub> CS	SiH <sub>4</sub>		
NS	MgNC	H <sub>3</sub> O <sup>+</sup>			
NaCl	N <sub>2</sub> H <sup>+</sup>				
OH	N <sub>2</sub> O				
PN	NaCN				
SO	OCS				
SO <sup>+</sup>	SO <sub>2</sub>				
SiO	CO <sub>2</sub>				
SiS	NH <sub>2</sub>				
CS	H <sub>3</sub> <sup>+</sup>				
HF	H <sub>2</sub> D <sup>+</sup> , HD <sub>2</sub> <sup>+</sup>				
SH	SiCN				
HD	AlNC				
FeO	SiNC				
CF <sup>+</sup>					
SiN					
PO					

8 atoms	9 atoms	10 atoms	11 atoms	12 atoms	13 atoms
CH <sub>3</sub> C <sub>3</sub> N	CH <sub>3</sub> C <sub>4</sub> H	CH <sub>3</sub> C <sub>5</sub> N	HC <sub>9</sub> N	C <sub>6</sub> H <sub>6</sub>	HC <sub>11</sub> N
CH <sub>3</sub> COOH	C <sub>3</sub> H <sub>6</sub>	(CH <sub>3</sub> ) <sub>2</sub> CO	CH <sub>3</sub> C <sub>6</sub> H	C <sub>2</sub> H <sub>5</sub> OCH <sub>3</sub>	
HC(O)OCH <sub>3</sub>	CH <sub>3</sub> CH <sub>2</sub> CN	(CH <sub>2</sub> OH) <sub>2</sub>			
C <sub>7</sub> H	C <sub>8</sub> H	CH <sub>3</sub> CH <sub>2</sub> CHO			
H <sub>2</sub> C <sub>6</sub>	(CH <sub>3</sub> ) <sub>2</sub> O				
CH <sub>2</sub> OHCHO	C <sub>8</sub> H				
l-HC <sub>6</sub> H	CH <sub>3</sub> CH <sub>2</sub> OH				
CH <sub>2</sub> CHCHO	HC <sub>7</sub> N				
CH <sub>2</sub> CCHCN	CH <sub>3</sub> C(O)NH <sub>2</sub>				

Table 1.2: There are 134 molecules listed as detected in the interstellar medium or circumstellar shells.

### 1.5.3 Linear carbon chains.

Many of the molecules observed using radioastronomical methods are linear species built on a carbon skeleton. This fact makes possible the presence of bare carbon chains in the interstellar space. Such nonpolar molecules cannot be observed with the aid of radioastronomical techniques and optical spectra remain unknown. Douglas [1] proposed such carbon chains to be the carriers of DIBs. Fulara [48] and Freivogel [49] extended this hypothesis to the whole class of linear, unsaturated hydrocarbons. The species trapped in neon matrices, according to a given mass selected of  $C_nH_m^-$ , showed strong absorption bands in the red and near infrared regions of the spectrum. Many of these bands fall very close to DIB wavelengths. The recent comparison of the laboratory spectra of several linear molecules obtained in the gas phase with the aid of the cavity ring-down method with the observed spectra of reddened stars (Motylewski et al. [50]) did not give any positive conclusion. None of the experimentally determined features matched any of the observed ones. The closest match is that of NCCCCN<sup>+</sup>, but also in this case the wavelengths differ by 0.9 Å. However, the similarity of both profiles suggests that molecules similar to NCCCCN<sup>+</sup> may be responsible for some DIBs.

#### 1.5.4 Polycyclic Aromatic Hydrocarbons - PAHs.

The occurrence of the infrared emission bands in many sites in the Galaxy has often been attributed to the presence of PAHs in the ISM, inspiring the idea that their cations might be carriers of DIBs [51]. Polycyclic aromatic hydrocarbons (PAHs) are hydrocarbon compounds with multiple six-membered aromatic rings. Such species are thought to be a common component of the interstellar medium in the Milky Way and in external galaxies. PAHs are typically observed in infrared emission following excitation by either ultraviolet or visible radiation in assorted regions of the interstellar medium exposed to radiation. Despite all attempts, no specific types of PAHs responsible for these features have been identified, and the form and intensity of the spectra vary strongly from one region to another, probably reflecting a variety of sizes and abundances [52]. The origin of PAHs also remains an unanswered question. Most believe that PAHs are formed in the atmospheres of carbon stars or in supernovae. Various observations show that the abundance of small free-flying PAHs has a tendency to decrease in dense clouds where UV photons do not penetrate [53]. It was proposed [54] that PAHs form larger PAHs or PAH clusters in such dense regions. As a consequence, free-flying PAHs observed at the border of illuminated clouds may be the result of photo-dissociation of these larger species. Although they determined a minimal size of 400 carbons for these species using mid-infrared ISOCAM maps of photo-dissociation regions (PDRs), this number is very uncertain. If free-flying PAHs are not present in the dense interstellar medium, an efficient process is needed to aggregate them. Aggregation is poorly understood, and the time in which this process occurs is undetermined, as is the fraction of small PAHs remaining in dense clouds unexposed to intense radiation. Currently, constraints on the PAH size and abundance as a function of the physical conditions in the dense interstellar medium remain weak. The electronic absorption spectra of many PAH cations have been observed in noble gas matrices [55].

### 1.5.5 Fullerenes.

Emission from aromatic hydrocarbons dominate the mid-infrared emission of many galaxies, including our own Milky Way [56]. Only recently have aromatic hydrocarbons been observed in absorption in the interstellar medium, along lines of sight with high column densities of interstellar gas and dust. The hypothesis that fullerenes are responsible for the occurrence of DIBs was proposed by Kroto (1985) soon after the discovery of  $C_{60}$ , when this molecule was recognised to be exceptionally stable. This hypothesis was refuted when the strongest absorption of  $C_{60}$  appeared to fall within the UV region (Hauffer et al. 1991, Kratschmer 1993). In the visible region, the absorption spectrum of  $C_{60}$ , isolated in an argon matrix, shows a few very weak peaks that correspond to electronic transitions which are forbidden due to symmetry reasons [57]. The visible portion of the spectrum of the next molecule in the fullerene series -  $C_{70}$  - contains several weak peaks. Although the spectrum of  $C_{70}$ , isolated in a neon matrix, falls within the region where the DIB density is substantial, the low intensities of its absorption peaks exclude the possibility of assigning any DIB to fullerenes [58]. If fullerenes existed in the ISM, they should mostly occur in the ionized form. The fullerene cations were thus suggested to be the next candidates for DIB carriers [59]. The absorption spectra of the  $C_{60}$  cation and the anion have so far only been measured in noble gas matrices [58]. The spectral features of  $C_{60}^+$  are situated close to two interstellar spectral features discovered quite recently [60]. The features are likely to be identified as those of  $C_{60}^+$ , but they appear in the range heavily contaminated with telluric lines which makes the measurements very difficult. It is possible that the gas phase electronic spectra of  $C_{60}^+$  will be experimentally obtained in the near future.

## 1.6 Conclusion.

The long history of the theories that attempt to identify the DIBs still remains far from being concluded. Partially it is because of the lack of laboratory spectra of many molecules, which can be considered as possible carriers. However, of the all proposed carriers two of them seem to outrun the rest in feasibility. Namely, carbon chains and polycyclic

aromatic hydrocarbons.

It is now clear that the DIBs cannot be explained by the early concept of a single carrier owing to the large number of bands detected and the lack of correlation between them. The present consensus, based on high-resolution astronomical observations, is that the carriers are large carbon-bearing gas phase molecules in either the neutral or/and ionized forms and that these molecular carriers are part of an extended size distribution of the interstellar dust. At the moment it is difficult to say which group of the molecules could be really responsible for DIBs (PAHs or carbon chains). Metal containing carbon compounds are also becoming increasingly interesting in astrochemistry, were a few such molecules (Table 1.2) were detected in carbon rich stars through their microwave and sub-mm/mm transitions [61, 62].

Because many metal elements such as magnesium, iron and sodium are heavily depleted in molecular clouds, the main question become in what form do these metal containing species exist in the interstellar medium. It is generally believed that the most refractory metal elements are condensed out into the surface of dust grains. Unfortunately, knowledge about gas-phase abundances and the surface absorption of such species in the ISM is limited. Therefore, the spectroscopic investigation of metal containing molecules in the ISM has implication for both gas-phase and grain chemistry [62].

To date, eleven main group dicarbides have been spectroscopically investigated ( $\text{XC}_2$ ,  $\text{X} = \text{H, B, C, N, O, Al, Si, P, S, Cl, As.}$ ) [63]  $\text{HC}_2$ ,  $\text{NC}_2$  [64],  $\text{OC}_2$  [65],  $\text{PC}_2$  [63],  $\text{SC}_2$  [66],  $\text{AsC}_2$  [63] all posses ( $\text{C}_{\infty v}$ ) structures.  $\text{ClC}_2$  has been shown to have a bent ground state  $\tilde{X}^2A'$  [67], while  $\text{AlC}_2$  and  $\text{SiC}_2$  are T-shaped ( $\text{C}_{2v}$ ) [68, 69].

The structure of various organometallic species depend on the nature of the chemical bonding between the carbon and metal atoms. The small metal-carbon clusters provide an opportunity to understand this chemical interaction and gain insight into the growth mechanism of metal-carbon nanomaterials. These metal carbides and dicarbides represent an important chemical class with application in a wide range of processes and materials. However, this spectroscopic information can reveal aspects of metal-carbon bonding which is scarcely available at the triatomic level.



# Chapter 2

## Experimental Setup

### 2.1 Introduction

Laser induced fluorescence (LIF) is a highly sensitive method of interrogating gas phase molecules. It has been applied with great advantage in various environments, from ultra low pressure regimes of molecular beams and beam surface scattering to relatively high pressure plasmas and flames. The concept of LIF is simple, but the implementation of the concept is quite involved. What follows is a brief description of the apparatus, an overview of the experimental setup, and an in-depth description of the many individual components that comprise the experimental process in roughly the order in which they appear during one experimental cycle.

### 2.2 Laser Induced Fluorescence Concept

Laser-induced fluorescence (LIF) is the optical emission from molecules that have been excited to higher energy levels by absorption of electromagnetic radiation. (LIF) is used for studying structure of molecules, detection of selective species in foreign environments and flow visualization. The species to be examined is excited with help of a laser. The excited species will after some time, usually in the order of few nanoseconds to microseconds, de-excite and emit light at a wavelength similar or larger than the excitation wavelength. This light, called fluorescence, is then detected using photodiodes, CCD cameras, or highly

sensitive photomultiplier tubes.

Two different kinds of spectra exist, disperse spectra and excitation spectra. Electronic excitation spectra are obtained by irradiating the molecules with a tunable laser and observing the total fluorescence intensity. As the laser is tuned across the absorption band system a fluorescence excitation spectrum results which strongly resembles the absorption spectrum.

Dispersed, fluorescence spectra are usually obtained by fixing the laser wavelength so that it corresponds to a particular vibronic transition, thus populating a single vibronic level in excited electronic state. In a free-jet expanded molecular beam the conditions can be assumed as collision-free. In this situation the fluorescence will be from the single vibronic level which was populated by the absorption of the fixed laser radiation (Figure 2.1). As it shown on the Figure 2.1, information about the ground state can be obtained from disperse fluorescence.

For the fluorescence between two levels one can write:

$$I_{LIF} = G\Theta_{21}B_{12}(\nu)N_1(J)I_\nu$$

Where  $G$  = light collection efficiency,  $\Theta_{21}$ =fluorescence quantum yield,  $B_{21}$ =absorption coefficient,  $N_1(J)$ = ground state population, and  $I_\nu$ =laser intensity.

$$\Theta_{21} = \frac{A_{21}}{A_{21}+Q_{21}+(\textit{other minor terms})}$$

$Q_{21}$ = loss via collisions (quenching).

The main advantage of fluorescence detection compared to absorption measurements is the greater sensitivity achieved because of lower background signal. LIF is useful to study the electronic structure of molecules and to make quantitative measurements of analyte concentrations. Analytical applications include monitoring gas-phase concentrations in the atmosphere, flames, and plasmas, and remote sensing using light detection and ranging (LIDAR).

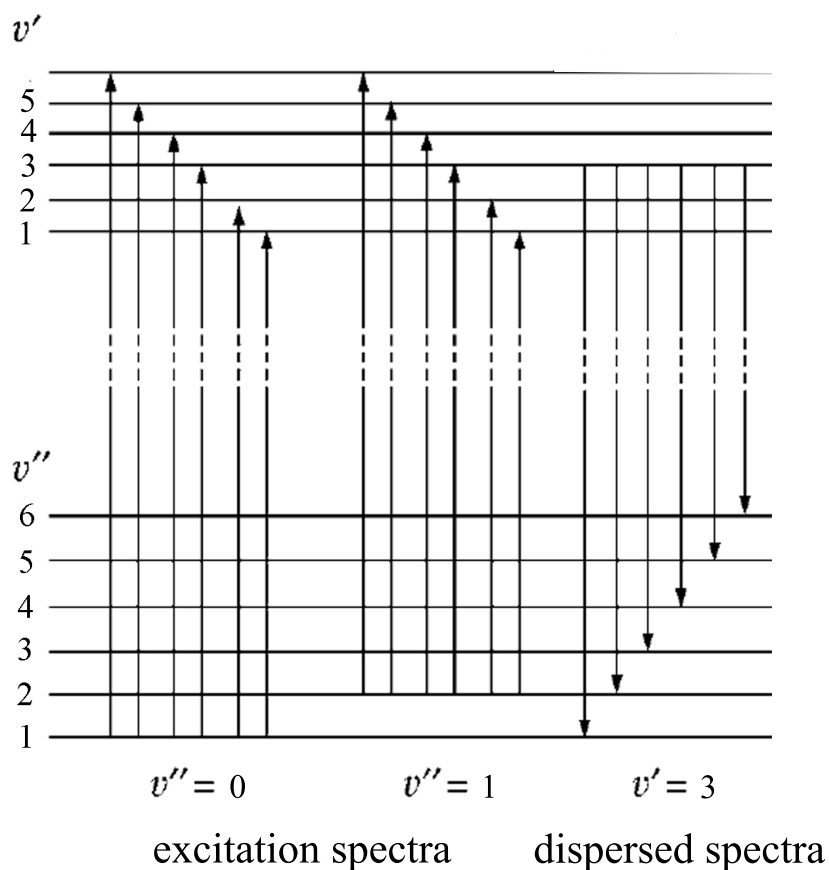


Figure 2.1: The comparison of dispersed and excitation spectra.

One of disadvantage of LIF is the possible quenching of fluorescence at higher pressures due to the numerous collisions of molecules. This, however, can be avoided through the use of molecular beam. A second problem encountered is that the molecules should fluoresce, which is usually limiting by the size of molecule.

### 2.3 Overview of the experiment

The LIF setup (Figures 2.2 and 2.3) is composed of two chambers. Both chambers are constructed of stainless steel with aluminum and stainless steel flanges. There are two reasons for the second chamber. First is to move the window for the ablation laser as far as possible from the source and the second is to add a second diffusion pump for

extra pumping efficiency. The whole experiment takes place in the first chamber. The chambers are not separated by any valves. The chambers are evacuated to approximately  $10^{-7}$  torr by two diffusion pumps connected through butterfly valves. The main chamber is evacuated by a Inficon model PDI250-W diffusion pump capable of pumping  $1750 \text{ l s}^{-1}$  of air at  $10^{-4}$  mbar. The second diffusion pump attached to the chamber is an Edwards model Diffstak CR160/700M B34837978 with a pumping speed of  $750 \text{ l s}^{-1}$  of air at  $10^{-4}$  mbar. The diffusion pumps are backed by an Edwards model E2M80 direct drive vane vacuum pump, capable of evacuating roughly  $1600 \text{ l min}^{-1}$ . When the pulsed valve is running (General valve, series T, 0.3 mm diameter), the pressure in the chamber is typically kept near  $1.5 \cdot 10^{-4}$  mbar.

The experiment operates at 20 Hz. All timings are coordinated through three Stanford Research System delay generators connected in sequence.

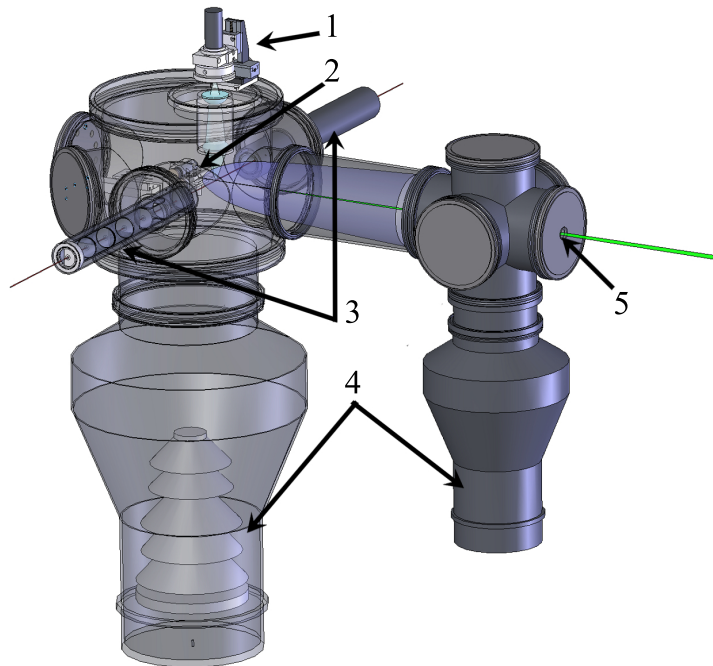


Figure 2.2: LIF experimental setup: (1)- optical system; (2)-ablation(discharge)source; (3)-baffle system; (4)-diffusion pumps; (5)-ablation laser input window.

Each experimental cycle, using the ablation source, begins with the firing of the pulsed valve and the release of a gas pulse into the vaporization block channel. The gas pulse flows

through the channel and passes over the metal sample rod. The ablation laser is timed to strike the sample rod as the gas pulse passes over it. Metal atoms and ions are ejected from the sample rod into the channel and form a plasma. The metal atoms collide with each other and with atoms from the carrier gas pulse. The collisions allow molecules and clusters to form and cool. Molecular formation continues as the gas pulse travels through the channel in the vaporization block. At the exit orifice of the block the molecular packet undergoes a supersonic expansion into vacuum. The molecules continue to collide with the carrier gas atoms and are cooled rotationally and vibrationally to approximately 30 K. The molecular beam expands conically into the chamber reaching its maximum velocity and minimum internal energy. Approximately 60 mm down stream from the exit orifice the molecular beam is intersected by the scanning probe laser. The fluorescence signal is collected by an  $f/1$  lens and detected using a Hamamatsu photomultiplier tube (PMT) R374 or R5929. The signal from (PMT) is collected and averaged with a LeCroy LC 334A oscilloscope which is remotely operated by a PC using home made Lab View software. The same software operates the lasers.

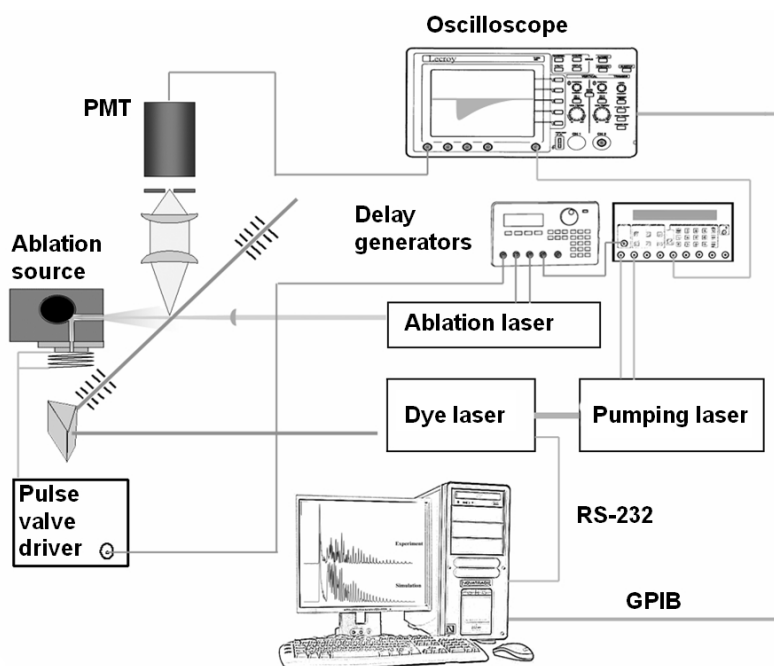


Figure 2.3: LIF experimental setup diagram.

and LeCroy LC334A 500 MHz digital oscilloscope.

## 2.4 Molecular sources

The molecules studied in this thesis can not be purchased in bulk form from a chemical supply house. They usually have nonzero dissociation energies that allows them to remain bound when undisturbed, but when constantly assaulted by collisions with atmospheric gases or with other identical molecules, they tend to form more thermodynamically stable species. As a consequence, such molecules could not be prepared, stored, and then studied at the leisure of the experiment. Instead they have to be synthesized, immediately isolated in the vacuum chamber, and then spectroscopically probed. In our experimental setup we use two different means of production: discharge and laser ablation sources.

### 2.4.1 Discharge source

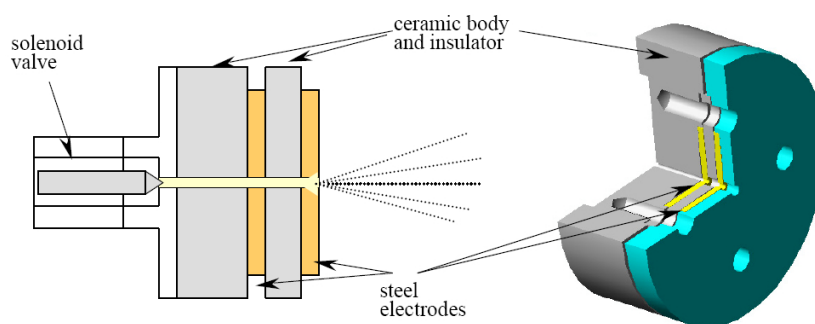


Figure 2.4: Discharge source

The discharge source is depicted in Figure 2.4. Based on the design of Ohshima and Endo [70], it is indispensable for producing a great variety of both neutral and ionic hydrocarbon radicals. Nearly all carbon-chain-related spectroscopic gas phase studies in the J.P. Maier group in Basel have been done using this pinhole or slit[26] discharge source. A precursor is typically diluted with buffer gas (Ar, Ne, He, N<sub>2</sub>, etc.) down to 0.15-3% and expanded under 5-10 bar backing pressure into vacuum through the ceramic body. The gas burst is generated by a solenoid valve controlled by a Berkley Nucleonics delay generator. The amount of gas released is varied by manipulating the width of the valve opening pulse. Adjusting this in accord with the pressure in the source chamber

allows one to keep the latter constant and thus ensure stable source conditions. A 100-200  $\mu\text{s}$  long high voltage pulse (-700 to 900 V) from a home-built power supply is applied between the stainless steel electrodes, placed on either side of a 10-20 mm thick ceramic insulating spacer. The channel is 1-1.2 mm thick all the way through the source, except for the insulator section where it is enlarged to 2 mm in order to create a localized plasma region. The inner electrode is simply a 1 mm thick disk with a 1 mm hole, and the outer one is 3.4 mm and possessing a divergent conical exit channel through which plasma is expanded to the vacuum chamber. The mass distribution of the clusters can be influenced by increasing the thickness of the outer electrode. A lengthened electrode allows more time for clustering and generally results in a higher relative abundance of larger species. Source stability is better when the outer electrode is grounded while the inner one is negatively pulsed. The source is mounted on an XYZ translation system, allowing for the distance and position of the source relative to the probe beam to vary, and thus a means to adjust the tolerance to the perpendicular velocity of the species in the beam. This gives control over the concentrations of species (both cold and hot) and their temperature characteristics during the experiment. The typical distance was 30-50 mm. In the present work, the discharge source was used mostly for adjusting and testing the experimental setup.

## 2.4.2 Laser ablation source

Laser ablation is a widespread field, with many multidisciplinary applications such as the production of gas phase ions. The process of ablation itself is quite complicated and still not fully understood. Many complexities are involved in understanding laser ablation, including the dynamics of the laser-produced plume, the ablation mechanism itself, and the problems of a decaying, and often non-uniform, target. Despite this the laser ablation process provides a relatively straightforward method to produce metal ions in the gas phase.

A simple calculation will demonstrate why pulsed laser ablation is useful. If the output of a pulsed laser of short duration (10 ns) with approximately 5 mJ/pulse is focused to a spot of about 0.5 mm, the total irradiance ( $\text{W}/\text{cm}^2$ ) at the focus is  $2.5 \cdot 10^8 \text{ W}/\text{cm}^2$ . This

represents quite a high concentration of energy in time and space. When such a laser pulse is allowed to strike a metal sample, this energy is deposited into such a small area in such a short period of time that the metal cannot dissipate the energy quickly enough into the bulk via vibration to allow the structure of the sample to be maintained. In other words, the metal sample does not just suffer a temperature increase. Instead, the material at the focus of laser beam is rapidly heated to melting and then heated even further to the point of vaporization and beyond. What leaves the surface is a hot vapor of metal atoms as well as thermally produced atomic metal ions and electrons. This collection of material is most properly thought of as a plasma. Further heating of the vaporized material occurs as some of the incident laser energy is absorbed by the newly formed plasma. This causes a greater degree of ionization and absorption, leading to further heating of the plasma until the laser pulse ends. The final temperature of plasma can be estimated to be  $10^4$  to  $10^5$  K.

This description of plasma production is greatly simplified. The exact nature of the plasma depends upon the exact irradiance of the sample surface by the laser as well as various properties of the material being vaporized such as heat capacity, thermal conductivity, heat of fusion, heat of vaporization, and surface reflectivity at the wavelength of laser being used to vaporize the metal.

How plume formation depends on these parameters is clearly seen in (Figure 2.5) where three different materials are ablated. The details of plasma formation have been studied extensively by others, and it continues to be an active area of research. Here, however, the concern is not with fully understanding the details of how the plasma is produced, but rather laser vaporization of the target is merely treated as a simple and reliable way to deposit a large quantity of metal atoms into the gas phase in a short period of time during each experimental cycle for use in the synthesis of the molecular species of interest. To optimize species production, permutation of many variables such as vaporization laser power, laser wavelength, and sample composition are varied until the desired result is achieved.

Several authors attempted to provide a simple mathematical relationship between the mass ablated and laser irradiance, which included the linear and the quadratic irra-



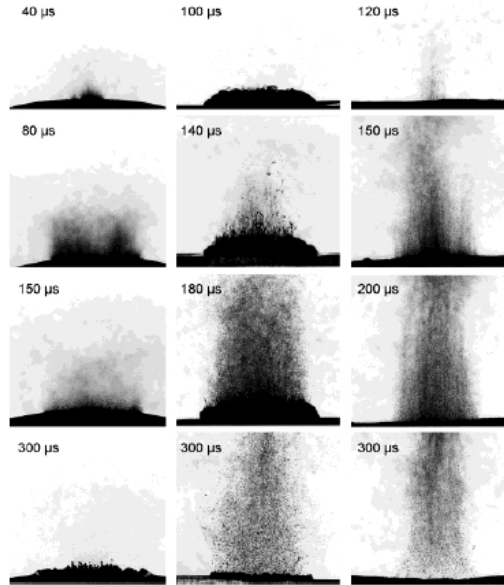


Figure 2.5: Dynamics of Er:YAG laser ablation of water, gelatin with 70% water content, and skin using a radiant exposure of  $4.6 \text{ J/cm}^2$ , 5 mm spot size, and  $200 \mu\text{s}$  pulse duration [71]. The times after the beginning of the laser pulse when the photographs were taken are indicated on the individual frames. Note the increasing delay in the ejection of particulate matter with increasing mechanical strength of the target.

diance terms. However the available publications show that the existing models can not precisely describe the process of ablation. Most of them are valid only for single pulse experiments and they are not applicable to explain the results of multiple events. Experimental measurements consistently show that for low laser fluence, for which the laser energy absorbed by the plume is thought to be negligible, the expansion front is a factor of 2-3 faster than predicted from an unsteady adiabatic expansion with typical vaporization temperatures [72]. The maximum expansion velocity from the free expansion model gives a velocity of  $5.55 \cdot 10^5 \text{ cm s}^{-1}$ .

The most important characteristic of ablation in this work is the number of molecules produced by the ablation source in one pulse. A simple estimation of how many molecules can be melted, evaporated, and heated up to the average plasma temperature with the energy of one laser pulse yields  $\sim 10^{16}$  molecules. This is the upper limit for the number of molecules, due to the fact that surface reflectivity and the dissipation of energy to the bulk of the sample is not taken into account. Therefore, a semiempirical approach in

which this mass was derived from experiment was used. The average mass of a sample vaporized by one laser pulse (25 mJ per pulse, 9 ns, 532 nm second harmonic (SH) of Nd:YAG.) was calculated by weighing the sample before and after approximately  $10^6$  laser shots and dividing the weight difference by the number of shots. In this rude estimate the average mass removed per laser shot is on the order of 80 ng for all the typical materials used in our experiment (Al, Mg). This results in the formation approximately of  $\sim 10^{14}$  molecules/pulse, and is already two orders of magnitude less than the simple estimation of applied energy given above. The same approach to the measurement of the mass ablated has also been used [73].

Newertheless this approach also does not give us correct information about the number of molecules in the beam due to the drops of melted metal (similar to the drops in Figure 2.6, in the so-called "Recoil-Induced Material Expulsion" [71]).

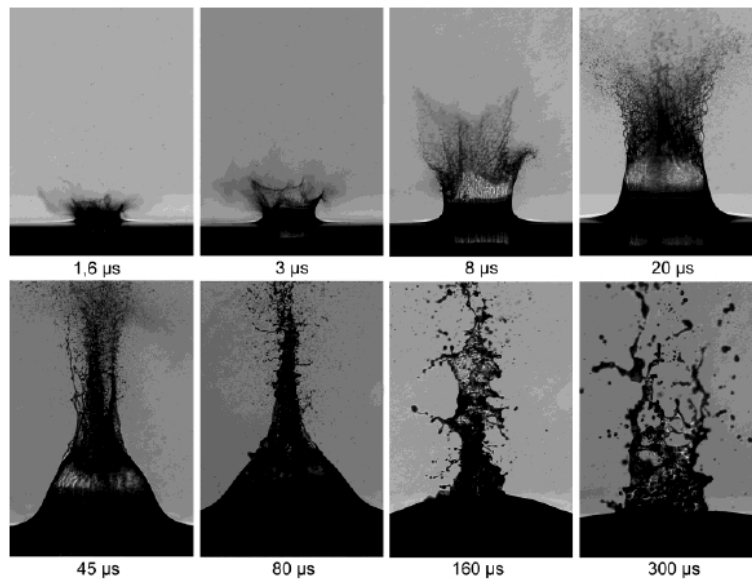


Figure 2.6: Late phase of the ablation dynamics for water ablation [71]. During the first  $20 \mu s$ , the plume dynamics is characterized by a powerful recoil-induced expulsion of liquid water. The flow in the vapor plume then leads to a focusing of the hollow water column into a jet like structure ( $20-80 \mu s$ ) that finally disintegrates ( $80-300 \mu s$ ).

The recoil stress produced by both vaporization and material ejection through phase explosion and confined boiling can induce a secondary material expulsion process that provides a strong increase in the ablation efficiency. Recoil-induced material expulsion is

most pronounced during ablation of liquids and of materials for which a molten layer is formed during the ablation process. Variations of the recoil stress amplitude in the radial direction result in a force driving the liquid toward the edges of the ablation crater and out of the crater, as illustrated schematically (Figure 2.7). However, that formation of a molten layer of tissue is not a necessary condition for recoil-induced material expulsion. Material will be ejected whenever the recoil stress component in the radial direction exceeds the mechanical strength of the tissue. While the primary material ejection visible at short delay times takes place across the entire ablation area, recoil-induced expulsion occurs preferentially at the ablation crater and includes the ejection of droplets much larger than those ejected during the initial phase explosion.

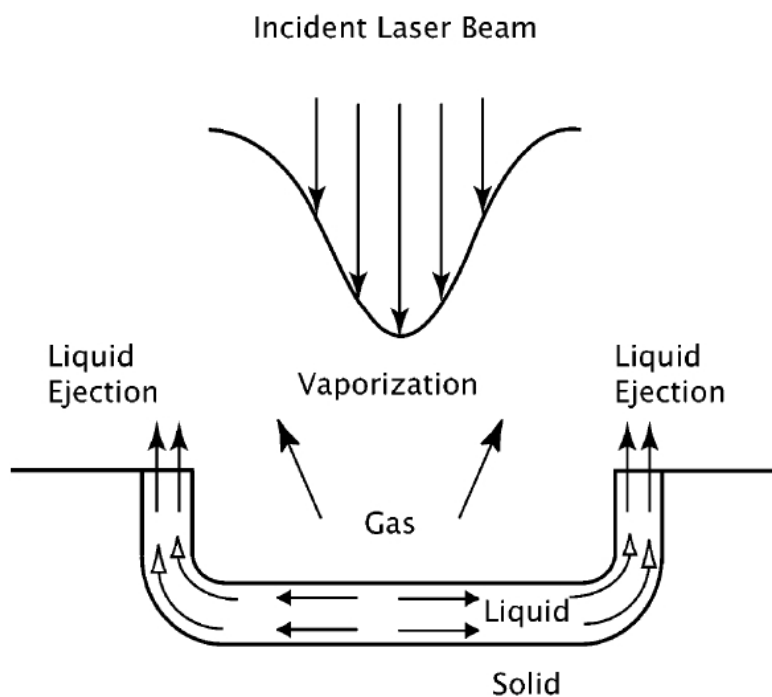


Figure 2.7: Illustration of recoil-induced material expulsion.

A significant amount of mass is carried away and usually deposited in the source channel, and therefore requires stopping the experiment periodically for cleaning.

Another important question is how molecules or cluster formation occurs, what parameters to vary and how to exert influence on this process. Probably the main parameter is the temperature of plume, which is predicted to be  $10^4 - 10^5$  K just after ablation and

rapidly decreases in time. When the temperature is too high nothing really forms because bonds are too weak in comparing with the internal energy to hold atoms together, and when the temperature decreases close to room temperature it is already not enough energy to start the reaction. Thus, a temperature or time "window" for our reactions needs to be determined. An experimental study of carbon nanotube growth [74] shows that even after 1 ms the average temperature for graphite plume can stay at about 1500 C (Figure 2.8) if the propagating plume is surrounded by gently flowing inert gas.

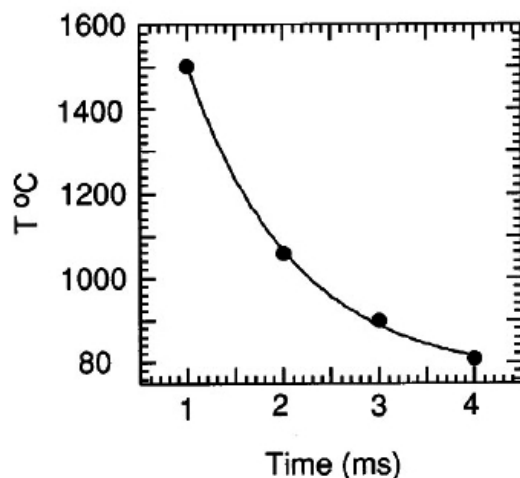


Figure 2.8: Temperature of carbon particles inside the propagating plume vs time after ablation [74].

It is obvious that in the case of laminar flow, an axisymmetric temperature distribution in the plume will form, with the temperature in the core of the plume much higher compared to the border.

To efficiently produce a certain species it is important to know how the molecule or cluster size changes in time. The typical time of cluster formation was studied in detail [74] (Figure 2.9). The evaporated material stays in the vapor phase until approximately 100 ms after ablation. During this time, the laser plasma is very hot and emission from excited atoms and molecules dominate laser-induced emission. The laser plasma cools rapidly, increasing the populations of the atomic and molecular ground states as indicated by laser induced fluorescence measurements. To observe the plume of ejected material at  $t > 200 \mu\text{s}$  they used laser-induced incandescence and Rayleigh scattering from clusters and

nanoparticles. By that time the plume becomes substantially nonuniform, demonstrating pronounced turbulent structure within the plumes. At later times ( $>2$  ms) the plume acquires a characteristic vortex ring shape that still has a highly turbulent substructure. Images of the plume and LIF spectra show that carbon condenses and forms clusters by  $t=200$  ms after ablation, while the metal catalyst atoms condense much later.

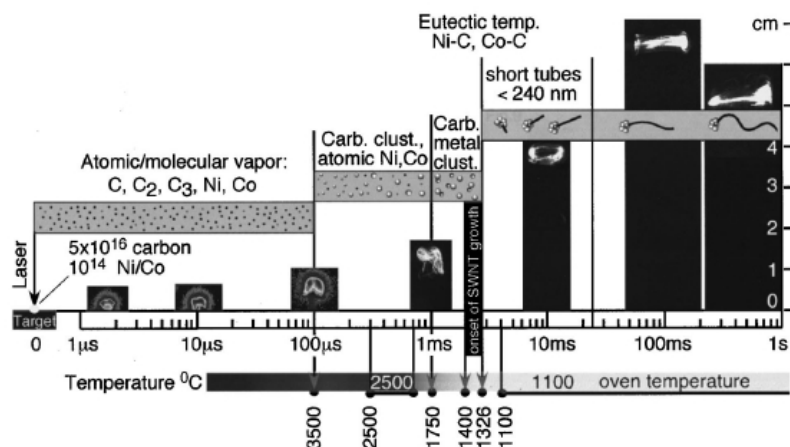


Figure 2.9: Summary of the results from the in situ imaging and spectroscopic diagnostic investigations of SWNTs growth inside a hot oven [74].

In order to do high-resolution spectroscopy the molecules in our beam should be quite cold. To do this the ablation plume is co-expanded with a carrier gas. The presence of carrier gas not only cools the molecules but also significantly decreases the velocity of the plume from  $4\text{--}8\text{ km s}^{-1}$  [75] to approximately  $500\text{--}600\text{ ms}^{-1}$ , which corresponds more to the velocity of gas molecules at room temperature.

In the present work, the interest is not in pure metal molecules, but more with metal terminated hydrocarbon chains. To produce such species, methane or acetylene are mixed into the carrier gas (typically 1% in argon). In the case of using pulsed carrier gas, the situation becomes even more complicated. Gas flow turbulently interacts with the ablation plume, significantly reducing its temperature and destroying the velocity profile and thermal distribution. This makes theoretical prediction of this process even less possible.

### 2.4.3 Free jet expansion

In all types of ablation sources used in this work, the ablated plume mixed with pulsed carrier gas inside a source channel, reacted with ablation plasma to form the required molecules and then expand into the vacuum. Expansion to the vacuum (free jet expansion) is a complex physical phenomena which is important in many technological applications including direct vapour deposition in materials and semiconductor processing, laser machining, rocket propulsion, and combustion.

It is assumed that supersonic neutral gas flows can be reasonably approximated as a near-thermal-equilibrium continuum [76]. In addition, the flows are assumed to be laminar (justifications for this assumption are provided in the discussion of the numerical results) and the thermal state of the neutral particles is determined by assuming that the gas is both a calorically and thermally perfect gas and obeys the ideal gas equation of state  $p = \rho RT$ , where  $p$  is the static pressure,  $\rho$  the gas density,  $T$  the temperature, and  $R$  the gas constant. Accordingly, the conservation form of the partial differential equations governing the transport of the neutral gas are the well-known Navier-Stokes equations for a compressible fluid, which, using vector notation, can be expressed as

$$\frac{\partial \rho}{\partial t} + \nabla \cdot (\rho v) = 0,$$

$$\frac{\partial}{\partial t}(\rho v) + \nabla \cdot (\rho v v + pI - \tau) = \rho f,$$

$$\frac{\partial}{\partial t}(\rho E) + \nabla \cdot [\rho v (E + \frac{p}{\rho}) + q - \tau \cdot v] = \rho f \cdot v,$$

where  $v$  is the velocity vector,  $E = p/(\rho(\gamma - 1)) + |v|^2/2$ , is the specific total energy,  $\tau$  is a second-order tensor or dyadic quantity representing the viscous stresses with elements  $\tau_{ij} = \mu(\frac{\partial v_i}{\partial x_j} + \frac{\partial v_j}{\partial x_i} + \delta_{ij} \frac{2}{3} \nabla \cdot v)$ ,  $I$  is the unit tensor,  $q$  the heat flux vector given by Fourier's Law,  $q = -k \nabla T$ ,  $\mu$  the dynamic viscosity,  $k$  is thermal conductivity, and  $\gamma$  the specific heat ratio for the gas. The vector quantity  $f$  is the external body force per unit mass (acceleration) acting on the fluid. For this model there is no additional

body force acting on the neutral gases. Furthermore, the physical geometry and flow fields are axisymmetric [76].

When a high-pressure gas goes through an orifice into a stagnant low-pressure chamber, the gas rapidly expands and results in the formation of an under-expanded free jet. A schematic diagram of the under-expanded free jet is shown (Figure 2.10). At the orifice, the flow is for the most part supersonic. The upstream high-pressure gas is, therefore, unaffected by the downstream flow conditions and the jet structure must adjust to match the backing-pressure in the low pressure chamber. The resulting free-jet flow is quite complex and characterized by thin non-isoentropic regions (shocks) with large gradients in the properties of the gas. The key features of an under-expanded free jet include the: (i) barrel (intercepting) shock; (ii) jet boundary; (iii) triple point; (iv) Mach disc; and (v) reflected shock.

The free-jet expansion process can be understood as follows. Expansion waves form at the exit of the orifice/nozzle as the flow expands into the low-pressure chamber. Figure 2.10 shows a schematic of free jet flow shock structure. The expansion waves extend to the free-jet boundary and reflect against it as weak compression waves to the high pressure region created. The reflected compression waves coalesce to form the intercepting shock in the interior of the jet. Depending on the flow conditions, the intercepting shock may reflect regularly at the centreline or it may terminate in a triple-point Mach disc configuration (as in all the cases to be considered herein). The Mach disc is a slightly curved shock (the Mach disc is normal to the flow at the jet axis), behind which is a large region of subsonic flow bounded by a slipstream emanating from the triple point. The flow across the oblique intercepting shock remains supersonic but has a lower Mach number than the flow in the core of the jet. The flow downstream of the shock that reflects from the interaction of the intercepting shock and the Mach disc is also supersonic.

The numerical solution of the under-expanded free-jet flow of nitrogen is shown (Figure 2.11). The figure depicts the predicted flow streamlines and computed distributions of Mach number  $M = |v|/a$ , where  $a$  is the speed of sound, and entropy change  $\Delta s = (R/(\gamma - 1))\ln((p/p_0)/(\rho/\rho_0^\gamma))$ . The black coloured streamlines are associated with neutral gas flow that passes through the Mach disc whereas the white coloured

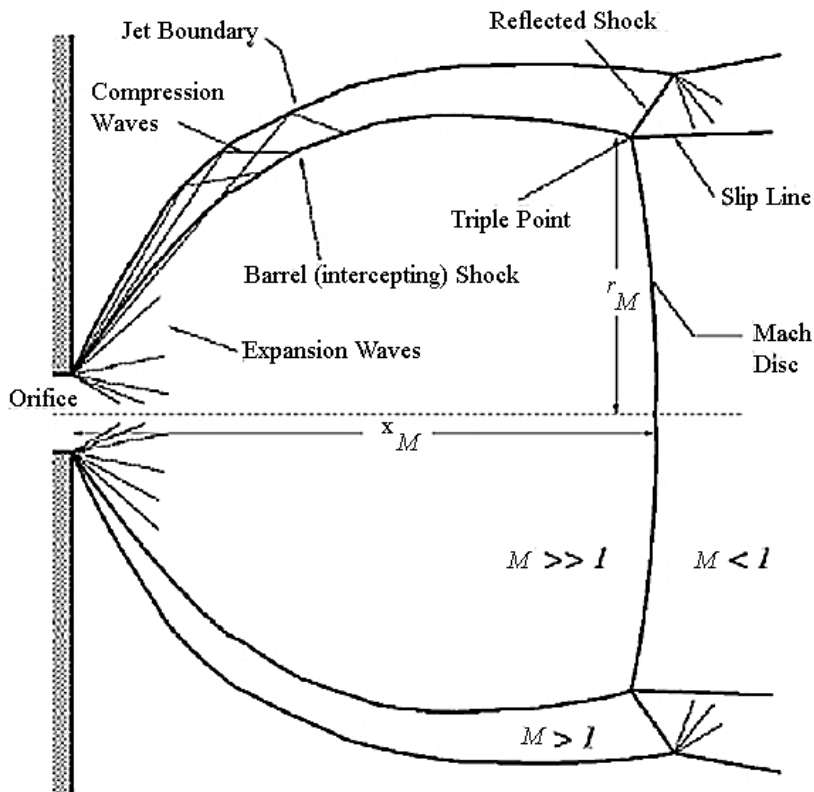


Figure 2.10: Schematic of supersonic free jet expansion with flow structure.

stream traces are associated with flow that passes through a region above the triple point via the intercepting shock. The purple coloured streamline marks the boundary between the flow passing through the Mach disc and flow passing above the triple point. The green coloured stream traces reflect the viscous entrainment of the low-pressure reservoir gas into the free jet flow that occurs in the mixing layer at the jet boundary. The flow is highly expanded downstream of the orifice. The pressure decreases by five orders in magnitude in the free jet and then increases abruptly again following the Mach disc to match the background pressure. The density and temperature also decrease and the flow speed increases monotonically. The Mach number exceeds 12 in the core region of the jet. The intercepting shock, jet boundary, triple point, Mach disc, and reflected shock are all quite evident in the predicted entropy and Mach number distributions and appear to be well resolved.

This calculations give us a clear picture of flow structure in free jet expansion, but



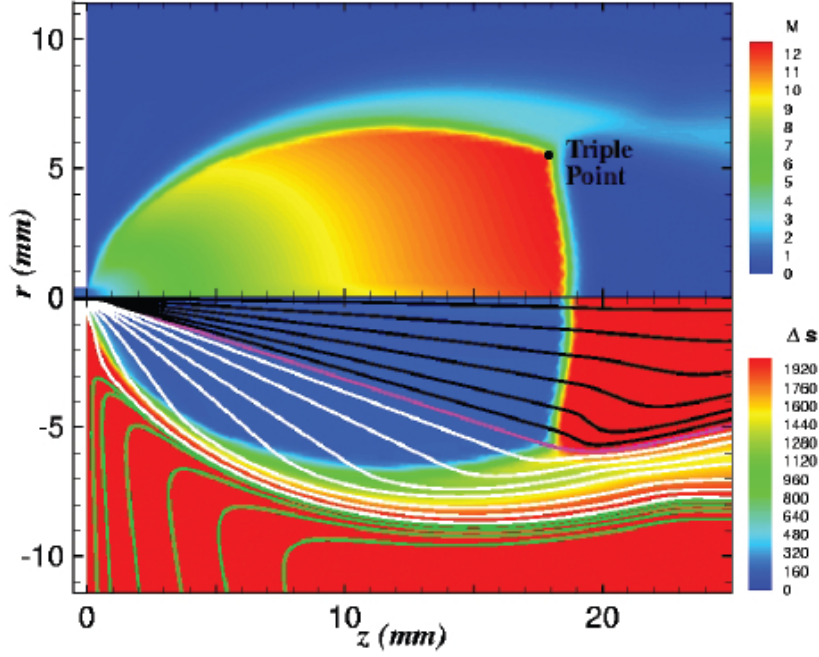


Figure 2.11: Computed flow streamlines and distributions of Mach number,  $M$ , and entropy change,  $s$ , for axisymmetric under-expanded free-jet flow with.

this model is too complicated to use for simple estimation. Instead, estimations based on the idealized continuum model [77] can be used. At high source pressures, the effect of gas viscosity and heat transfer may be neglected, and the gas flow can be treated as an adiabatic, isentropic expansion. The adiabatic assumption leads to the conservation of the sum of enthalpy and the kinetic energy of directed mass flow as the gas expand to the vacuum:  $H(x) + \frac{1}{2}mu(x)^2 = constant$ , where  $H(x)$  is the molar enthalpy of gas at the position  $x$  from the point of expansion and  $u(x)$  the average velocity at this position. This equation limits the ultimate flow velocity to the value  $u_{max} = \sqrt{\frac{2H(T_0)}{m}}$ , where  $H(T_0)$  is the molar enthalpy of the gas at the temperature of the source reservoir,  $T_0$ . For calorically perfect gases which have a constant-pressure molar heat capacity,  $C_p$ , that is independent of temperature,  $H(T)$  is given as  $C_pT$ , and the ultimate flow velocity becomes

$$u_{max} = \sqrt{\frac{C_p T_0}{m}}$$

For an ideal monatomic gas,  $C_p = \frac{5}{2}R$ , and thermal velocities can be predicted. For

example He, Ne, Ar, Kr, and Xe expanding from a reservoir at 300 K will have velocities of  $1.77 \cdot 10^5$ ,  $7.86 \cdot 10^4$ ,  $5.59 \cdot 10^4$ ,  $3.86 \cdot 10^4$ , and  $3.08 \cdot 10^4$  cm s<sup>-1</sup> respectively.

For calorically perfect ideal gases [defined by the relationship  $dH = C_p dT$  (with  $C_p$  independent of temperature) and the ideal gas law,  $p = \rho kT$  ], adiabatic isentropic expansion from a reservoir at conditions  $(P_0, T_0, \rho_0)$  then gives;

$$\frac{T_1}{T_0} = \left(\frac{P_1}{P_0}\right)^{(\gamma-1)/\gamma}; \quad \frac{\rho_1}{\rho_0} = \left(\frac{P_1}{P_0}\right)^{1/\gamma}; \quad \text{and} \quad \frac{\rho_1}{\rho_0} = \left(\frac{T_1}{T_0}\right)^{1/(\gamma-1)},$$

where  $\rho$  is the density of the gas and  $\gamma$  is the heat capacity ratio  $C_p/C_v$ , equal to 1.6666 (5/3) for monatomic gases, 1.4 (7/5) for diatomic gases ignoring vibrations, and 1.2857 (9/7) for diatomic gases at high temperature where vibrations contribute  $Nk$  to the heat capacity. This equation implies that an expansion carried out with a large pressure ratio will lead to the large reduction in temperature.

The propagation of sound in gases is also an example of adiabatic, nearly isentropic process, and the speed of sound  $a$ , in an ideal gas is given as

$$a(T) = \sqrt{\frac{\gamma RT}{m}}$$

The Mach number,  $M(x)$ , is then defined as the ratio of the average flow velocity of the expanding gas at the position  $x$ ,  $u(x)$  to the local speed of sound of the gas  $a(x)$ , i.e.,  $M(x) = u(x)/a(x)$ . The substantial cooling associated with gas supersonic expansion reduces the local speed of sound of the expanding gas tremendously, while the average flow velocity,  $u(x)$ , increases as random motion is converted into direct mass flow (but never exceeding  $u_{max}$ , as discussed earlier). The expansion is said to become supersonic when the ratio  $u(x)/a(x)$  (or the Mach number  $M(x)$ ), increases beyond unity. Experimentally it is not difficult to achieve Mach numbers of 20 or greater in supersonic expansion.

Combining the previous equations it is possible to express the temperature, pressure, and density ratios in terms of Mach number,  $M(x)$ , as

$$\frac{T(x)}{T_0} = W^{-1}; \quad \frac{\rho(x)}{\rho_0} = W^{-1/(\gamma-1)}; \quad \frac{P(x)}{P_0} = W^{-\gamma/(\gamma-1)},$$

Where  $W = 1 + \frac{\gamma-1}{2}M(x)^2$

Finally, the functional dependance of the Mach number on downstream distance,  $x$ , can be calculated using formula

$$M(x) = A\left(\frac{x-x_0}{D}\right)^{\gamma-1} - \frac{1}{2} \frac{[(\gamma+1)/(\gamma-1)]}{A[(x-x_0)/D]^{\gamma-1}}$$

Where  $D$  is orifice diameter, and  $x_0/D$  and  $A$  depends on  $\gamma$ .

One can obtain the asymptotic expression for the temperature, pressure, and density ratio at the large distances  $x/D$  as

$$\frac{T(x)}{T_0} = B\left(\frac{x-x_0}{D}\right)^{-2(\gamma-1)}; \quad \frac{P(x)}{P_0} = C\left(\frac{x-x_0}{D}\right)^{-2\gamma}; \quad \frac{\rho(x)}{\rho_0} = f\left(\frac{x-x_0}{D}\right)^{-2};$$

The idealized continuum model assumes that collisions occur with sufficient frequency to be maintained throughout the expansion process. At some point in the expansion, however, the collision frequency drops to such low levels that a particular degree of freedom may fall out of equilibrium. This is the beginning of transition from continuum flow to free molecular flow, which ultimately leads to gas molecules isolated in a (nearly) collision-free environment. Generally, rotational relaxation occurs more readily than vibrational relaxation, and the translational energy exchange occurs even more easily than rotational relaxation. For these reasons, it is typically the vibrational degrees of freedom which fall out of the equation first, followed by the rotational degrees of freedom. Finally the collisions become so infrequent that translational equilibration ceases, and the continuum model becomes invalid.

Making some simple assumption concerning the effectiveness of collision energy transfer, it can be shown that a real supersonic expansion will reach the terminal Mach number,  $M_T$ , beyond which no further cooling occurs. Assuming a single component gas in the reservoir, this may be written as

$$M_T = G(\sqrt{2}\sigma\rho_0 D_\varepsilon)^{(\gamma-1)/\gamma}$$

In any real apparatus, the idealized continuum model will also break down when the expanding gas becomes sufficiently rarefied that its density approaches that of background gases. At this point collisions between the background gases and the expanding gas cause the molecular velocity distribution to be randomized, so that the expansion becomes irreversible, leading to a serious increase in entropy. If the background gas density is high, the expansion travels through a shock zone where molecules are rapidly decelerated. If the background density is low, a molecule in the jet experiences a series of individual scattering events, and the randomization of the velocity distribution occurs over an extended region of space. The thickness of the shock zone thus depends on the density of the background gas. As it was already shown, there are two types of shock zones that develop. A barrel shock zone forms around the centered line of the expansion, resembling a paraboloid of revolution centered on the jet axis, opening from the expansion orifice. This ends at the second shock zone, called the Mach disk, forms a nearly flat terminal shock wave perpendicular to the center line of the beam.

The location of Mach disk depends only on the ratio between the source and background pressures,  $P_0$  and  $P_B$  and can be expressed in a simple formula

$$x_M = 0.67D\sqrt{\frac{P_0}{P_B}}$$

In current experimental setup the estimated distance to the Mach disk is approximately 7-12 cm (depend on backing pressure). This is important to know if one wants to detect the fluorescence signal from the zone of silence.

#### 2.4.4 Ablation source design

As opposed to the other ablation source used in our our group, which was designed specifically to produce large pure-carbon chains, in our source the ablation laser beam is collinear with molecular beam (Figure 2.12). Experiments show that this orientation

significantly improves the pulse to pulse stability of the source. The rod inside the source

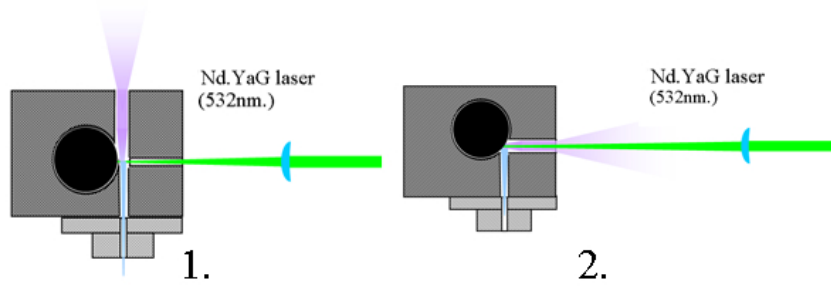


Figure 2.12: Ablation source scheme. 1.-traditional design; 2.-this work.

(Figure 2.13) is rotated and translated so that a fresh surface is continuously exposed to the laser (25 mJ/9 ns pulse of 532 nm Nd:YAG, focused into 0.3 mm spot) which is fired to coincide with an inert gas flow over the target area. Vaporized material is swept through a 10 mm long and 3 mm diameter tube with a buffer gas under 3-10 bar backing pressure and expanded into a vacuum chamber. At the laser spot on the rod the plasma is constricted at high buffer pressure. This makes clustering reactions in the plume of the material vapor rapid compared with the diffusion speed. Varying the length

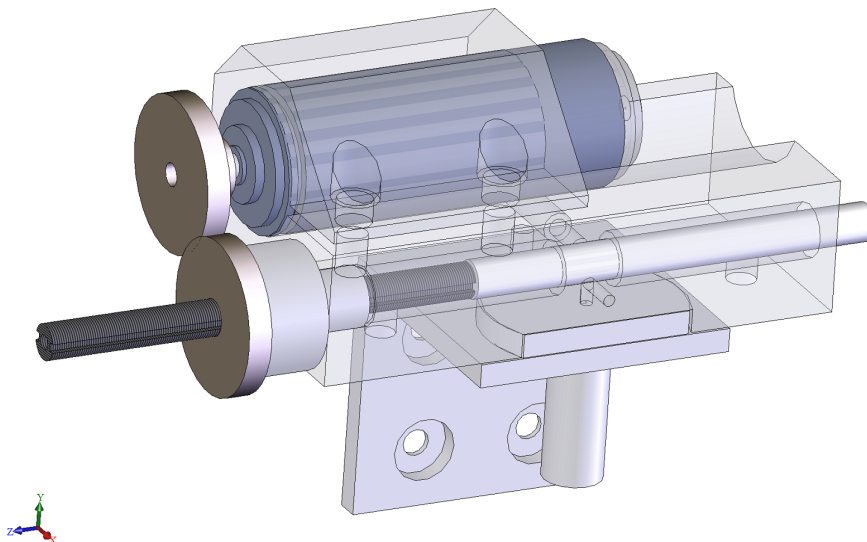


Figure 2.13: One rod ablation source.

of channel by attaching the extenders, the masses of produced molecules can be shifted. The pressure can be varied from 3.5 to 10 bar in order to optimize production of a specific molecule. However, this will also affect the reaction products cooling efficiency, which should be kept in mind when doing such optimizations. Mostly, metal-capped carbon chains are been sought for. To produce such kind of molecules, mixtures of methane or acetylene in argon are passed over the ablated metal rod. In this case a number of different species are produced, sometimes resulting in overlapping spectra, which make the assignments extremely complicated. In order to reduce the number of species, hydrogen has been eliminated from the precursor components by creating a double rod source. (Figure 2.14). To prove the effectiveness of the double rod source the spectra of  $\text{AlC}_2$  was

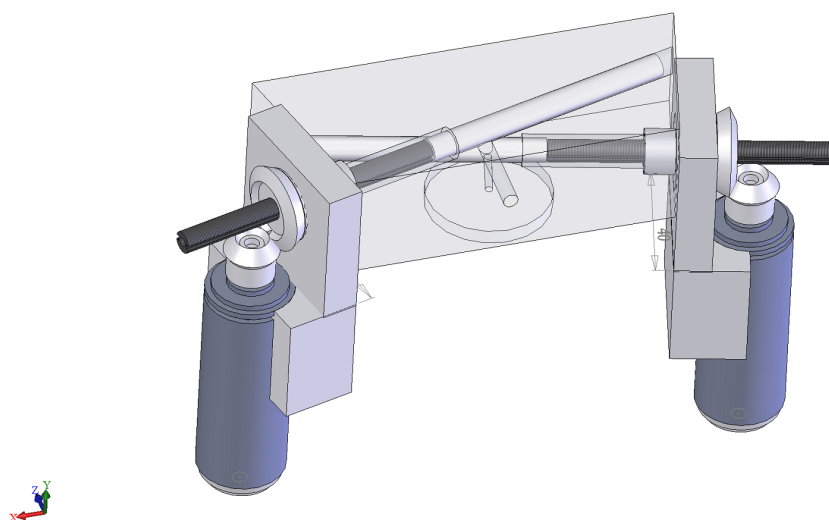


Figure 2.14: Double-rod ablation source.

obtained (Figure 2.15). Comparison of this spectrum with the one from one rod source (Figure 2.13) shows a good agreement with one another. The rotational temperature in the case of using the double rod source is little too high. The reason is the bigger diameter of the source channel decrease the "backing" pressure and makes jet cooling less efficient. The diameter of the source channel has to be increased because the both rods must be

ablated.

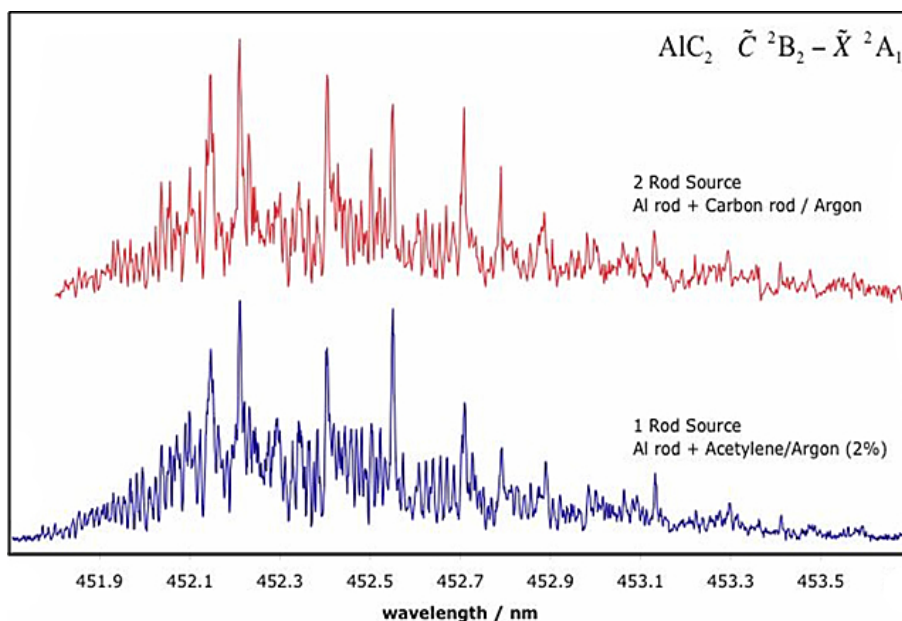


Figure 2.15: The origin band of the  $\tilde{C}^2B_2 \leftarrow \tilde{X}^2A_1$  transition of  $AlC_2$  with comparison of single (bottom) and double (top) rod source.

In the case of  $AlC_2$ , a combination of aluminum and graphite rods was used, and pure argon as a carrier gas. To ablate both rods the laser beam (40 mJ/9 ns pulse 532 nm of Nd:YAG laser) was split in two, and the positions of the focused lasers spots was adjusted separately.

## 2.5 Optical system

### 2.5.1 Baffle system

An important characteristic of the experimental setup is the signal-to-noise ratio. In the case of the LIF experiment, scattered light is the dominant source of noise. There are several ways to reduce scattered light, such as painting everything inside the LIF chamber black or collecting fluorescence signal only from a certain point in space. Most effective is to guide properly the probe laser beam through the LIF chamber. The baffle system used during this thesis (Figure 2.16) was designed in collaboration with Prof. Alan Knight,

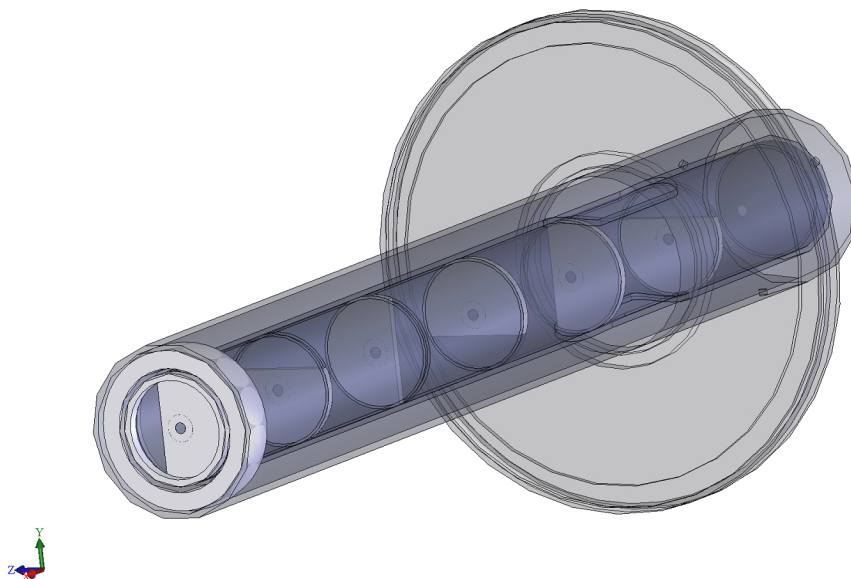


Figure 2.16: 3D scheme of the baffle system used in this work. It is composed of six irises with increasing diameter.

It consists of two sets of anodized aluminum irises fixed inside two metal pipes. The opposite sides of these pipes are fixed in flanges through teflon spacers and the other ends are fixed in proper position with a screw, to allow one to adjust the position of the tubes. All irises are adjusted in a such way that the centers of each are on one straight line. The diameters of the irises are slowly increasing in the direction the laser beam follows. Such a baffle system, together with blackening the inner walls of the LIF chamber, allows one to significantly reduce scattered light and therefore a large amount of experimental noise.

## 2.5.2 Optical system

The fluorescence radiation is collected perpendicular with respect to the laser beam. The light collection assembly (Figure 2.17) consists of two stationary lenses and a PMT holder with adjustable slits. The first lens ( $f=60$  mm) is mounted 60 mm away from the plane formed by crossing of probe laser and molecular beam axis. The second lens focuses light to the slits. Fine adjustment is achieved by shifting the PMT holder with slits in two



dimensions and rotating the slits. Two types of PMT were used, Hamamatsu type R374 Multialkali photocathode for UV - near IR range, 11-stage and R5929 type with prismatic window, 11stage, with high cathode sensitivity and electron transit time 60 ns for both. The sensitivity curves plotted in (Figure 2.18).

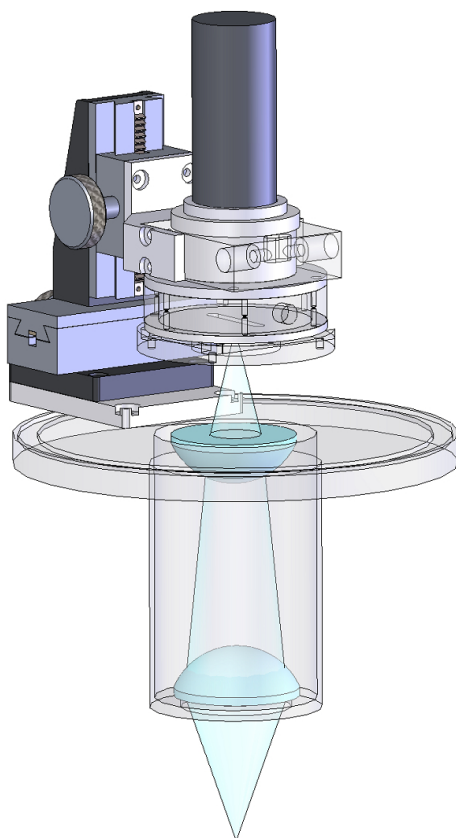


Figure 2.17: Optical arrangement of experimental setup.

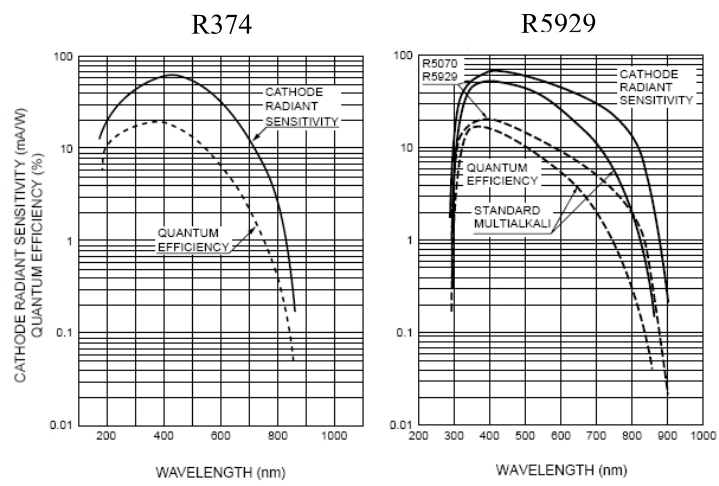


Figure 2.18: PMT sensitivity.

### 2.5.3 Radiation sources

Different tunable lasers were used in the experiments, depending on the spectral region investigated and the line-width required to resolve the rotational structure (Figure 2.19).

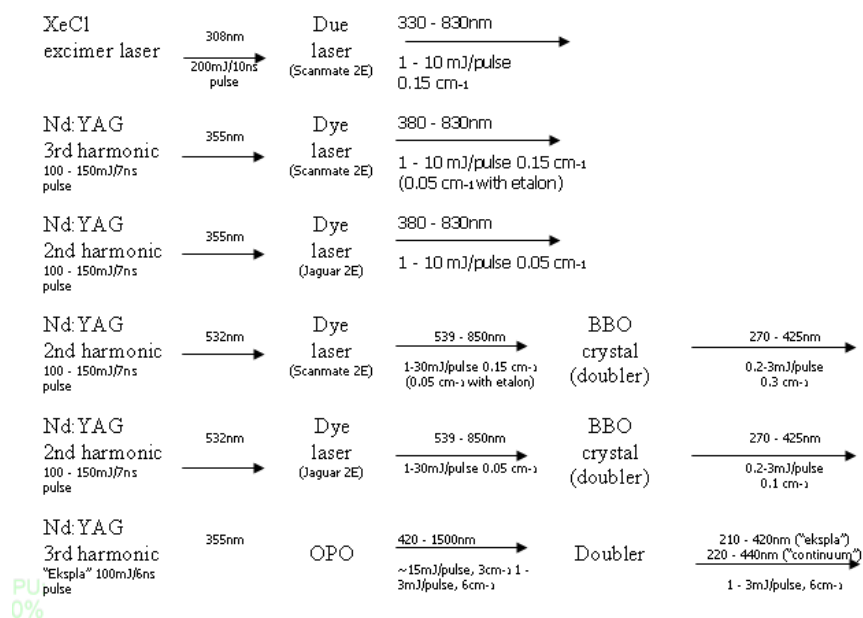


Figure 2.19:

### 2.5.4 Wavelength calibration

An important consideration in these studies is an accurate calibration of the laser wavelength. It is not sufficient to rely on the calibration provided by the laser drive electronics, because this varies as a function of diffraction grating angle, dye refractive index, laser optimization and initial laser set-up. To determine the actual laser wavelength, an external Burleigh WA-4500 pulsed wavemeter was therefore employed. This wavemeter contains two etalons: a wedged one is used to obtain an initial wavelength value (0.05 nm), and a fixed air gap FabryPerot etalon which has a resolution of 0.001 nm. The wavemeter compares the unknown laser to that of an internal HeNe reference laser. The wavelength range of the WA-4500 wavemeter is from 400 to 1100 nm, however for calibration in UV

region, the pre-doubled radiation from the dye laser was used. The wavelength of the HeNe reference laser is 632.8197 nm in air, whereas it was expected that the wavemeter would be accurate near this wavelength, where much of this work was carried out. To calibrate the pulsed wavemeter in the other regions, well-known atomic lines were used. The absolute wavelength accuracy is estimated as being around  $\pm 0.005$  nm based on the calibration of the wavemeter. The relative accuracy is around  $\pm 0.002$  nm, the largest contribution to the relative inaccuracy being due to non-linearity of the laser grating stepper-motor.

## 2.6 Data acquisition.

The data acquisition program was built using the LabView software. The program controls the laser wavelength and collects data from the oscilloscope (triggering of the setup occurs independently from the program). Each cycle of collecting data starts when the computer, through the RS-232 interface, sets a new wavelength for the laser. When the laser confirms that it has accepted the correct position, the computer sends a command to the oscilloscope (through GPIB) to collect and average data for N pulses, typically 1-100 laser shots. The oscilloscope will collect N pulses, average them, and send the data back to the computer. In the program one can set 5 different time gates to calculate the average signal inside each one. Usually the first gate collects the signal before the excitation pulse occurs, and uses this pulse for background subtraction from the other gates. Thus, background fluctuation are significantly decreased. Data from the gates, as well as wavelength position, are saved in to the file.

As an option, during the scan, data from the wavemeter can be collected, for calibration in real-time. Data from the wavemeter is also saved to the file. In the case of using the dye laser with an etalon or the narrow band dye laser, the program directly operates the laser step-motors.

## 2.7 Expansion temperature profile

To find the optimal position for the laser probe beam, it is important to know how the rotational temperature of the molecules change with distance from the source. The rotational temperature can be analyzed using the intensity distribution of rotational lines. For the intensity of the absorption line one can write [78]:

$$I_{abs} = \frac{C_{abs.\nu}}{Q_r}(J' + J'' + 1)e^{-B''J''(J''+1)hc/kT}$$

Where  $C_{abc}$  is constant depending on the change of dipole moment and the total number of molecules in the initial vibrational level  $Q_r$ , so-called state sum.

Combination of:  $\frac{C_{abs.\nu}}{Q_r}(J' + J'' + 1)$  can be replaced by line strength  $S_J$  which can be derived from Hönl-London equation:

For  $\Delta\Lambda=0$

$$S_J^R = \frac{(J'' + 1 + \Lambda'')(J'' + 1 - \Lambda'')}{J'' + 1} = \frac{(J' + \Lambda')(J' - \Lambda')}{J'}$$

$$S_J^Q = \frac{(2J'' + 1)\Lambda''^2}{J''(J'' + 1)} = \frac{(2J' + 1)\Lambda'^2}{J'}$$

$$S_J^P = \frac{(J'' + \Lambda'')(J'' - \Lambda'')}{J''} = \frac{(J' + 1 + \Lambda')(J' + 1 - \Lambda')}{J' + 1}$$

For  $\Delta\Lambda=+1$

$$S_J^R = \frac{(J'' + 2 + \Lambda'')(J'' + 1 + \Lambda'')}{4(J'' + 1)} = \frac{(J' + \Lambda')(J' - 1 + \Lambda')}{4J'}$$

$$S_J^Q = \frac{(J'' + 1 + \Lambda'')(J'' - \Lambda'')(2J'' + 1)}{4J''(J'' + 1)} = \frac{(J' + \Lambda')(J' + 1 - \Lambda')(2J' + 1)}{4J'(J' + 1)}$$

$$S_J^P = \frac{(J'' - 1 - \Lambda'')(J'' - \Lambda'')}{4J''} = \frac{(J' + 1 - \Lambda')(J' + 2 - \Lambda')}{4(J' + 1)}$$

For  $\Delta\Lambda = -1$

$$S_J^R = \frac{(J'' + 2 - \Lambda'')(J'' + 1 - \Lambda'')}{4(J'' + 1)} = \frac{(J' - \Lambda')(J' - 1 - \Lambda')}{4J'}$$

$$S_J^Q = \frac{(J'' + 1 - \Lambda'')(J'' + \Lambda'')(2J'' + 1)}{4J''(J'' + 1)} = \frac{(J' - \Lambda')(J' + 1 + \Lambda')(2J' + 1)}{4J'(J' + 1)}$$

$$S_J^P = \frac{(J'' - 1 + \Lambda'')(J'' + \Lambda'')}{4J''} = \frac{(J' + 1 + \Lambda')(J' + 2 + \Lambda')}{4(J' + 1)}$$

For this test we use the well known  $0 - 0 a \ ^3\Pi_u \longrightarrow d \ ^3\Pi_g$  transition of  $C_2$  at 516 nm. For this transition  $\Delta\Lambda = 0$ , therefore:

$$S_J^R = \frac{J''(J'' + 2)}{J'' + 1} = \frac{(J' + 1)(J' - 1)}{J'}$$

$$S_J^Q = \frac{(2J'' + 1)}{J''(J'' + 1)} = \frac{(2J' + 1)}{J'}$$

$$S_J^P = \frac{(J'' + 1)(J'' - 1)}{J''} = \frac{J'(J' + 2)}{J' + 1}$$

$$\text{R-lines: Intensity of } R(J) \propto \frac{J''(J'' + 2)}{J'' + 1} e^{-B'' J''(J'' + 1)/kT}$$

$$\text{P-lines: Intensity of } P(J) \propto \frac{(J'' + 1)(J'' - 1)}{J''} e^{-B'' J''(J'' + 1)/kT}$$

$$\ln\left[\frac{I(R(J)) * (J'' + 1)}{J''(J'' + 2)}\right] = K - \frac{B}{kT} J''(J'' + 1)$$

$$\ln\left[\frac{I(P(J)) * J''}{(J'' - 1)(J'' + 1)}\right] = K - \frac{B}{kT} J''(J'' + 1)$$

To define temperature one has to plot  $\ln\left[\frac{I(R(J)) * (J'' + 1)}{J''(J'' + 2)}\right]$  and  $\ln\left[\frac{I(P(J)) * J''}{(J'' - 1)(J'' + 1)}\right]$  against  $J''(J'' + 1)$  where the slope will be equal  $-\frac{B}{kT}$ .

Three different distances from the source orifice to the probe laser beam were used: 63, 45 and 27 mm. For each distance, a rotationally resolved spectra was obtained and analyzed. The assignment of lines is presented in (Figure 2.20). The analysis of lines

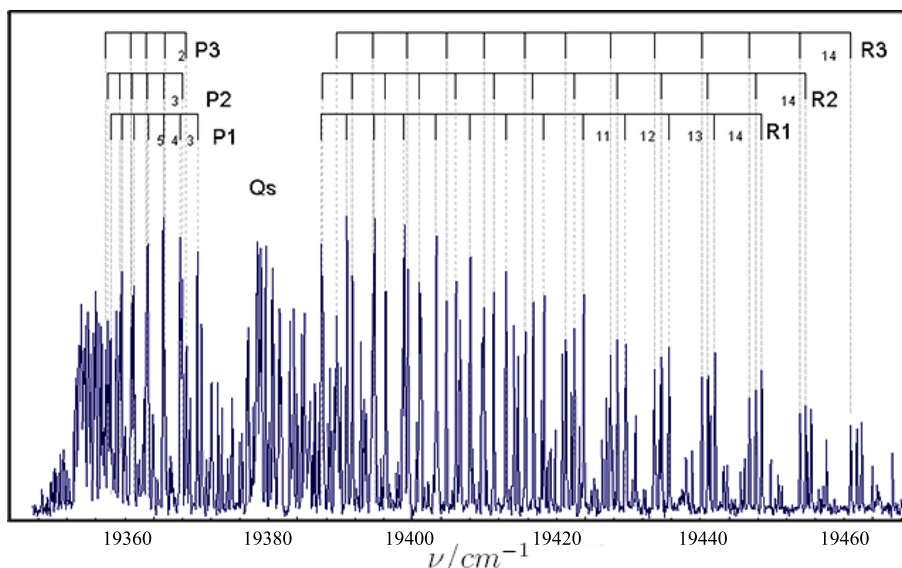


Figure 2.20: Rotation line assignment of  $C_2$   $0 - 0$   $a$   $^3\Pi_u \longrightarrow d$   $^3\Pi_g$  transition at 516 nm.

gives as temperature 66, 110, and 180 K, respectively. To prove that the temperature estimation was correct, a simple simulation in PGopher [79] was done. Comparison of the experimental spectrum with the simulation (Figure 2.21) shows a non-Boltzmann temperature distribution peculiar to  $C_2$  molecules [80]. For example, to lineup the maximum of P and R branches in the simulation with experiment (63 mm distance) one has to use a temperature equal to  $\sim 60$  K. However, to obtain the same band head temperature one must use  $\sim 120$  K, showing that this nonpolar diatomic molecule cools strangely in a free

jet expansion.

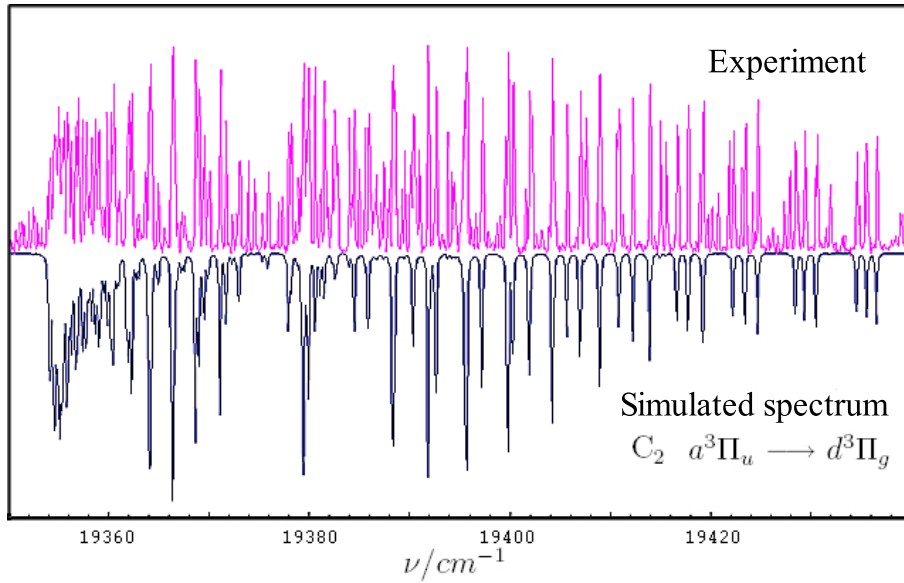


Figure 2.21: Comparison of experimental spectrum of  $C_2$   $0 - 0 a^3\Pi_u \rightarrow d^3\Pi_g$  with simulation (two temperatures).

To be sure that the temperature obtained is reasonable, the temperature were plot vs. distance. Then the extrapolation of temperature curve was compared with minimal temperature predicted from gas theory and with the expected position of Mach disk (Figure 2.22).

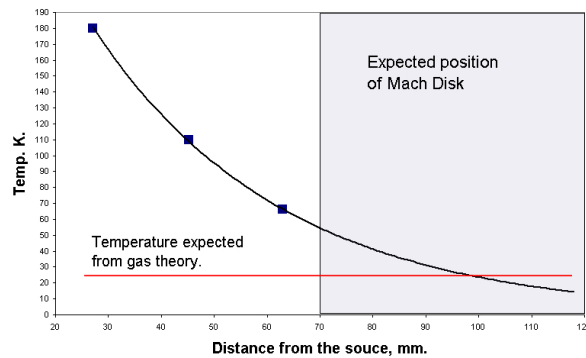


Figure 2.22: Dependence of beam temperature with the distance.

$C_2$  does not have a dipole moment, neither  $C_3$ . Therefore jet cooling is not very effective for both species. But in case of  $C_3$ , at distance 30 mm from the source orifice,



we observe the temperature  $\sim 70$  K. thus, one can expect that other molecules will have lower rotational temperature.

## 2.8 Molecular beam number density

As was already written before, it is important to know number density in the expanded beam. An estimation has already been made, but now, this will be done from an analytical point of view. The voltage on the oscilloscope ( $U$ ) is assumed to be:

$$U = N_{ph} \times N_{mol} \times C_{C_2} \times A$$

were  $N_{ph}$  number of photons,  $N_{mol}$  number of molecules, C the effective absorption cross section for  $C_2$ , and A is the constant describing the apparatus sensitivity, which can be calculated.

$$N_{ph} = \frac{P\lambda}{hc}$$

were P is "power" of laser. But the cross-section is still not known. In the experiment the fluorescence light is collected from the small cylindrical volume of space formed by the laser beam and slits. It is assumed that there are no multiphoton processes. In this case, if the power of the laser is increased from a particular power, saturation (Figure 2.23) will be obtained. In the case of saturation of the signal on the oscilloscope one can write:

$$U = A \times N_{mol} \text{ or } N_{mol} = U/A$$

A is a complex parameter dependent on the volume of space from where the fluorescence is collected, solid angle of optic system, cathode radiant sensitivity, gain of PMT, coupling resistance of the oscilloscope, and life-time of the transition. For the  $C_2$  transition at 516 nm, the cathode sensitivity  $S=50$  mV  $W^{-1}$ . The voltage on PMT is 1535 V, gain of PMT is  $G = 10^7$ , coupling resistor  $R=50$   $\Omega$ , the voltage on oscilloscope  $U=400$

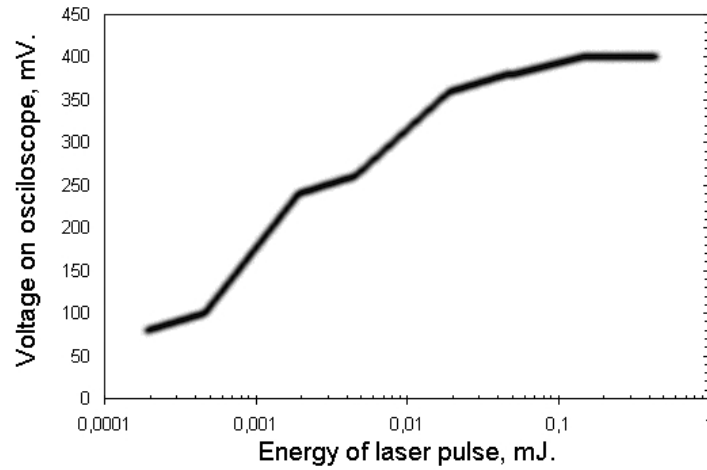


Figure 2.23: Voltage on PMT v.s. laser power.

mV.

Current through the PMT:

$$I = \frac{U}{R} = \frac{0.4}{50} = 0.008 A.$$

Power of light falling on cathode:

$$P = \frac{I}{S \cdot G} = \frac{0.008}{50 \cdot 10^{-3} \cdot 10^7} = 1.6 \cdot 10^{-7} \text{ W}$$

The energy of a photon on the PMT:

$$E = P \cdot \frac{1}{2} \cdot \tau = 1.6 \cdot 10^{-7} \cdot \frac{1}{2} \cdot 170 \cdot 10^{-9} = 1.36 \cdot 10^{-14} \text{ J}$$

The energy of single a photon:

$$E_{ph} = \frac{hc}{\lambda} = 3.85 \cdot 10^{-19} \text{ J (for 516 nm)}$$

Number of photons detected by PMT:

$$N_{PMT} = \frac{E}{E_{ph}} = 3.53 \cdot 10^4$$

It is assumed that the molecules emits light in all directions evenly. Therefore to obtain the number density in the observed volume,  $N_{V'}$ , we have to multiply  $N_{PMT}$  by a coefficient derived by ratio of optic system solid angle to solid angle of whole sphere:

$$N_{V'} = N_{PMT} \cdot 0.0434 = 8.13 \cdot 10^5$$

The diameter of the laser beam inside the chamber is approximately 1 mm. Slits are used to narrow the light collected so that scattered light can be avoided. Due to the use of these slits in the optical system, the fluorescence signal collected forms a cylinder approximately 5 mm long with a volume of 3.92 mm<sup>3</sup>. For 1 mm<sup>3</sup> there are  $2 \cdot 10^5$  molecules. The density in the molecular beam is assumed to be  $\propto \frac{1}{R^2}$ . For a small square volume of space at distance 63 mm from the source one can write:

$$\frac{4\pi R^2}{R^2} \cdot A \cdot \frac{s \cdot \Delta R}{4\pi R^2} = 2 \cdot 10^5 \quad A=8.18 \cdot 10^8.$$

A molecular beam can be estimated by a 90° cone. For the number of density within the beam in beam, one can write the integral:

$$N = C \int_0^{120mm} 4\pi R^2 \cdot A \cdot \frac{1}{R^2} dR = 4\pi C A R \Big|_0^{120mm},$$

Where  $C = \frac{\Omega(90^\circ)}{4\pi}$  is the coefficient derived from the solid angle.

The number of molecules in the beam is therefore  $N \sim 1.8 \cdot 10^{11}$  molecules.

# Chapter 3

## Preliminary experiments

Before searching for new molecules within a particular spectral region, the experimental apparatus was checked carefully to make sure everything works properly. During these tests a number of experiments were performed. In this chapter several well-known spectra will be presented. Reproducing spectra was a part of experimental adjustment procedure. The first spectrum observed was the  $A\ ^2B_2 \leftarrow X\ ^2A_1$  transition of  $\text{NO}_2$  [81]. For preliminary studies the chamber was filled with  $\text{NO}_2$ . A Lambda Physics Scanmate dye laser with a bandwidth  $0.15\ \text{cm}^{-1}$  was used. The scan was taken with a very large step size  $\sim 0.1\ \text{nm}$ . This spectrum (Figure 3.1) was reproducible, but due to the narrow bandwidth of the laser and the large step size, some lines are most probably missing. This makes comparison with published spectra complicated [81]. In theory, the use of a free-jet expansion decreases the rotational temperature, making spectra less complicated for interpretation. However, the laser step size was never decreased, making the spectrum in a free-jet expansion even less recognizable.

One of the methods for production of carbon chains is to put a hydrocarbon gases such as methane or acetylene through a discharge. Some of carbon-chain-related spectroscopic gas phase studies in the J.P. Maier group have been done using a pulsed pinhole discharge source. The next step in adjusting the LIF setup was to use the discharge source. By pulsing a 2% acetylene mixture in argon through the discharge source, the  $0-0\ A\ ^1\Pi_u \leftarrow X\ ^1\Sigma_g$  transition of  $\text{C}_3$  [82] was observed (Figure 3.2).

The rotation temperature was estimated to be  $\sim 70\ \text{K}$ . The efficiency of the discharge

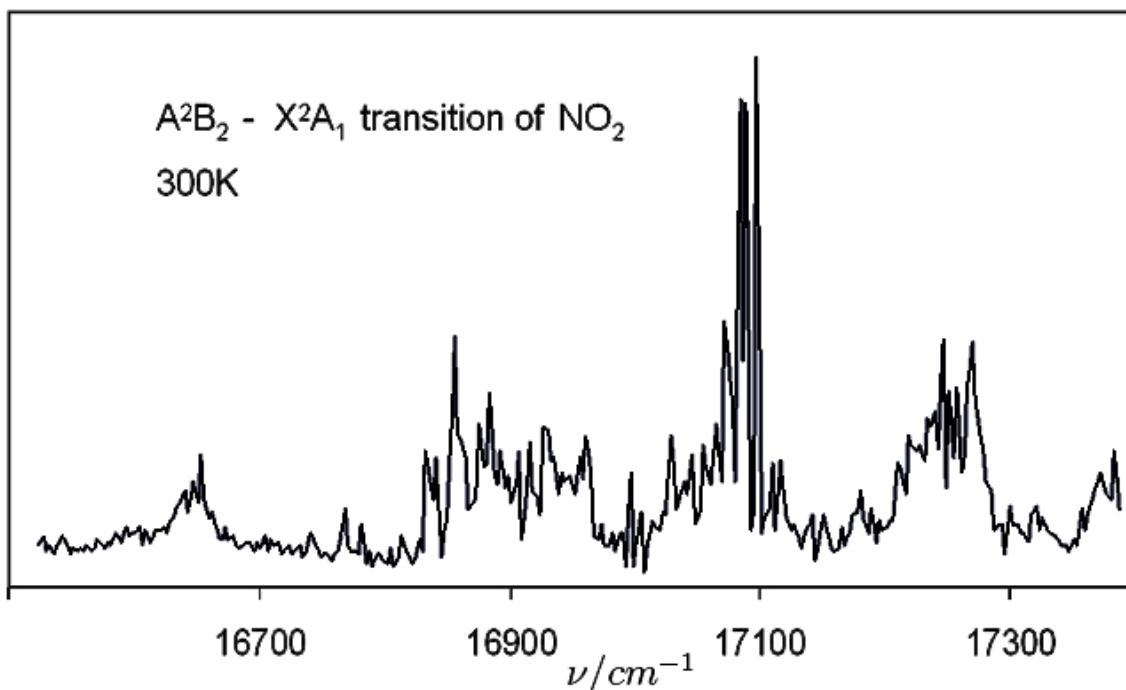


Figure 3.1: The  $A^2B_2 \leftarrow X^2A_1$  transition of gas-phase  $\text{NO}_2$  at 300K .

source was demonstrated.

The next step was to produce metal containing carbon chains. As a test molecule FeC was chosen. To produce FeC argon was bubbled through liquid  $\text{Fe}(\text{CO})_5$  and then the mixture was pulsed through the discharge source. The distance between the source and probe beam was  $\sim 40$  mm. The spectrum of  $[20,3] \ ^3\Delta_3 \leftarrow X \ ^3\Delta_3$  transition of FeC was observed (Figure 3.3). Actually only one of three components of spin-orbit splitting was observed [83].

Unfortunately, discharging a mixture of  $\text{Fe}(\text{CO})_5$  in argon destroys the electrodes and graphite deposits on the walls of the source canal. In this situation, the source must be cleaned every half an hour. Moreover, the stability of source was not good enough in comprising with already published data, observed with ablation. This was one reason to use an ablation source rather than a discharge source.

The testing of an ablation source was performed first with ablation of graphite rod in the presence of pulsed argon. The  $0 - 0 \ d \ ^3\Pi_g \leftarrow a \ ^3\Pi_u$  transition of  $\text{C}_2$  at 516 nm was observed. It was already describe in detail in the previous chapter. Also, the low

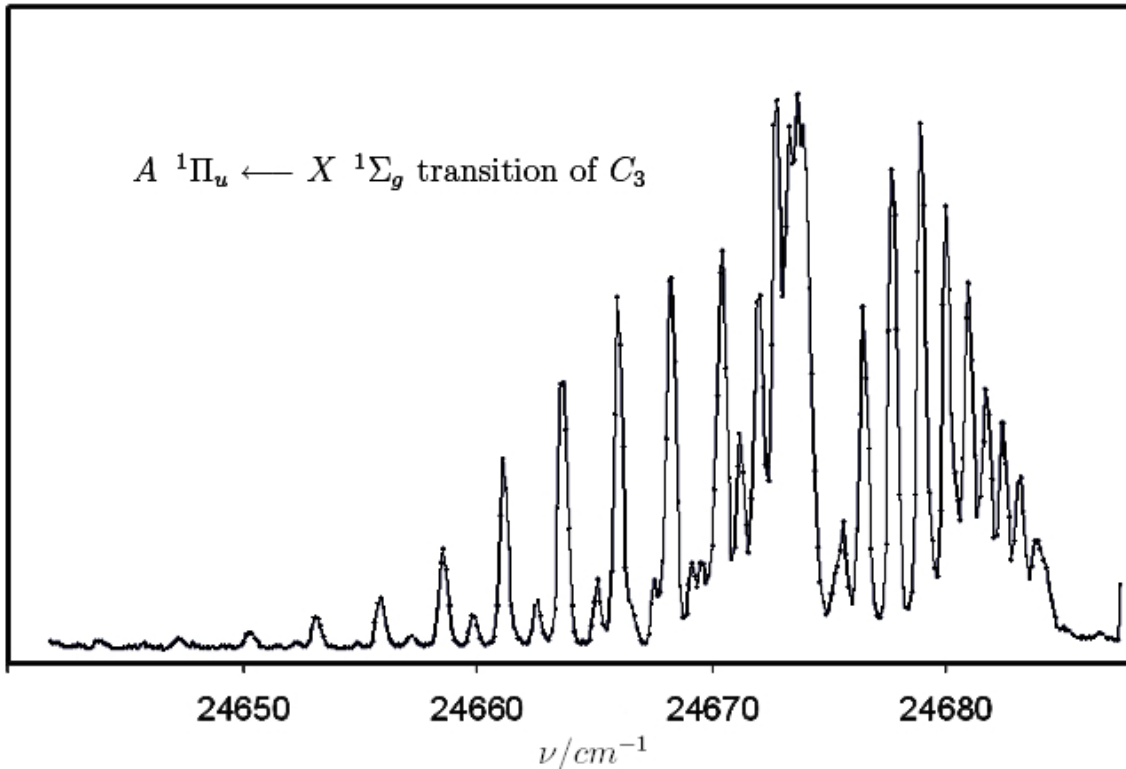


Figure 3.2: The  $0 - 0$   $A \ ^1\Pi_u \leftarrow X \ ^1\Sigma_g$  transition of  $C_3$  at a rotational temperature of  $\sim 70$ K.

resolution scan using an OPO (Ekspla) laser system covering the whole visible range was obtained (Figure 3.4).

To test an ablation source's capability to produce metal capped carbon chains a mixture of 1% acetylene in argon was pulsed over Mg rod. The spectra of MgH and MgCCH were observed.

An Al rod was tested next, and again, low resolution scans in visible region using an OPO (Ekspla) laser system were obtained. The scans were made with 1 % acetylene mixture in argon (Figure 3.6). In both cases the sample was contaminated with atmospheric air.

Two peaks of particular interest were scanned in high resolution ( $\Delta\tilde{\nu} \sim 0.1\text{cm}^{-1}$ ). The one at 445 nm was assigned to  $0-0$   $B \ ^4\Sigma^- \leftarrow X \ ^4\Sigma^-$  transition of AlC, which was previously reported [84]. The next band appeared more complicated. It was suspected to be an overlapping band system. The rotationally resolved spectra for AlC and AlO were

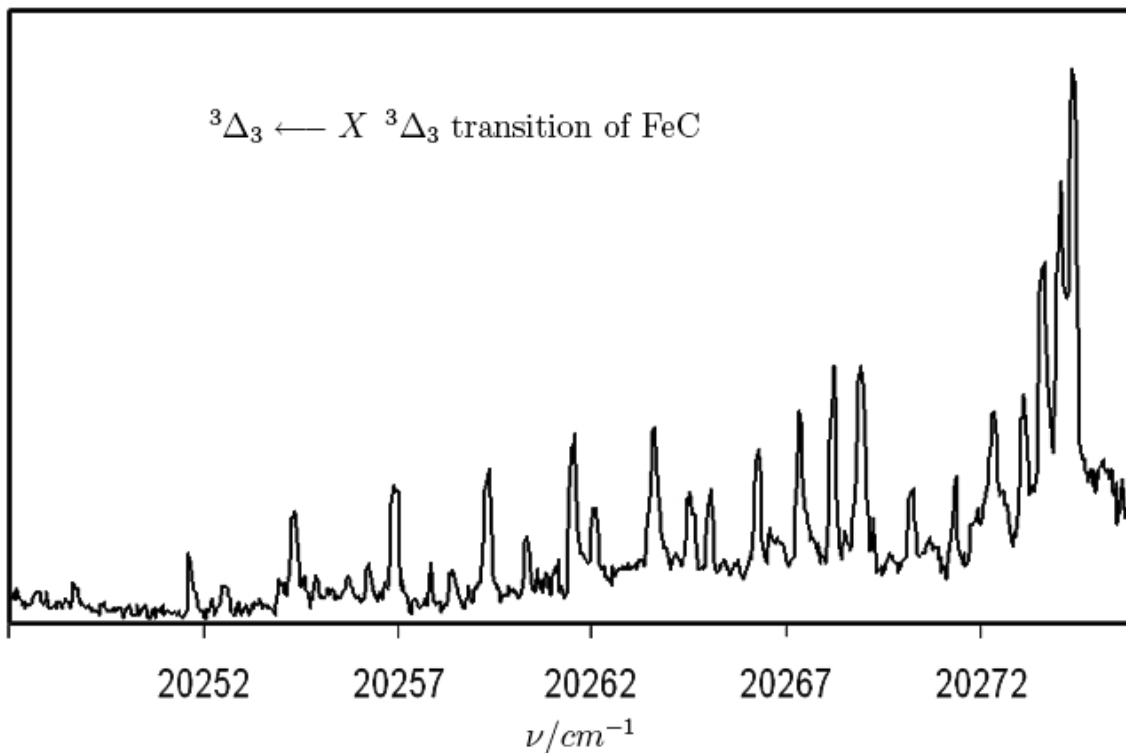


Figure 3.3: The  $[20,3]^3\Delta_3 \leftarrow X^3\Delta_3$  transition of FeC in gas-phase. Only one of three components of spin-orbit splitting was observed [83].

simulated in the "Diatomic" software package. A comparison with the experimental data (Figure 3.8) confirmed this assumption. This band can be assigned to an overlapping system of the 1-0  $B^4\Sigma^- \leftarrow X^4\Sigma^-$  transition of AlC and the 3-0  $B^2\Sigma^+ \leftarrow X^2\Sigma^+$  transition of AlO.

Recently, Mg terminated carbon chains were searched for in the blue-region of the visible spectra. The double rod source was used to exclude hydrogen from the system. Comparison of low resolution scans (Figure 3.9) reveal several interesting band systems which are expected to belong to magnesium carbon compounds containing no hydrogen. Unfortunately, with a high resolution laser ( $\Delta\nu \sim 0.08 \text{ cm}^{-1}$ ) these bands were not reproduced yet. Therefore, this band systems require further investigation.

In this way the capability of experimental setup to record spectra with reasonable S/N ratio was proven as well as the capability of various sources to produce some of the required species.

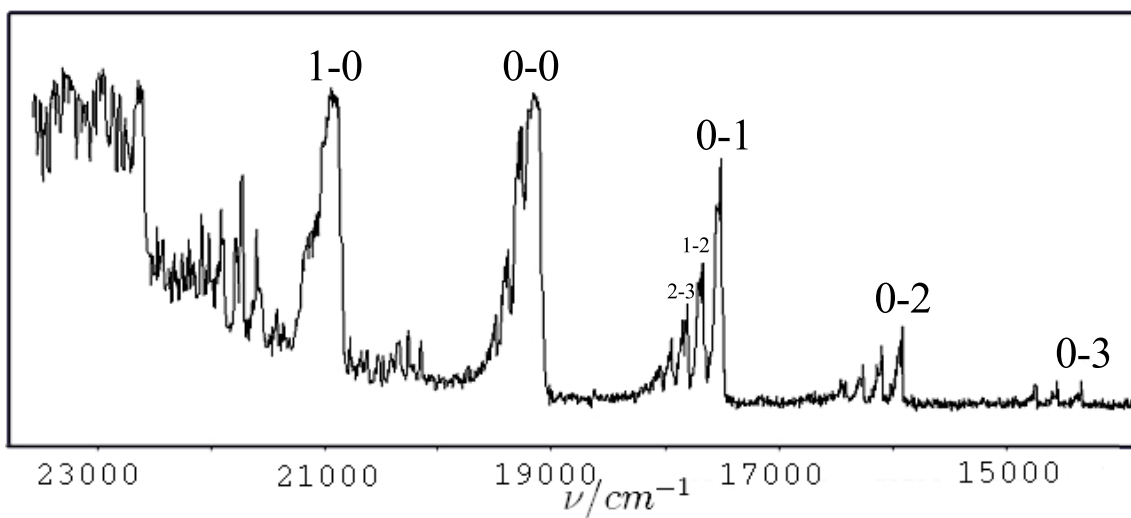


Figure 3.4: The vibrational bands of the  $a \ ^3\Pi_u \rightarrow d \ ^3\Pi_g$  electronic transition of  $C_2$ .

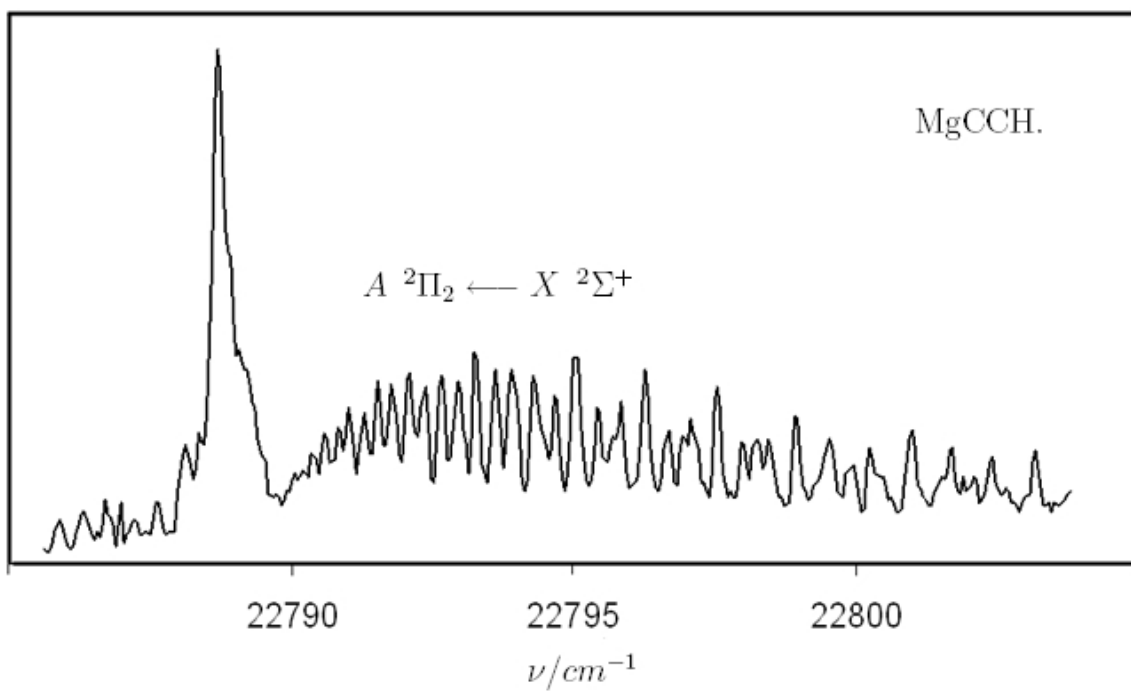


Figure 3.5: The  $A \ ^2\Pi_2 \leftarrow X \ ^2\Sigma^+$  transition of  $MgCCH$ .



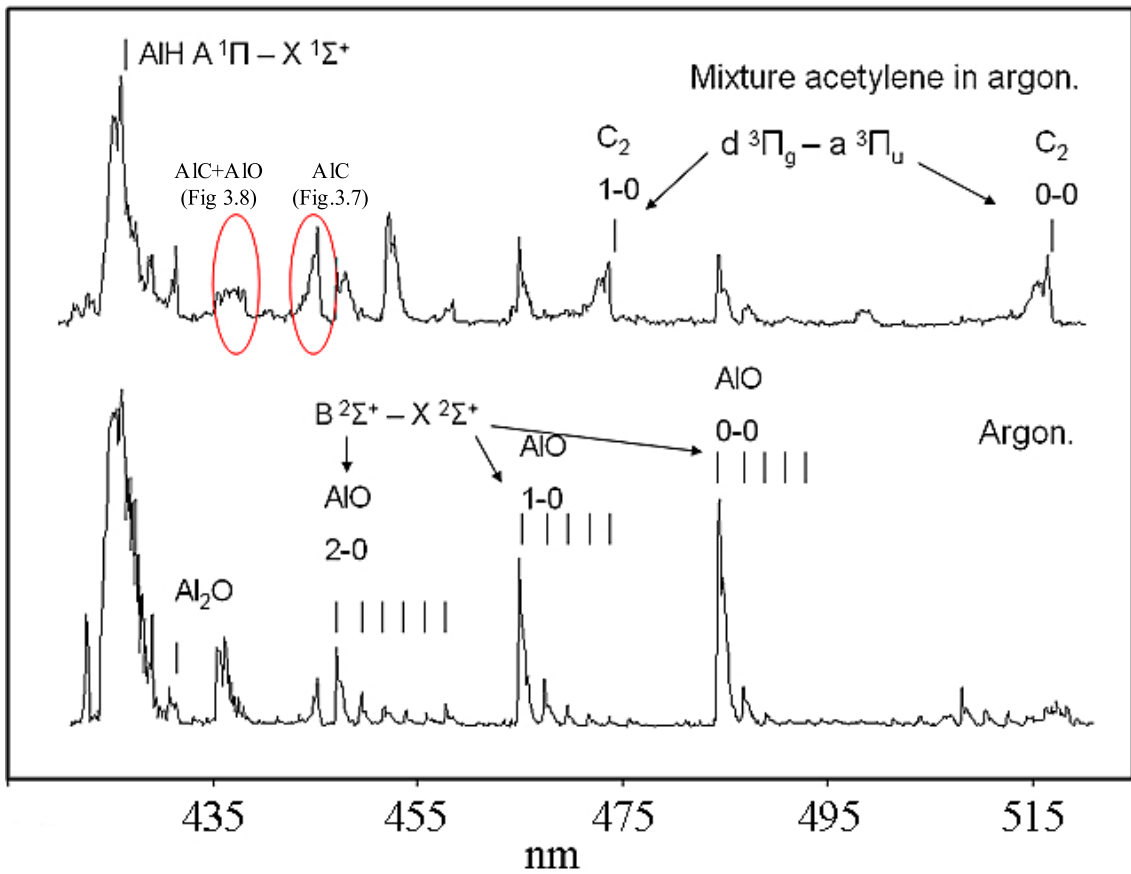


Figure 3.6: The low resolution spectra of an Al rod ablated with different gas mixtures.

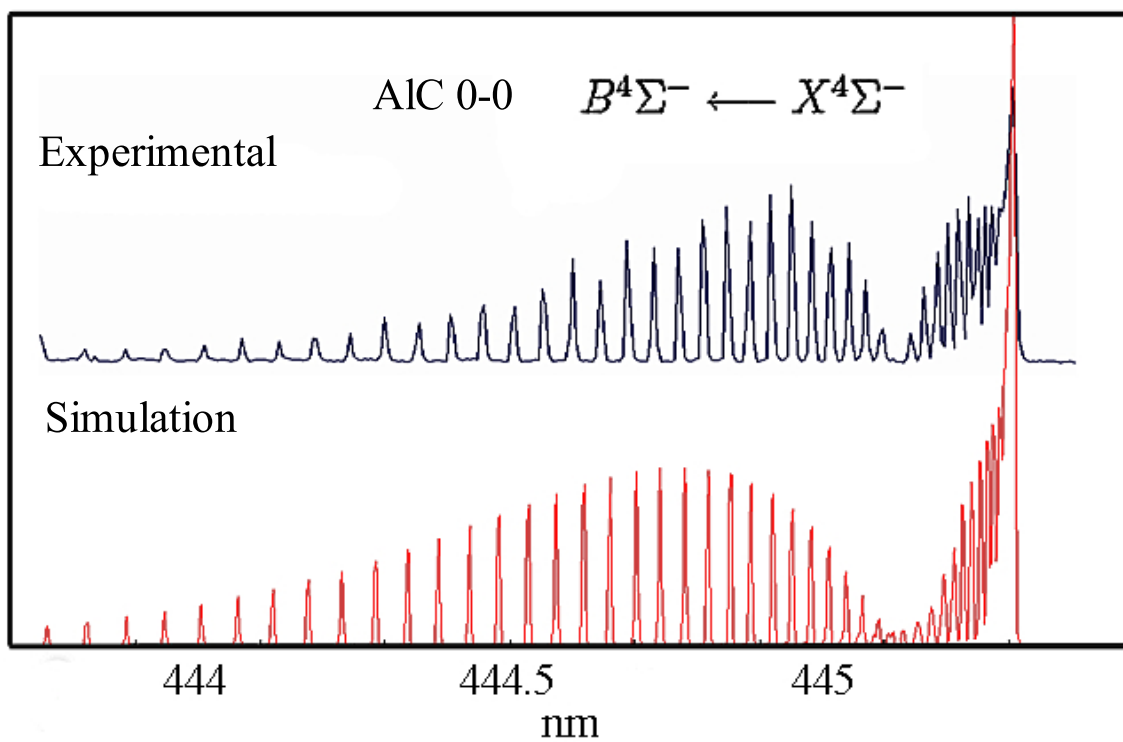


Figure 3.7: Comparison of the simulated 0-0  $B^4\Sigma^- \leftarrow X^4\Sigma^-$  transition of AlC with experimental data.

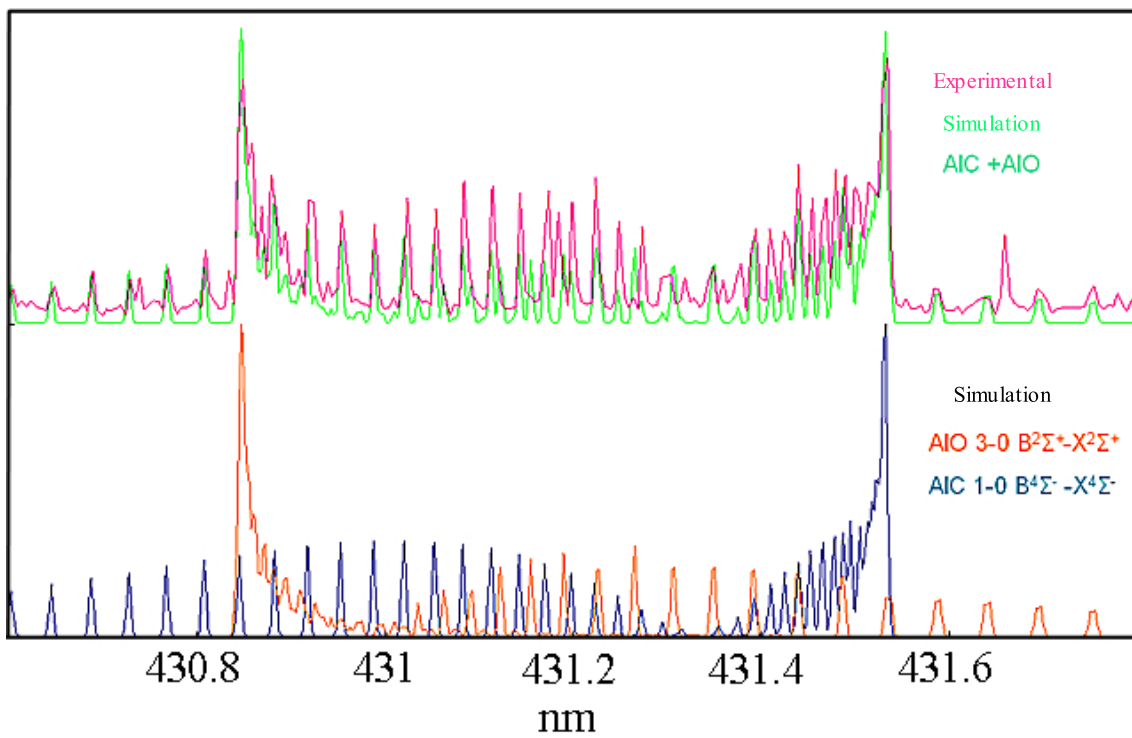


Figure 3.8: Comparison of the simulated  $1 - 0 B^4\Sigma^- \leftarrow X^4\Sigma^-$  transition of AIC and  $3 - 0 B^2\Sigma^+ \leftarrow X^2\Sigma^+$  transition of AIO with experimental observation.

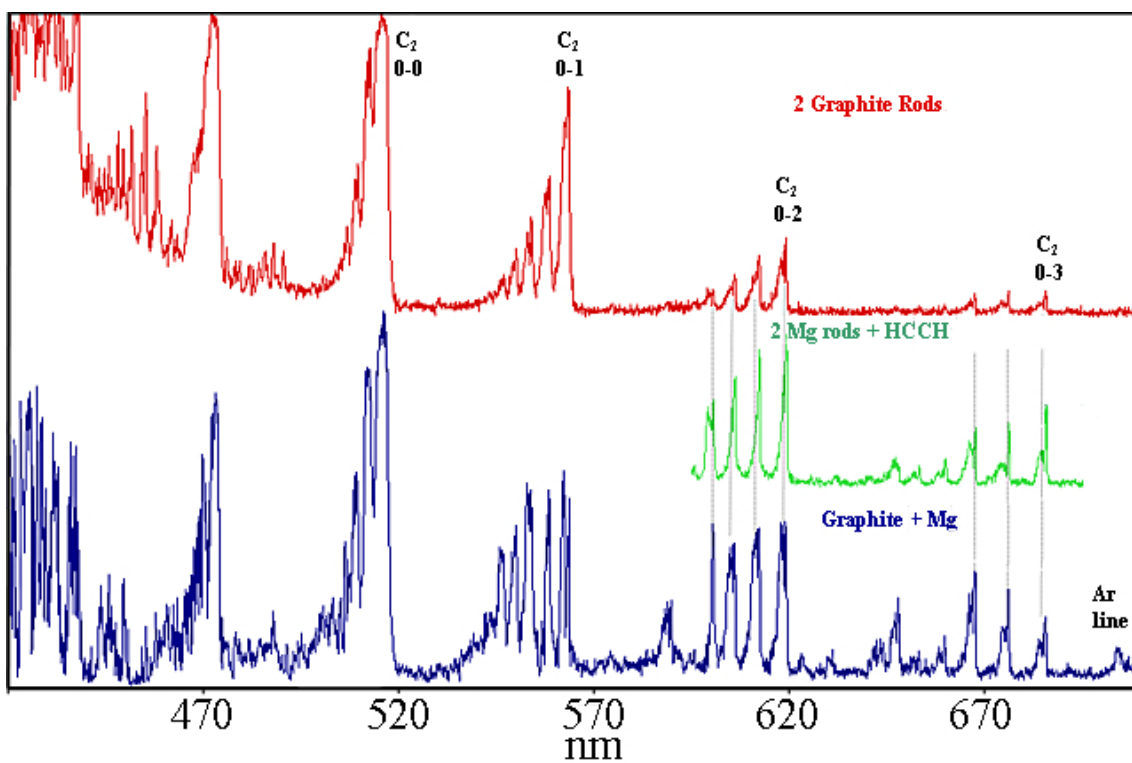


Figure 3.9: Low resolution spectra of magnesium carbon species produced by a double rod ablation source described in previous chapter.

# Chapter 4

## Vibrational analysis of the $\tilde{C} \ ^2B_2 \longleftarrow \tilde{X} \ ^2A_1$ electronic transition of $\text{AlC}_2$

### 4.1 Introduction

The rotational analysis of the 0-0  $\tilde{C} \ ^2B_2 \longleftarrow \tilde{X} \ ^2A_1$  transition of  $\text{AlC}_2$  was previously reported [68]. A further investigation of the gas-phase electronic spectrum of  $\text{AlC}_2$  in a broad spectral range involves both a mass-selective resonant two-color two-photon ionization (R2C2PI) technique [11] and laser induced fluorescence. The  $\tilde{C} \ ^2B_2 \longleftarrow \tilde{X} \ ^2A_1$  origin band was confirmed and new vibronic bands are investigated.

### 4.2 Theoretical calculation

The electronic ground state structures of  $\text{AlC}_2$  were investigated using both coupled cluster theory [85] and hybrid density B3LYP functional [86] using Dunning's correlation-consistent basis sets [87]. The calculations indicate that T-shaped  $\text{AlC}_2$  ( $C_{2v}$ ) is the global minimum. Linear  $\text{AlCC}$  ( $C_{\infty v}$ ) and  $\text{CAIC}$  ( $D_{\infty h}$ ) are local minima lying approximately 0.4 eV and 7 eV higher in energy respectively. QCISD(T) [88] also predicts that the ( $C_{2v}$ ) structure more stable than ( $C_{\infty v}$ ) by 36.72 kJ mol<sup>-1</sup> (0.38 eV) and the barrier

from ( $C_{\infty v}$ ) to ( $C_{2v}$ ) is predicted to be  $0.5 \text{ kJ mol}^{-1}$  ( $0.005 \text{ eV}$ ), at the same time the barrier from ( $C_{2v}$ ) to ( $C_{\infty v}$ ) is much higher  $37.22 \text{ kJ mol}^{-1}$  ( $0.385 \text{ eV}$ ). Equilibrium

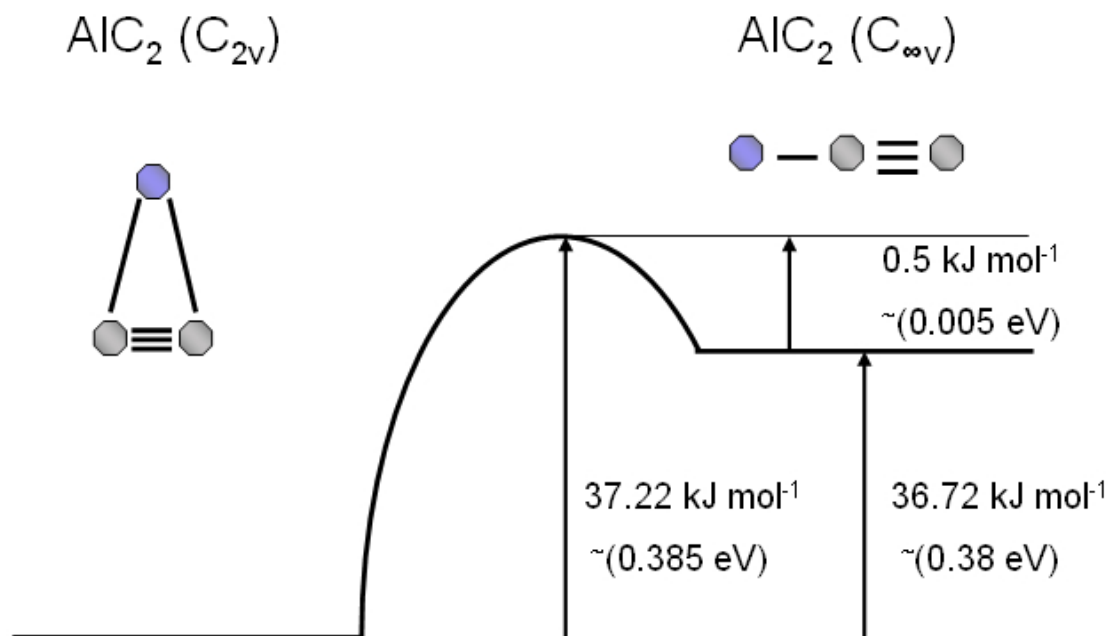


Figure 4.1: Structural calculation QCISD(T) predicts ( $C_{2v}$ ) structure more stable than ( $C_{\infty v}$ ) [88].

geometries for the ground state were optimized using the B3LYP/aug-cc-pVQZ theory and RCCSD(T)/cc-pVTZ approach. Previously, theoretical calculations [68] of excited electronic states of T-shaped  $\text{AlC}_2$  ( $C_{\infty v}$ ) were carried out using the complete active space self-consistent field method (CASSCF) [89] and multireference electronic configuration interaction (MRCI) theory [90]. Vertical excitation energies were calculated for states up to  $3.8 \text{ eV}$  above the ground state.

In order to predict the spectrum in the UV region, high lying electronic states for T-shaped  $\text{AlC}_2$  ( $C_{\infty v}$ ) have been investigated with CASSCF and MRCI approach using the Gaussian 98 suite of programs [91] and the MOLPRO package [92]. The resulting vertical transition energies and oscillator strengths are summarized in Table 4.1

T-shaped  $\text{AlC}_2$  possess the same  $C_{2v}$  symmetry like  $\text{H}_2\text{O}$ . Like water,  $\text{AlC}_2$  has 2  $a_1$  vibrations and 1  $b_2$  vibration. Accordingly, rovibronic transitions involving  $a_1$  vibronic

Isomer AlC <sub>2</sub> (C <sub>2v</sub> )	Transition	T <sub>v</sub> (eV)			f
		CAS	MRCI	MRCI+Q	CAS
	A <sup>2</sup> A <sub>1</sub> ← X <sup>2</sup> A <sub>1</sub>	1.185	1.272	1.493	2.83 x 10 <sup>-2</sup>
	B <sup>2</sup> B <sub>1</sub> ← X <sup>2</sup> A <sub>1</sub>	2.209	2.369	2.456	7.45 x 10 <sup>-4</sup>
	C <sup>2</sup> B <sub>2</sub> ← X <sup>2</sup> A <sub>1</sub>	2.764	2.832	2.730	1.49 x 10 <sup>-2</sup>
	D <sup>2</sup> B <sub>1</sub> ← X <sup>2</sup> A <sub>1</sub>	2.969	3.305	3.305	7.79 x 10 <sup>-3</sup>
	E <sup>2</sup> B <sub>2</sub> ← X <sup>2</sup> A <sub>1</sub>	3.590	3.887	3.830	1.48 x 10 <sup>-2</sup>
	F <sup>2</sup> A <sub>1</sub> ← X <sup>2</sup> A <sub>1</sub>	4.210			1.84 x 10 <sup>-3</sup>
	G <sup>2</sup> A <sub>2</sub> ← X <sup>2</sup> A <sub>1</sub>	4.696			0.0

Table 4.1: Calculated vertical transition energies(T<sub>v</sub>) and oscillator strengths (*f*) with CASSCF, MRCI and MRCI+Q theories with cc-pVTZ basis set for T-shaped AlC<sub>2</sub>.

modes will be fully allowed and will also be observed as b-type perpendicular transitions. Asymmetric b<sub>2</sub> vibrations, however, are only allowed in even quanta. This will also manifest themselves with perpendicular structure. In this way rigorous assignments can be made

### 4.3 Experimental

Jet cooled AlC<sub>2</sub> was produced using laser vaporization of an aluminum rod (30 mJ/5 ns pulse of a SH (532nm) Nd:YAG, focused to 0.3 mm) in the presence of a 1-1.5 % acetylene gas mixture seeded in either helium or argon expanded through a 0.3 mm orifice pulsed valve. The rod was rotated and translated so that a fresh surface was constantly exposed to the laser, which was fired in coincide with the gas flow over the target area. The ablation plume then flows through a channel (3 mm diameter 5 - 15 mm long) before entering vacuum. The resulting free jet expansion is probed using either a mass-selective resonant two-color two-photon ionization (R2C2PI) technique or laser induced fluorescence. Mass-selective spectra were collected by probing the skimmed beam of the jet expansion. Ions were removed from the collimated beam by applying a perpendicular electric field before entering the ionization zone of Wiley-McLaren time-of-flight mass spectrometer [93]. Neutral molecules were irradiated with a pulse of tunable ultraviolet-visible radiation, followed by 7.9 eV photons from F<sub>2</sub> excimer laser. Ions were then extracted into a time of flight tube where signal from a microchannel plate ion-detector was sent to fast os-

Label	$\nu(\text{cm}^{-1})$	$\Delta\nu(\text{cm}^{-1})$	Assignment
1	22108	0.0	$0_0^0$
2	22310	202	$2_0^1$
3	22495	387	$2_0^2$
4	22696	588	$2_0^3$
5	22902	794	$2_0^4$
6	23308	1200	$3_0^2$
7	23506	1398	$1_0^1$
8	23719	1611	$1_0^1 2_0^1$

Table 4.2: The vibrational bands position of  $C \ ^2B_2 \leftarrow X \ ^2A_1$  transition of  $\text{AlC}_2$ .

cilloscope and data acquisition card. The combination of UV-VIS and 157 photons was sufficient to ionize  $\text{AlC}_2$ .

Laser induced fluorescent spectra were measured using an excimer pumped dye laser ( $0.15 \text{ cm}^{-1}$ ). Fluorescence signal was collected by an  $f/1$  lens and detected using a photomultiplier tube and digital oscilloscope. Low resolution spectra were collected over the 355-500 nm range using an OPO (Ekspla) system ( $\Delta\nu_{\frac{1}{2}} \sim 5 \text{ cm}^{-1}$ ) with wavemeter calibration for vibronic survey scans. A pulsed dye laser was used ( $0.15 \text{ cm}^{-1}$ ,  $\sim 5 \text{ mJ/pulse}$ ) for the rotationally resolved work, with the calibration established through the use of an optogalvanic spectrum obtained from Fe/Ne hollow cathode lamp.

## 4.4 Results

The R2C2PI low resolution ( $5 \text{ cm}^{-1}$ ) electronic spectrum of the  $\tilde{C} \ ^2B_2 \leftarrow \tilde{X} \ ^2A_1$  band system in  $\text{AlC}_2$  for 410-475 nm range are shown in Figure 4.2. The wavelength of vibronic bands and suggested assignments are listed in Table[2]

Figure 4.3 contains the origin band of the  $\tilde{C} \ ^2B_2 \leftarrow \tilde{X} \ ^2A_1$  transition at 452 nm ( $22102.7 \text{ cm}^{-1}$ ), recorded using an excimer pumped dye laser and LIF detection accompanied by the simulation using Wang program. The perpendicular nature of the band is evident due to the rotational K-structure observed. Figure 4.4 contains the spectrum of two rovibronic transition (assigned as  $2_0^1$  and  $2_0^2$  vibronic bands) in comparison with the origin band at the top. The similar profile of all these bands indicate the



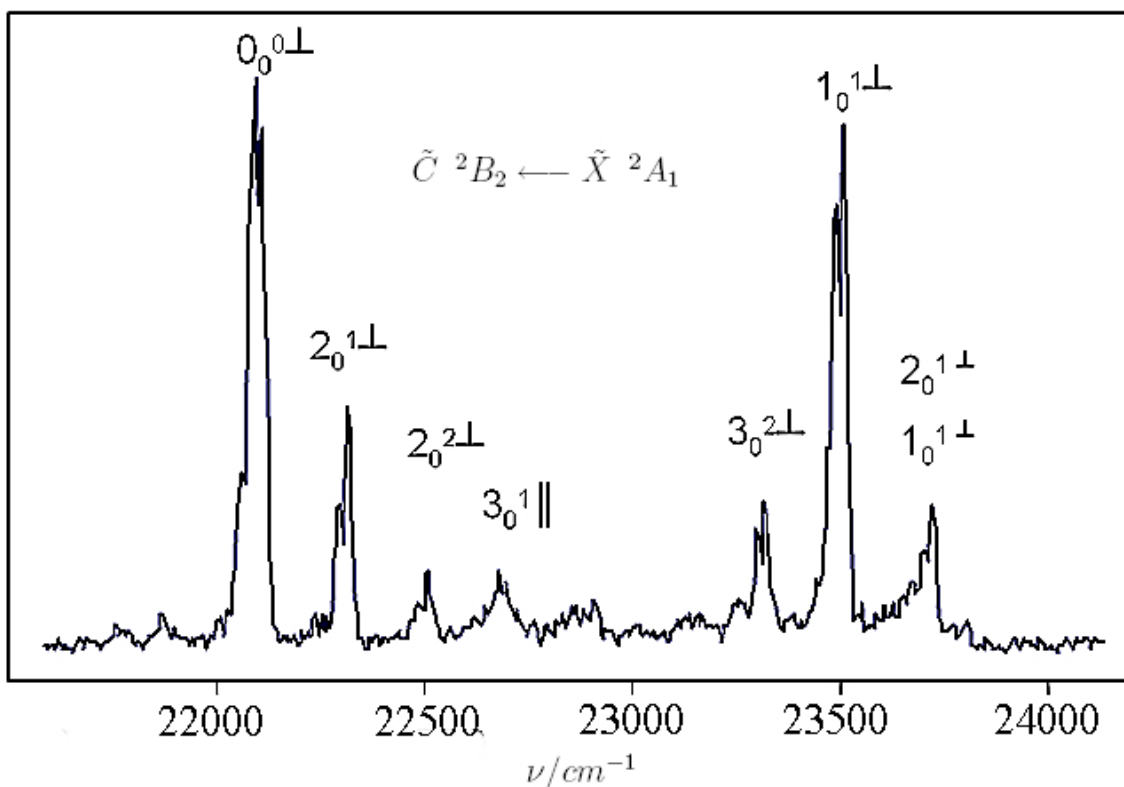


Figure 4.2: Low resolution R2C2PI electronic spectrum of the  $\tilde{C} \ ^2B_2 \leftarrow \tilde{X} \ ^2A_1$  band system in  $\text{AlC}_2$ .

perpendicular type transition. The  $2_0^2$  vibronic band, bottom trace, overlaps with the 0-0 and 1-1 bands of the  $B \ ^4\Sigma^- \leftarrow X \ ^4\Sigma^-$  AlC transition, and therefore the trace shown is actually the result of normalized spectral subtraction. The other three rovibronic transitions are presented in Figure 4.5. Once again, the evident K-structure denotes the perpendicular nature of the transition, and the structure is quite similar to the origin band.

In the low resolution scan, Figure 4.2 another band is observed around 440 nm ( $\sim 22700 \text{ cm}^{-1}$ ). The high resolution scan of this region, Figure 4.6, doesn't show any similarity to the transition of  $\text{AlC}_2$  observed before. If the  $\nu_2$  vibration progression were extrapolated into the investigated region, the  $2_0^3$  perpendicular vibrational band is expected to appear and it should be similar in structure to the bands observed in the Figures 4.4 and 4.5. Also if the  $23308 \text{ cm}^{-1}$  band is assigned to the allowed  $3_0^2$  perpendicular transi-

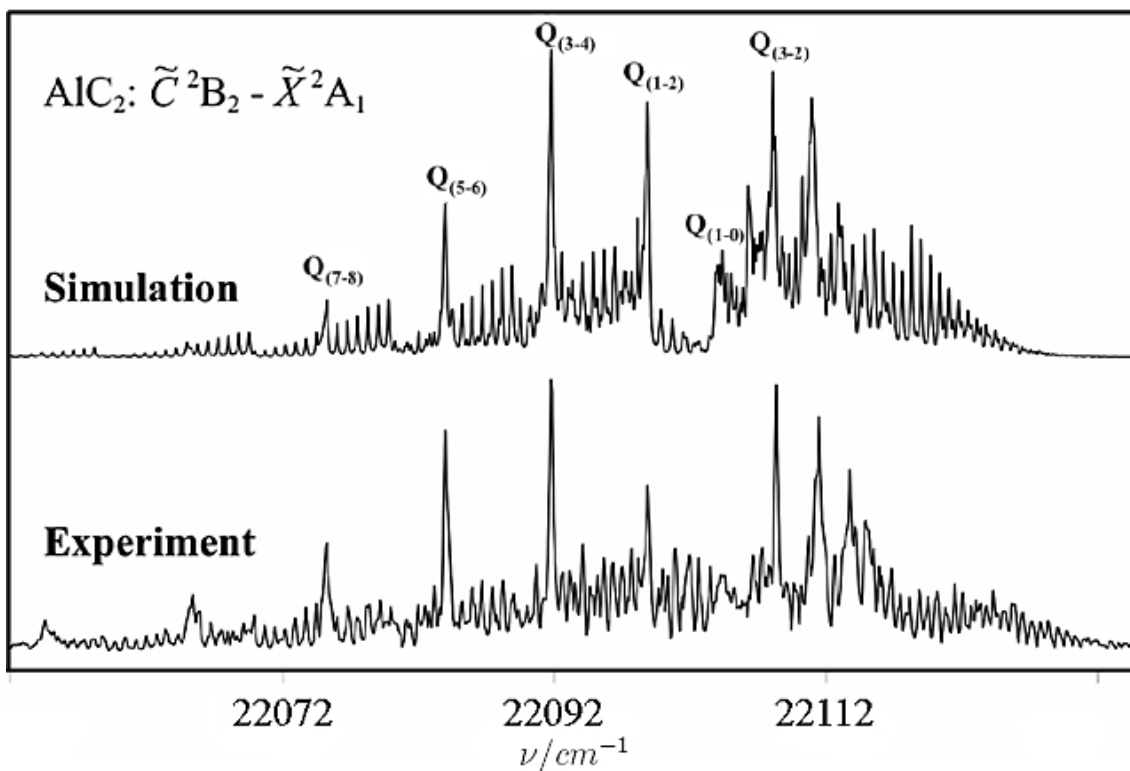


Figure 4.3: Rotationally resolved origin band of  $\text{AlC}_2$   $\tilde{C}^2B_2 \leftarrow \tilde{X}^2A_1$  transition observed by LIF and accompanied by the simulation using the Wang program.

tion, the forbidden  $3_0^1$  parallel transition may appear in the 440 nm ( $\sim 22700 \text{ cm}^{-1}$ ) area. It was suspected that the band observed around 440 nm is the overlapping of those two  $2_0^3$  and  $3_0^1$  bands. Comparison of the experimentally observed band with simulations of the  $2_0^3$  and  $3_0^1$  transitions (Figure 4.6) prove this assumption.

With the high resolution data available the vibrational bands positions, Table 8.2 can be corrected (Table 8.3). In the case of the  $\nu_2$  vibration, the transitions were observed up to  $2_0^4$ . The comparison with the harmonic oscillator model show that the energy levels become closely spaced with increasing number of quanta. The better approximation for the vibrational structure of the molecule than the quantum harmonic oscillator can be the Morse potential. The stationary states on the Morse potential have eigenvalues:

$$E(\nu) = h\nu_0\left(\nu + \frac{1}{2}\right) - \frac{[h\nu_0\left(\nu + \frac{1}{2}\right)]^2}{4D_e}$$

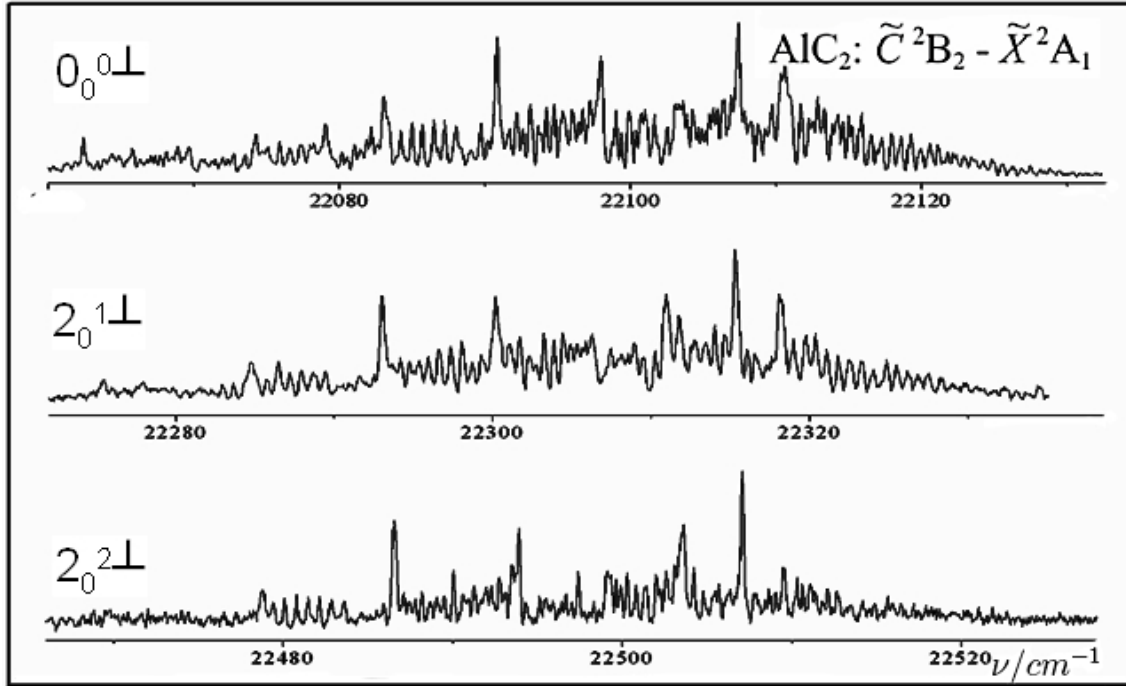


Figure 4.4: The rotationally resolved  $0_0^0$ ,  $2_0^1$  and  $2_0^2$  bands of  $\text{AlC}_2$   $\tilde{C}^2B_2 \leftarrow \tilde{X}^2A_1$  transition observed by LIF.

Where here  $\nu$  is the vibrational quantum number, and  $\nu_0$  has units of frequency, and is mathematically related to the particle mass,  $m$ , and the Morse constants via:

$$\nu_0 = \frac{a}{2\pi} \sqrt{\frac{2D_e}{m}}.$$

It can be written in the more common form:

$$\frac{E_\nu}{hc} = \omega_e \left( \nu + \frac{1}{2} \right) - \omega_e \chi_e \left( \nu + \frac{1}{2} \right)^2$$

The approximation of  $\nu_2$  vibronic bands progression with this polynomial gives the coefficients:

$$\omega_e = 223.78 \text{ and } \omega_e \chi_e = 8.07 \text{ cm}^{-1}$$

The dissociation energy for the  $\nu_2$  vibration is  $D_e = 4.8 \cdot 10^{-8}$  J. For the  $\nu_3$  vibration

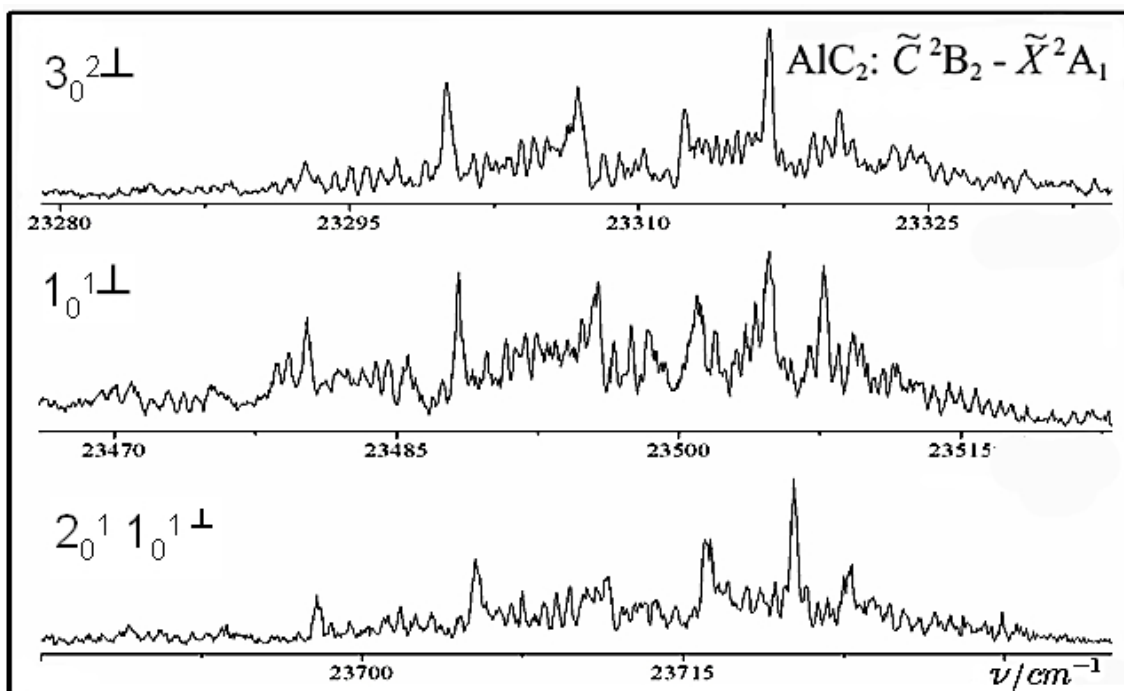


Figure 4.5: The rotationally resolved  $3_0^2$ ,  $1_0^1$  and  $1_0^1 2_0^1$  bands of  $\text{AlC}_2 \tilde{C}^2B_2 \leftarrow \tilde{X}^2A_1$  transition observed by LIF.

only two vibronic bands were observed and only one for  $\nu_1$ .

## 4.5 Conclusion

The result of the spectroscopic investigation of the jet-cooled  $\text{AlC}_2 \tilde{C}^2B_2 \leftarrow \tilde{X}^2A_1$  band system can be summarized as follows. The rotationally resolved spectra were obtained and analyzed for several vibronic bands. The high resolution scans allowed the identification of the band observed in the 440 nm region as an overlap of the  $2_0^3$  perpendicular and  $3_0^1$  parallel transitions. Also, the positions of vibronic bands were corrected and reported in Table 8.3. The  $\nu_2$  vibration progression was approximated with a Morse potential and the coefficient of unharmonicity and dissociation energy were obtained. The presence of the  $3_0^1$  forbidden band in spectra can be explained by perturbation with the  $2_0^3$  allowed transition.

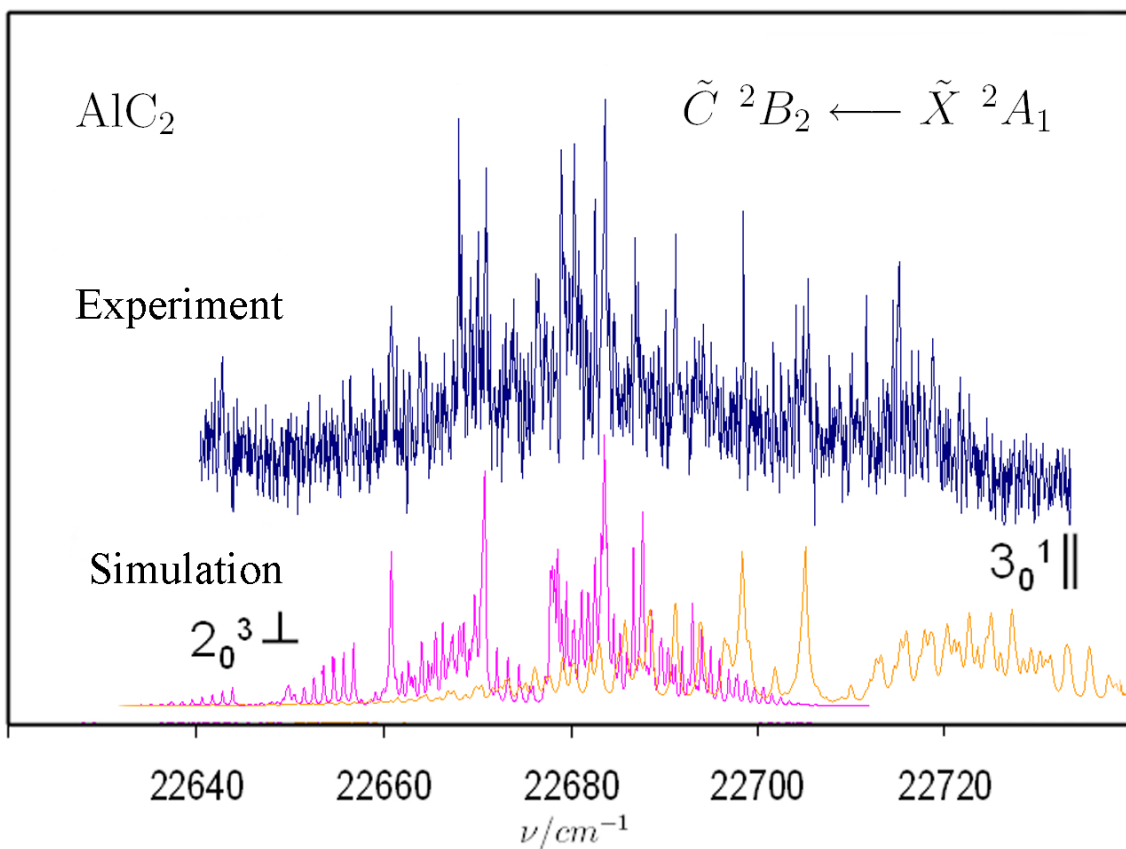


Figure 4.6: The comparison of experimentally observed observed by LIF band around 440 nm with simulated  $2_0^3$  and  $3_0^1$  bands of  $\text{AlC}_2 \tilde{C} \ ^2B_2 \leftarrow \tilde{X} \ ^2A_1$  transition .

Label	$\nu(\text{cm}^{-1})$	$\Delta\nu(\text{cm}^{-1})$	Assignment
1	22102.7	0.0	$0_0^0$
2	22310	207.3	$2_0^1$
3	22502	399.3	$2_0^2$
4	22677	574.3	$2_0^3$
5	22705	602.3	$3_0^1$
6	22836.3	733.6	$2_0^4$
7	23312	1209.3	$3_0^2$
8	23499.7	1397	$1_0^1$
9	23715	1612.3	$1_0^1 2_0^1$

Table 4.3: The corrected vibrational bands position of  $C \ ^2B_2 \leftarrow X \ ^2A_1$  transition of  $\text{AlC}_2$ .

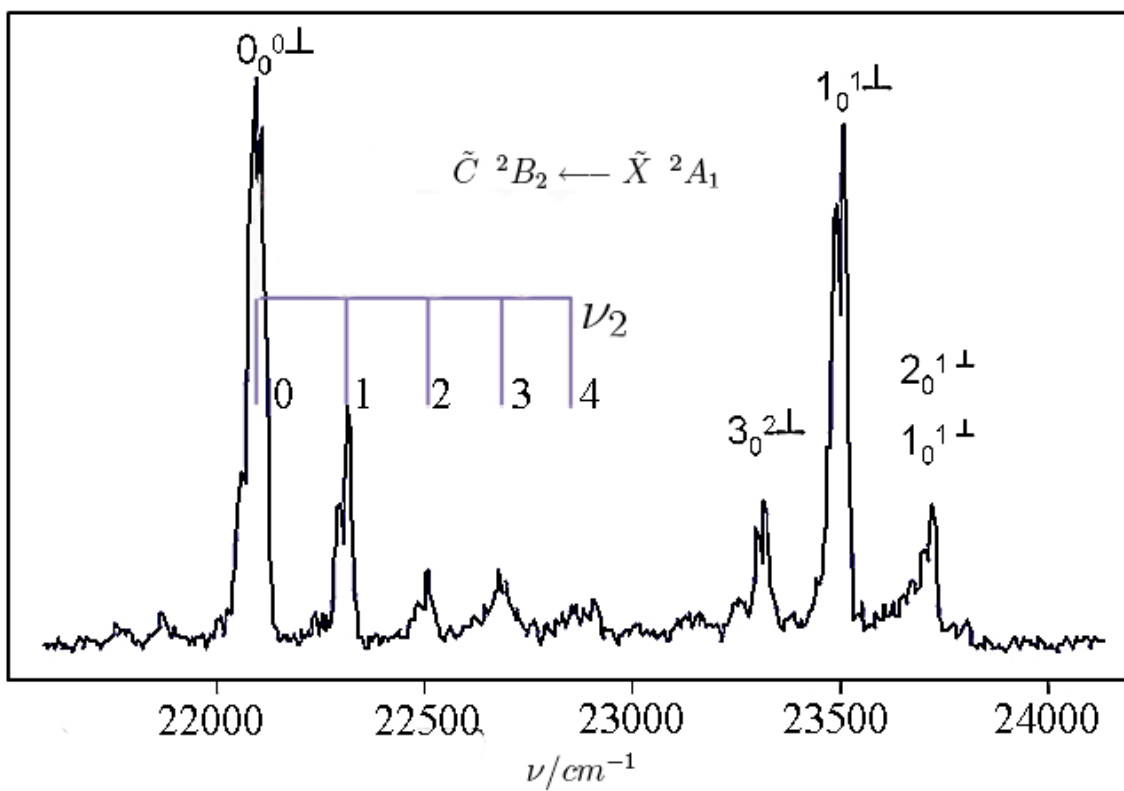


Figure 4.7: The  $\nu_2$  vibrational progression of AlC<sub>2</sub>  $\tilde{C} \ ^2B_2 \leftarrow \tilde{X} \ ^2A_1$  transition.

# Chapter 5

## The further investigation of the vibronic spectrum observed in $A \ ^1\Pi \leftarrow X \ ^1\Sigma^+$ electronic transition AlCCH

### 5.1 Introduction

Aluminum is one of the most abundant metals in the interstellar medium. Several aluminum containing compounds were already found in space, including AlNC and AlCl, which were observed in pure rotational spectra of IRC +10216 carbon star [94]. Other aluminum compounds, like aluminum terminated carbon chains are expected to be found in space. To better understand the bonding processes found in the interstellar medium that are responsible for the bonding of metals containing molecules, the species must first be studied extensively from a spectroscopic point of view. Previously, the  $A \ ^1\Pi \leftarrow X \ ^1\Sigma^+$  electronic transition of linear AlCCH was detected by using laser ablation and (R2C2PI) in 315-355 nm region.

Frequency	AICCH ( $C_{\infty v}$ )	HAICC ( $C_{2v}$ )
$\nu_1$	3438 ( $\sigma$ )	2028 ( $a_1$ )
$\nu_2$	2065 ( $\sigma$ )	1807 ( $a_1$ )
$\nu_3$	733 ( $\pi$ )	754 ( $a_1$ )
$\nu_4$	503 ( $\sigma$ )	7522 ( $b_2$ )
$\nu_5$	132 ( $\pi$ )	459 ( $b_1$ )
$\nu_5$		415 ( $b_2$ )

Table 5.1: Ab initio calculated harmonic vibrational frequencies ( $\text{cm}_1$ ) for linear and cyclic isomers in their ground states at the DFT-B3LYP/ aug-cc-pvtz level [95].

## 5.2 Theoretical calculation

The ground state geometry has been calculated for 4 different isomers [95]:

linear-AICCH, cyclic-HAICC, linear-HAICC and bend AICCH. Geometry optimization was performed with the GAUSSIAN 98 suite of programs [91] using DFT and B3LYP/aug-cc-pvtz basis set. It was shown that the linear-AICCH configuration is more stable than the cyclic by  $41.1 \text{ kJ mol}^{-1}$ . The geometry optimization for other isomers linear-HAICC and bent AICCH indicate that they are unstable and with time they will convert to cyclic-HAICC and linear-AICCH, respectively. The calculated harmonic vibrational frequencies for the ground state stable isomers are listed in Table 8.1.

The previously observed spectrum in the 315-350 nm region was assigned to  $A \ ^1\Pi \leftarrow X \ ^1\Sigma^+$  electronic transition of linear AICCH. The observed vibronic bands are listed in Table 8.2. According to their assignment in the degenerate  $A \ ^1\Pi$  state, the  $\nu_5'$  bending vibrational mode (AICC) of  $\Pi$  symmetry splits in to two components due to the Renner-Teller interaction. In order to improve the assignment of the vibrational structure of the  $A \ ^1\Pi \leftarrow X \ ^1\Sigma^+$  transition in AICCH, LIF spectra were obtained.

## 5.3 Experiment.

Jet cooled AICCH was produced using laser vaporization of an aluminum rod (20 mJ/5 ns pulse of a SH (532nm) Nd:YAG, focused to 0.3 mm) in the presence of a 1-1.5 % acetylene gas mixture seeded in either helium or argon provided by a 0.3 mm orifice pulsed valve. The rod was rotated and translated so that the fresh surface was constantly exposed to



Label [95]	$\nu/\text{cm}^{-1}$		$\Delta\nu/\text{cm}^{-1}$		Assignment
	AICCH	AICCD	AICCH	AICCD	
2'	28233.3	28293.3	-516.4	-513.6	$4_1^0$ (AIC stretch)
1'	28624.8	28577.1	-126.0	-229.7	Hot band
1	28749.7	28806.9	0	0	$0_0^0$ ( $A \ ^1\Pi \leftarrow X \ ^1\Sigma^+$ )
2	28784.1	28843.3	34.4	36.4	$\nu_5'$ (AICC bend)
3	28864.3	28921.9	114.5	115	$\nu_5'$ (AICC bend)
4	29149.6	29103.7	399.9	296.9	$\nu_3'$ (CCH bend)
5	29404.2	29435.4	654.5	628.5	$4_0^1$ (AIC stretch)
6	29427.0	29468.1	677.3	661.2	(AICC bend)
7	29505.7	29563.3	756.0	756.5	(AICC bend)
8	29623.8	29635.9	874.0	829.1	(AICC bend)
9	29721.5	29740.1	971.8	933.2	(AICC bend)
10	29857.3	29921.7	1107.6	1114.8	(AICC bend)
11	30051.2	30081.0	1301.5	1274.1	$4_0^2$ (AIC stretch)
12	30310.8	30332.9	1561.1	1526.0	
13	30485.5	30491.1	1735.8	1684.2	
14	30640.0		1890.0		

Table 5.2: The vibronic bands in the  $A \ ^1\Pi \leftarrow X \ ^1\Sigma^+$  system of AICCH and AICCD observed by R2C2PI [95].

the laser, which was fired in coincide with the gas flow over the target area. The ablation plume then flows through a channel (2 mm diameter 5 mm long) before entering vacuum. The resulting free jet expansion is probed by LIF  $\sim 40$  mm down stream. Fluorescence signal was collected by an  $f/1$  lens and detected using a photomultiplier tube and digital oscilloscope. The frequency doubled radiation from a Jaguar pulsed dye laser with  $\Delta\nu \sim 0.06 \text{ cm}^{-1}$  was used. The predoubled laser beam was used for calibration with Burleigh WA-4500 pulsed wavemeter.

## 5.4 Results.

High resolution spectra were collected in the region of 27800-29600  $\text{cm}^{-1}$ (Figure 5.1). As was mentioned before, the LIF experiment does not have mass selection, and thus assignment of the vibronic bands were made based on their rotational profiles and spacings.

The band heads assigned to AICCH and AICCD  $A \ ^1\Pi \leftarrow X \ ^1\Sigma^+$  are presented in

Figure 5.2 and listed in Table 8.3.

AICCH				AICCD			
N	$\nu/\text{cm}^{-1}$	$\Delta\nu/\text{cm}^{-1}$	I	N*	$\nu/\text{cm}^{-1}$	$\Delta\nu/\text{cm}^{-1}$	I
1	29468.5	715.0	0.20	1*	29469.7	659.7	0.08
2	29425.8	672.3	0.59	2*	29440.7	630.7	0.45
3	29398.3	644.8	0.95	3*	29435.2	625.2	0.17
4	29374.8	621.3	0.40	4*	29431.9	621.9	0.09
5	29361.9	608.4	0.17	5*	29417.5	607.5	0.10
6	29343.6	590.1	0.32	6*	29398.3	588.3	0.11
7	29296.5	543.0	0.11	7*	29298.4	488.3	0.10
8	29276.9	523.4	0.11	8*	29273.5	463.5	0.28
9	29240.4	486.9	0.31	9*	29272.3	462.3	0.14
10	29144.3	390.8	0.86	10*	29271.4	461.4	0.14
11	29125.4	371.9	0.56	11*	29191.1	381.1	0.12
12	29118.5	365.0	0.19	12*	29144.1	334.1	0.33
13	29110.8	357.3	0.24	13*	29140.2	330.2	0.21
14	29103.4	349.9	0.20	14*	29138.2	328.2	0.22
15	29094.1	340.6	0.12	15*	29135.8	325.8	0.22
16	29086.5	332.9	0.08	16*	29131.9	321.9	0.21
17	29042.5	289.0	0.19	17*	29129.2	319.1	0.34
18	29033.8	280.2	0.15	18*	29126.6	316.6	0.22
19	29029.7	276.2	0.17	19*	29125.6	315.6	0.15
20	29027.0	273.5	0.16	20*	29110.5	300.5	0.38
21	29024.6	271.1	0.17	21*	29098.0	288.0	0.84
22	29022.3	268.8	0.17	22*	29095.4	285.4	0.11
23	28975.0	221.5	0.37	23*	29041.3	231.3	0.69
24	28937.6	184.1	0.24	24*	29014.7	204.7	0.32
25	28915.2	161.7	0.21	25*	29000.4	190.4	0.12
26	28909.8	156.3	0.20	26*	28989.5	179.4	0.12
27	28905.2	151.6	0.23	27*	28934.1	124.1	0.23
28	28855.8	102.2	0.59	28*	28921.7	111.7	0.49
29	28854.4	100.9	0.46	29*	28915.4	105.3	0.29
30	28781.0	27.5	0.76	30*	28909.7	99.6	0.33
31	28753.5	0	0.99	31*	28879.6	69.6	0.21
32	28709.4	-44.1	0.16	32*	28867.6	57.6	0.14
33	28680.9	-72.6	0.20	33*	28838.9	28.9	0.49
34	28620.7	-132.9	0.35	34*	28810.0	0	0.91
35	28497.1	-256.4	0.15	35*	28753.5	-56.5	0.46
36	28479.8	-273.7	0.11	36*	28726.6	-83.4	0.36
37	28444.0	-309.6	0.11	37*	28713.5	-96.5	0.16
38	28346.7	-406.8	0.28	38*	28703.7	-106.4	0.13
39	28324.8	-428.7	0.28	39*	28689.0	-121.0	0.08

AlCCH				AlCCD			
N	$\nu/\text{cm}^{-1}$	$\Delta\nu/\text{cm}^{-1}$	I	N*	$\nu/\text{cm}^{-1}$	$\Delta\nu/\text{cm}^{-1}$	I
40	28316.8	-436.7	0.16	40*	28681.3	-128.8	0.06
41	28305.4	-448.1	0.06	41*	28668.3	-141.8	0.06
42	28293.3	-460.3	0.04	42*	28657.7	-152.3	0.04
43	28250.1	-503.4	0.37	43*	28632.9	-177.2	0.10
44	28230.0	-523.0	0.68	44*	28582.0	-228.0	0.46
45	28108.9	-644.6	0.43	45*	28581.5	-228.4	0.42
46	27710.4	-1043.1	0.10	46*	28525.6	-284.4	0.37
47	27586.1	-1167.4	0.10	47*	28499.6	-310.4	0.35
48	27575.1	-1178.4	0.04	48*	28495.0	-315.0	0.22
49	27564.7	-1188.9	0.03	49*	28491.8	-318.2	0.25
50				50*	28480.1	-329.0	0.12
51				51*	28473.6	-336.4	0.10
52				52*	28469.2	-340.8	0.15
53				53*	28457.4	-352.6	0.21
54				54*	28451.1	-358.9	0.16
55				55*	28315.9	-494.1	0.30
56				56*	28294.4	-515.5	0.61
57				57*	28291.7	-518.4	0.49
58				58*	28070.8	-739.2	0.12
59				59*	27783.3	-1026.7	0.18
60				60*	27779.6	-1030.4	0.13
61				61*	27777.6	-1032.4	0.18

Table 5.3: The vibronic bands assigned to the  $A\ ^1\Pi \leftarrow X\ ^1\Sigma^+$  electronic transition of AlCCH and AlCCD observed by LIF.(N and N\* is nothing but number in table.)

## 5.5 Discussion

Degenerate electronic states usually occur in molecules having a high degree of symmetry. In degenerate electronic states of linear triatomic or polyatomic molecules the potential function along the bending coordinate can split due to vibronic coupling between the motions of the electrons and the nuclear vibrations. The resulting breakdown of the Born-Oppenheimer approximation in this case is known as the Renner-Teller effect [78].

In the case of AlCCH there are two bending vibration  $\nu_3$  (CCH) and  $\nu_5$  (AlCC) which can combine in an infinite numbers of ways of bending to reduce the symmetry and cause the Renner-Teller effect. This results in an overall lowering in energy for the molecule

Due to the expansional cooling only low vibrational levels in the ground state are expected to be populated during the experiment. For  $^1\Pi \leftarrow ^1\Sigma^+$  transition, the dis-

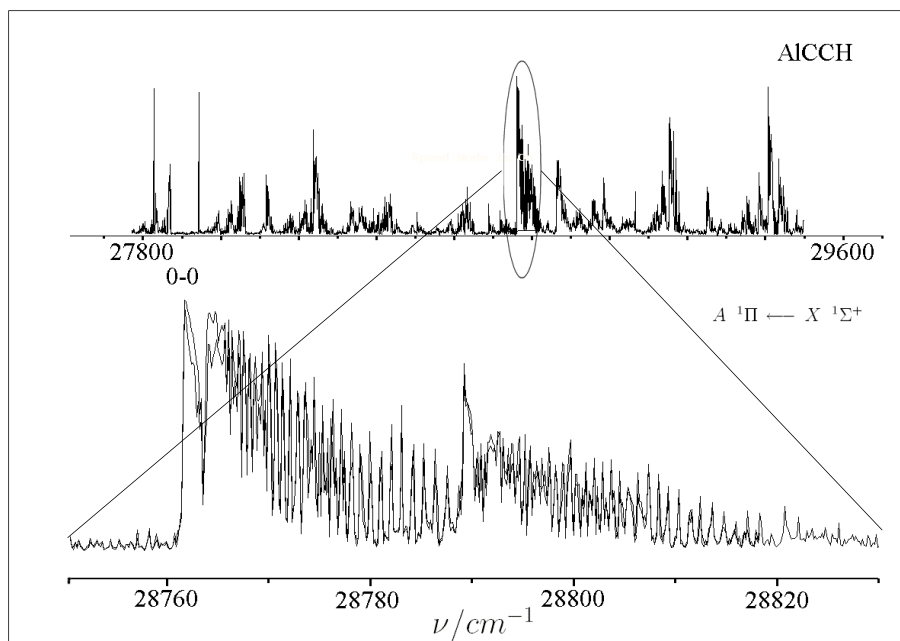


Figure 5.1: High resolution spectrum of the  $A \ ^1\Pi \leftarrow X \ ^1\Sigma^+$  transition of AlCCH.

inction between "Hund" case (a) and (b) is pointless. The selection rules are:

$\Delta J = 0; \pm 1, \Delta \Lambda = 0; \pm 1, \Sigma^+ \leftrightarrow \Sigma^+, \Sigma^- \leftrightarrow \Sigma^-, \Sigma^+ \leftrightarrow \Sigma^-, \Sigma \leftrightarrow \Pi, \Pi \leftrightarrow \Delta, \Sigma \leftrightarrow \Delta, \Sigma \leftrightarrow \Phi$  and  $\Pi \leftrightarrow \Phi$ .

The scheme of the energy levels and possible transitions presented in Figure 5.3. It is expected to observe Renner-Teller splitting originated from the first excited vibrational level in the ground electronic state.

The vibrational assignment is presented in Figure 5.1. The corrected band positions are listed in Table 5.4

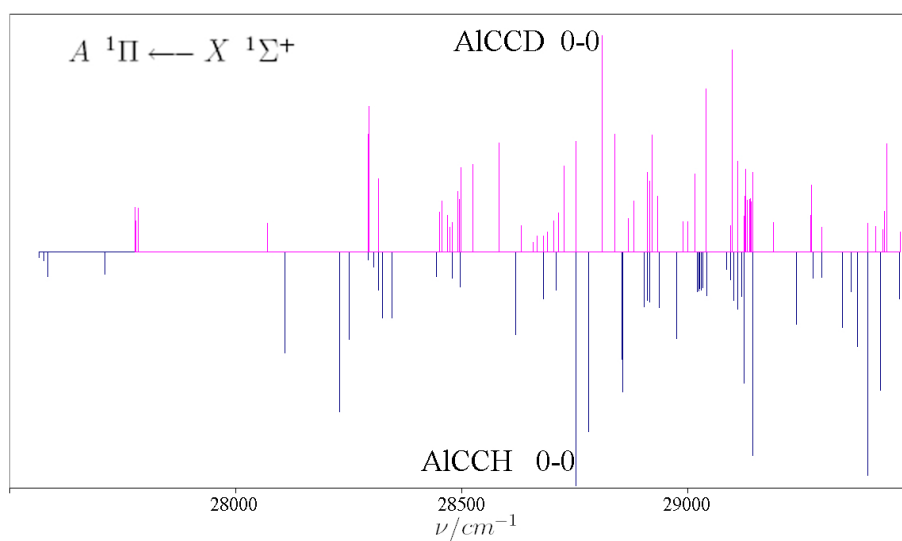


Figure 5.2: The band heads assigned to  $A \ ^1\Pi \leftarrow X \ ^1\Sigma^+$  transition of AICCH and AICCD.

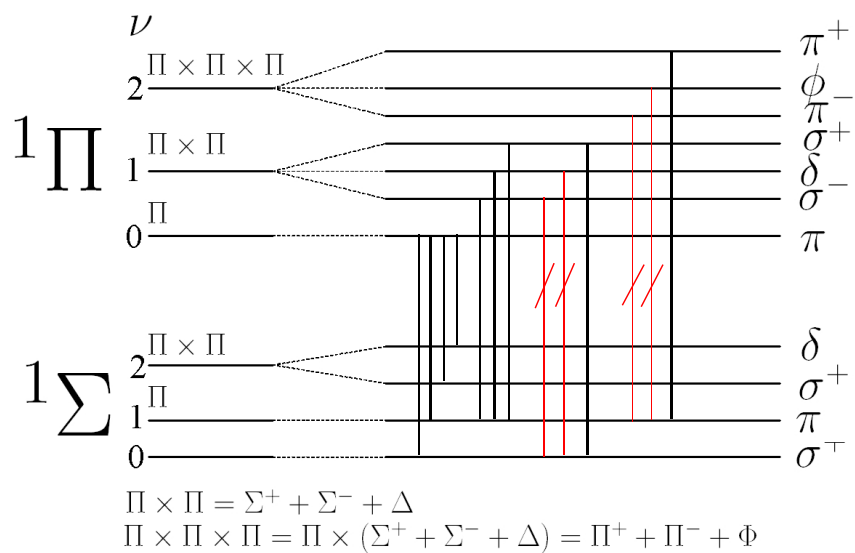


Figure 5.3: Scheme of energy levels for  $^1\Pi \leftarrow ^1\Sigma^+$  system and allowed transitions in case of a Renner-Teller effect.

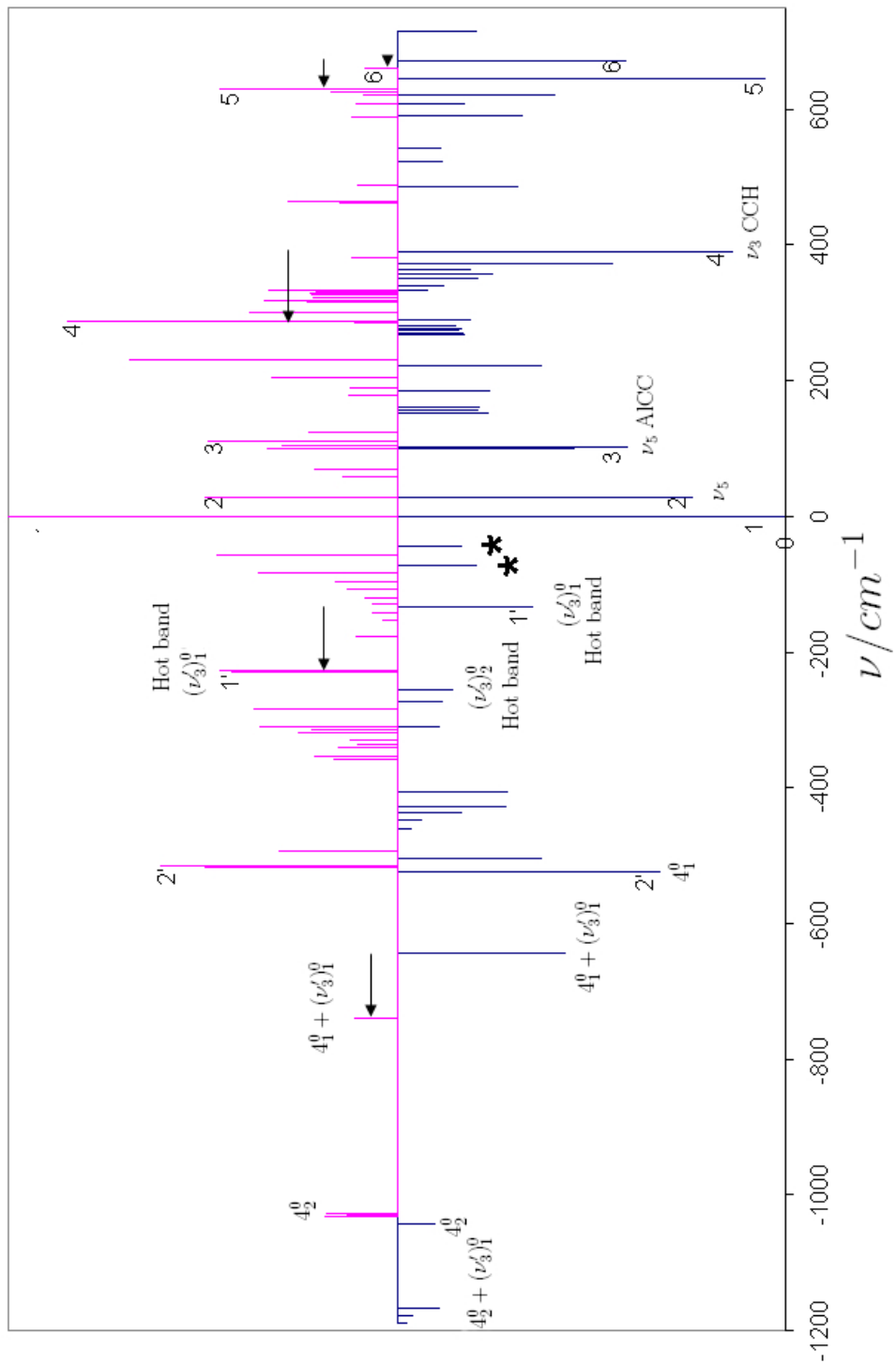


Figure 5.4: The vibrational assignment of AICCH and AICCD  $A \ ^1\Pi \leftarrow X \ ^1\Sigma^+$  band system. Arrows mark the transition shifted due to deturation.

Label	$\nu/\text{cm}^{-1}$				$\Delta\nu/\text{cm}^{-1}$		Assignment
	N	AlCCH	N*	AlCCD	AlCCH	AlCCD	
	47	27586.1			-1167.4		$4_2^0 + (\nu'_3)_1^0$
	46	27710.4	60*	27779.6	27710.4	-1030.4	$4_2^0$ (AlC stretch)
	45	28108.9	58*	28070.8	-644.6	-739.2	$4_1^0 + (\nu'_3)_1^0$
2'	44	28230.0	56*	28294.4	-523.0	-515.5	$4_1^0$ (AlC stretch)
	35	28497.1			-256.4		$(\nu'_3)_2^0$ Hot band
1'	34	28620.7	44*	28582.0	-132.9	-228.0	$(\nu'_3)_1^0$ Hot band
	33	28680.9			-72.6		Renner-Teller component of $\nu_5$
	32	28709.4			-44.1		Renner-Teller component of $\nu_5$
1	31	28753.5	34*	28810.0	0	0	$0_0^0$ ( $A \ ^1\Pi \leftarrow X \ ^1\Sigma^+$ )
2	30	28781.0	33*	28838.9	27.5	28.9	$\nu'_5$ (AlCC bend)
3	28	28855.8	28*	28921.9	102.2	111.7	$\nu'_5$ (AlCC bend)
4	10	29144.3	21*	29103.7	390.8	288.0	$\nu'_3$ (CCH bend)
5	3	29398.3	2*	29440.7	644.8	630.7	$4_0^1$ (AlC stretch)
6	2	29425.8	1*	29469.7	672.3	659.7	(AlCC bend)

Table 5.4: The vibronic bands in the  $A \ ^1\Pi \leftarrow X \ ^1\Sigma^+$  system of AlCCH and AlCCD observed by LIF.

The bands marked with  $\star$  are due to Renner-Teller splitting of AlCCH originated from the first vibrationally excited state in the electronic ground level. It is expected to see the third component, however in the experiment only two components appear. It is possible that the third component is too weak to be detected with the existing experimental setup. The other possibility is that the third component overlaps with the origin band.

The bands assigned with  $\nu_3$  vibrations and combinations are still questionable due to disagreement with the predicted frequency for CCH bending mode. The frequency of which was predicted to be  $754 \text{ cm}^{-1}$  and observed significantly lower in energy  $132.9 \text{ cm}^{-1}$

## 5.6 Conclusion.

High resolution scans of  $A \ ^1\Pi \leftarrow X \ ^1\Sigma^+$  band system reveal 41 new vibronic band for AlCCH and 53 vibronic band for AlCCD. The obtained rotational structure is too complicated to be analyzed as it is. It is possible that the key to understand this structure can be obtained using a state-selected experiment such as the four-wave mixing technique.



## Chapter 6

# Electronic spectrum of the $\text{AlC}_2$ radical

## Electronic Spectrum of the AlC<sub>2</sub> Radical

Egor Chasovskikh, Evan B. Jochowitz, Eunsook Kim, and John P. Maier\*

Department of Chemistry, University of Basel, Klingelbergstrasse 80, CH-4056 Basel, Switzerland

Isabelle Navizet

Université Paris-Est, Laboratoire de Chimie Théorique, 5 bd Descartes,  
F-77454 Marne la Vallée cedex 2, France

Received: July 3, 2007; In Final Form: September 5, 2007

An electronic transition of the AlC<sub>2</sub> radical (*C*<sub>2v</sub> structure) has been observed using laser-induced fluorescence spectroscopy. The molecule was prepared in a supersonic expansion by ablation of an aluminum rod in the presence of acetylene gas. A spectrum was recorded in the 451–453 nm region and assigned to the  $\tilde{C}^2B_2-\tilde{X}^2A_1$  system ( $T_0 = 22102.7 \text{ cm}^{-1}$ ) based on a rotational analysis and agreement with calculated molecular parameters and excitation energies. Ab initio results obtained using couple cluster methods are in accord with previous theoretical work which concludes that ground-state AlC<sub>2</sub> possesses a T-shaped *C*<sub>2v</sub>  $^2A_1$  geometry, with the linear  $^2\Sigma^+$  AlCC isomer 0.70 eV higher in energy. A fit of the experimental spectrum yields rotational constants in the ground and electronically excited states that are in reasonable agreement with the calculated values:  $A'' = 1.7093(107)$ ,  $B'' = 0.4052(50)$ ,  $C'' = 0.3228(49) \text{ cm}^{-1}$  for the  $\tilde{X}^2A_1$  state, and  $A' = 1.5621(137)$ ,  $B' = 0.4028(46)$ ,  $C' = 0.3201(54) \text{ cm}^{-1}$  for  $\tilde{C}^2B_2$ . Variation in individual fluorescence lifetimes suggests that the emitting  $\tilde{C}^2B_2$  state undergoes rovibronic mixing with lower lying electronic states.

### Introduction

Metal carbides play an important role in the field of catalytic reactions, mainly due to the large surface areas that they tend to possess. Other recent advances in coating technologies have further fueled research in these compounds. Interest in gas-phase studies stems from the fact that smaller metal carbides are predicted to exist in space. While carbon is the most abundant heavy element in interstellar space, aluminum compounds containing halides, such as AlCl and AlF, as well as AlNC, have been detected in the inner circumstellar envelopes of carbon-rich stars through their rotational transitions.<sup>1,2</sup>

Dicarbides became a curiosity when both experiments and theory demonstrated that SiC<sub>2</sub> possesses a T-shaped geometry,<sup>3,4</sup> which was in direct conflict with the linear ground state structure of C<sub>3</sub>.<sup>5,6</sup> Among theorists, there is general agreement that AlC<sub>2</sub> also has a T-shaped structure, with the *C*<sub>2v</sub> conformation 33.5–46 kJ mol<sup>-1</sup> more stable than the linear *C*<sub>∞v</sub> geometry.<sup>7–11</sup> The high electron affinity of C<sub>2</sub> also suggests that stable dicarbides are likely formed with electropositive metals possessing low-ionization potentials, such as Al, Mg, or B.<sup>12</sup> Similarly, vibrational, rotational, and hyperfine structure in high-resolution spectra for the  $\tilde{A}^2A_1 - \tilde{X}^2A_1$  transition of T-shaped YC<sub>2</sub> have also been analyzed.<sup>13,14</sup> Optical Stark measurements on the origin band led to the determination of a large dipole moment (6.38 D in the  $\tilde{X}^2A_1$  state) confirming that the bonding in YC<sub>2</sub> is highly ionic.<sup>15</sup> Any structural parameters obtained from studying AlC<sub>2</sub> will help expand the understanding of more complex metal carbide systems. Spectroscopically determined constants offer a means to identify these molecules in interstellar environments.

Recent structural calculations found that the *C*<sub>2v</sub> T-shaped structure is more stable than the linear *C*<sub>∞v</sub> geometry by 47.66

kJ mol<sup>-1</sup> using a single point QCISD(T) calculation (36.69 kJ mol<sup>-1</sup> using DFT B3LYP).<sup>10</sup> The same study reports a 37.20 kJ mol<sup>-1</sup> barrier (B3LYP) for isomerization from the T-shape to linear form, versus a 0.50 kJ mol<sup>-1</sup> barrier for the reverse reaction, thus indicating that any linear *C*<sub>∞v</sub> AlC<sub>2</sub> will be easily converted into the *C*<sub>2v</sub> isomer.

Previous experimental work on the AlC<sub>2</sub> radical includes electron spin resonance studies in rare gas matrices.<sup>16</sup> Here, the T-shaped structure of AlC<sub>2</sub> was confirmed and led to the assignment of the  $\tilde{X}^2A_1$  ground state. Bonding characteristics were also analyzed, indicating that the aluminum atom interacts with C<sub>2</sub> by donating electron density to the more electronegative C<sub>2</sub> through both  $\sigma$ - and  $\pi$ -molecular orbitals.

Although AlC<sub>2</sub> has not yet been detected in the IR, theoretical methods have been used to calculate vibrational frequencies in the ground state: a single point QCISD optimization yielded the low-frequency b<sub>2</sub> mode (404.8 cm<sup>-1</sup>) and the two a<sub>1</sub> vibrational modes (624.4 and 1761 cm<sup>-1</sup>).<sup>10</sup> CASSCF theory with a VDZ basis set reports frequencies of 442, 680.2, and 1733.1 cm<sup>-1</sup> for the same vibrations.<sup>8</sup>

The energy difference between the  $\tilde{X}^2A_1$  and  $\tilde{A}^2A_1$  states in neutral AlC<sub>2</sub> was determined as 0.98 eV through an analysis of the photoelectron spectrum of the AlC<sub>2</sub><sup>-</sup> anion.<sup>17</sup> A vibrational progression was assigned to a 590 cm<sup>-1</sup> Al–C<sub>2</sub> stretch in both the ground and excited  $^2A_1$  states.

Rotational constants for the equilibrium structures of the T-shaped AlC<sub>2</sub> radical were calculated as:  $A_e = 50.76$ ,  $B_e = 12.00$ , and  $C_e = 9.705 \text{ GHz}$ .<sup>7</sup> A more recent study, using a B3LYP/6-311G(d) method, reports  $A_e = 52.657$ ,  $B_e = 11.814$ , and  $C_e = 9.650 \text{ GHz}$  for a similar T-shaped structure.<sup>11</sup>

### Experimental Section

Jet-cooled AlC<sub>2</sub> was produced using laser vaporization (532 nm) of a pure aluminum rod in the flow of 5% acetylene in

\* Corresponding author. E-mail: j.p.maier@unibas.ch. Phone: +41 61 267 38 26. Fax: +41 61 267 38 55.

**TABLE 1: Optimized Geometry for  $\tilde{X}^2A_1$  ( $C_{2v}$ ) AlC<sub>2</sub> and Calculated Vibrational Frequencies (cm<sup>-1</sup>)**

	CCSD(T)	QCISD/6-311G* (ref 10)
$r_{C-C}$	1.276 Å	1.280 Å
$r_{Al-C}$	1.928 Å	1.937 Å
$\alpha_{C-Al-C}$	38.7°	38.6°
$\omega_1 a_1$	1735	1761
$\omega_2 a_1$	645	624
$\omega_3 b_2$	421	405

**TABLE 2: Vertical Transition Energies (eV) for Excitations with Transition Moments Greater than 0.2 a.u., Calculated at the Minimum Geometry**

transition	CASSCF	MRCI+Q	transition moment (a.u.)
$\tilde{A}^2A_1 - \tilde{X}^2A_1$	1.195	1.200	0.995 (Z)
$\tilde{F}^2A_1 - \tilde{A}^2A_1$	3.011		-0.470 (Z)
$\tilde{E}^2B_2 - \tilde{C}^2B_2$	0.809		0.394 (Z)
$\tilde{B}^2B_1 - \tilde{A}^2A_1$	1.024		-0.334 (X)
$\tilde{D}^2B_1 - \tilde{X}^2A_1$	2.947	3.271	0.335 (X)
$\tilde{D}^2B_1 - \tilde{A}^2A_1$	1.752		-0.230 (X)
$\tilde{C}^2B_2 - \tilde{X}^2A_1$	2.770	2.752	0.471 (Y)
$\tilde{E}^2B_2 - \tilde{X}^2A_1$	3.580	3.830	0.422 (Y)
$\tilde{E}^2B_2 - \tilde{A}^2A_1$	2.385		0.367 (Y)

helium or argon gas (10 bar) provided by a 0.3 mm orifice-pulsed valve. The rod was rotated and translated so that a fresh surface was continuously exposed to the laser, which was fired to coincide with the gas flow over the target area. The vaporization plume flows through a channel (3 mm diameter by 5 mm long) before undergoing a free-jet expansion.

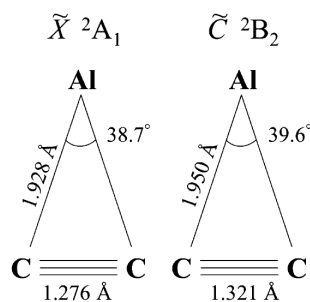
The resulting AlC<sub>2</sub> radicals are then probed through laser-induced fluorescence (LIF) using an excimer-pumped dye laser (0.15 cm<sup>-1</sup>) with a wavemeter used for frequency calibration. The fluorescence signal was collected by an  $f/1$  lens and detected using a photomultiplier and a digital oscilloscope.

## Results

Ab initio calculations using the MOLPRO program<sup>18</sup> with an aug-cc-pVQZ basis set of Dunning et al.<sup>19,20</sup> were carried out for the electronic states of AlC<sub>2</sub>. The coupled cluster with perturbative triples (CCSD(T)) method was used for the description of the  $\tilde{X}^2A_1$  ground state. For comparison, the ground-state linear  $^2\Sigma_g^+$  isomer AlCC was also calculated and found to lie 0.70 eV higher in energy. The optimized geometries for the electronic  $C_{2v}$  ground state and the harmonic frequencies of the fundamental vibrational transitions are compared with previous work in Table 1.<sup>10</sup>

The vertical transition energies for the lowest excited states whose transition moments are greater than 0.2 au are listed in Table 2 at the ground state equilibrium geometry. Full valence CASSCF calculations were performed with 8 states (3  $a_1$ , 2  $b_1$ , 2  $b_2$ , 1  $a_2$ , all in  $C_{2v}$  symmetry). Higher level calculations for vertical transitions originating from the  $\tilde{X}^2A_1$  state have also been performed at the MRCI level of theory with the results listed in Table 2. Finally, the excited  $\tilde{C}^2B_2$  state has been optimized at the MRCI level of theory in  $C_{2v}$  geometry. The minimum lies 2.684 eV above the  $\tilde{X}^2A_1$  ground state. The geometries calculated for the upper and lower states are shown in Figure 1.

The bottom trace in Figure 2 shows the experimental spectrum (0.15 cm<sup>-1</sup> resolution) for the  $\tilde{C}^2B_2 - \tilde{X}^2A_1$  transition of AlC<sub>2</sub>. The signal was dependent on the presence of aluminum. The spectrum was not observed when acetylene was missing from the buffer gas mixture, indicating that carbon and/or hydrogen must be present in the spectral carrier. Substituting deuterated acetylene had no effect, thus eliminating the role of hydrogen.

**Figure 1.** Optimized geometries for the AlC<sub>2</sub> radical calculated at the CASSCF level of theory.

The recorded spectrum was thus assigned to the  $\tilde{C}^2B_2 - \tilde{X}^2A_1$  transition of AlC<sub>2</sub>, one of the stronger transitions listed in Table 2, based on its observed frequency. Scanning to the red revealed no additional band systems, thereby allowing a confident assignment of the observed band as the origin of the  $\tilde{C}^2B_2 - \tilde{X}^2A_1$  transition.

Decay curves were measured for 21 rotational peaks in the origin band of the  $\tilde{C}^2B_2 - \tilde{X}^2A_1$  transition of AlC<sub>2</sub>, in the range from 22 065 to 22 116 cm<sup>-1</sup>. The decay curves appeared exponential and were found to vary from 140 to 640 ns. This substantial scatter is shown graphically in Figure 3 where the measured lifetimes are plotted above a portion of the experimental spectrum reproduced from Figure 2.

## Discussion

A rotational analysis using the program “WANG” was performed with a conventional Hamiltonian for an asymmetric top assuming a  $b$ -type transition in a  $C_{2v}$  molecule.<sup>21</sup> In particular six Q-branch heads, which are associated with  $\Delta K \pm 1$  subbands that result from the perpendicular nature of the transition, were used to guide the fit. These are labeled in Figure 2 using the notation  $Q(K_a' - K_a'')$ . In all, a selection of 14 lines, including P-branch lines from the  $K_a' - K_a''$  (3-4) and  $K_a' - K_a''$  (1-0) manifolds, was included in the least-squares optimization to obtain the best parameters for the rotational analysis. Any increase in the number of fitted lines tended to be detrimental to achieving a successful fit, presumably because of the substantial blending of lines due to the limited resolution achievable in measuring the experimental spectrum. The temperature used for modeling the spectrum was 70 K and the line width was fixed at 0.15 cm<sup>-1</sup>. The resulting simulation is shown as the upper trace in Figure 2.

As with SiC<sub>2</sub>,<sup>3</sup> the two carbon atoms in this molecule are equivalent and interchangeable through rotation around the “ $a$ ”-inertial axis. In a near-prolate asymmetric top, equivalent zero spin nuclei that are symmetric with respect to rotation about the “ $b$ ”-axis will produce alternation in the  $J$  structure. Here, in a  $C_{2v}$  geometry, the equivalent zero-spin nuclei are identical through 2-fold rotation about the  $a$ -axis, producing alternation in the  $K$  rotational structure ( $K_a$ ). For AlC<sub>2</sub> the nuclear spin statistical weights of odd  $K_a''$  levels ( $K_a'' = 1, 3, \dots$ ) are zero, hence there should be no evidence of any sub-bands originating from these states. Taking into account these alternation effects is essential for the fitted spectrum to more closely resemble the observed one, offering further verification of the spectral carrier.

However, as may be seen from the comparison shown in Figure 2, a perfect fit between the rotational analysis and the experimental spectrum was not achieved. This may be attributed to two factors. One possibility is that  $\tilde{C}^2B_2$  rovibronic levels

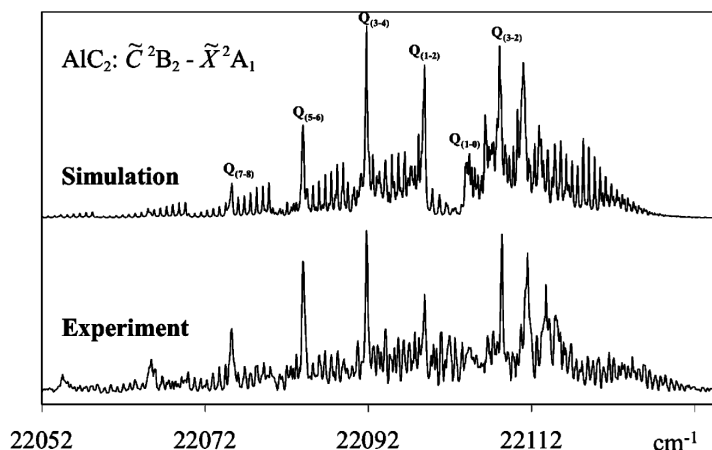


**Figure 2.** The origin band in the  $\tilde{C}^2B_2 - \tilde{X}^2A_1$  electronic transition for  $AlC_2$ , recorded via laser-induced fluorescence. The lower trace is the experimental spectrum, while the upper trace depicts the simulated fit. Q-branch heads that are associated with  $\Delta K \pm 1$  sub-bands and were used to guide the spectral fit are labeled  $Q(K'_a - K''_a)$ .

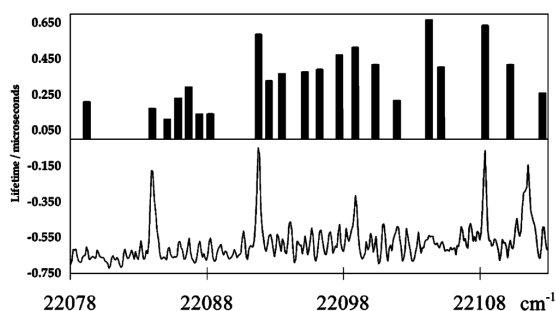


**Figure 3.** The origin band in the  $\tilde{C}^2B_2 - \tilde{X}^2A_1$  electronic transition for  $AlC_2$ , reproduced from Figure 2. Above the spectrum lie depictions of the fluorescent lifetimes measured.

are perturbed as a result of rovibronic coupling with levels associated with lower lying electronic states. These can include near-degenerate  $b_2$  levels of the  $\tilde{A}^2A_1$  and  $\tilde{X}^2A_1$  states or lower lying quartet states that have not yet been located. Through vibronic and Coriolis operators  $A_1$ ,  $A_2$ , and  $B_1$  states may also interact in a rotational-dependent manner, thus perhaps also perturbing the observed system.

The lifetimes of various lines in the spectrum were measured in an effort to qualitatively examine the extent of mixing among the electronic states in  $AlC_2$ , giving rise to the wide variation in  $\tau$  depicted in Figure 3. In an earlier study on the  $\tilde{A}^1B_1 - \tilde{X}^1A_1$  transition of  $SiH_2$  ( $C_{2v}$ ), wide variations in the fluorescent lifetimes of individual rotational lines (few nanoseconds to  $>1 \mu s$ ) were attributed to rovibronic perturbations.<sup>22,23</sup> Specifically, rovibronic levels in the  $SiH_2 \tilde{A}^1B_1$  state mix with background levels from either the lower lying  $\tilde{a}^3B_1$  state or highly excited vibrational levels from the  $\tilde{X}^1A_1$  ground state, leading to perturbations in the energy levels and oscillator strengths and thus making a spectral fit impossible using a standard rotational Hamiltonian. Similar behavior has also been reported for the fluorescence decay rates found in the  $S_1$  ( $\tilde{A}^1A_2$ ) states of formaldehyde.<sup>24,25</sup>

This mixing can be sensitive to rotational quantum number<sup>26</sup> and the proximity and identity of near degenerate background states, leading to seemingly random perturbations in oscillator strengths and energy level positions and thereby influencing the experimental measurement of the rotational contour. Figure 3

shows that some Q-branch band maxima associated with the  $\Delta K \pm 1$  sub-bands possess lifetimes up to 2–3 times longer than other lines. These longer lifetimes may arise due to quartet dilution, whereby a substantial fraction of spin forbidden quartet character is added to the emitting  $\tilde{C}^2B_2$  state. Conversely, other high  $J$ -levels demonstrate shortened lifetimes, which may be due to a stronger coupling with  $b_2$  vibronic states from the  $\tilde{A}^2A_1$  and  $\tilde{X}^2A_1$  electronic states, resulting in increased non-radiative decay rates.

A second reason for the imperfect fit to the experimentally observed spectrum may derive from a non-Boltzmann temperature distribution in the jet: that is, in an expanding jet the  $J$ -levels cool more efficiently than the  $K$ -levels. This has been previously observed in beams of glyoxal<sup>27</sup> and acetaldehyde<sup>28</sup> that were also studied using LIF. In the case of acetaldehyde, the rotational temperature for molecules in the beam was found to be over four times higher in  $K$ -quantum number than in  $J$ . This same effect is apparent in the spectral simulation of  $AlC_2$ , where at 70 K the  $J$ -temperature seems to fit reasonably well; however, the intensity distribution in the Q-branch heads appears to fall faster than in the experimental spectrum. This would seem to indicate that to correctly simulate the spectrum one would have to model an increased  $K$ -temperature while holding the  $J$ -temperature at its current value. This has not been carried out at this stage because a reasonable fit was obtained yielding rotational constants consistent with the theoretical structures calculated for the  $\tilde{X}^2A_1$  and  $\tilde{C}^2B_2$  states.

The molecular constants obtained are given in Table 3, along with the corresponding MRCI calculated values. Conservative errors were qualitatively estimated through fixing the resulting constants and then systematically varying each parameter. In general, constants could be varied by approximately twice the value of the standard deviations derived from the spectral fitting procedure before the modeled spectrum significantly differed from the experimentally obtained one. Error in  $T_0$  stems from the spectral line width used to measure the transition.

Geometric structures can be estimated from the rotational constants derived in the spectroscopic fit, with the C–C bond length calculated directly from the  $A$  constants. This yields  $r_{Al-C}$  and  $r_{C-C}$  as 1.93 and 1.28 Å for the  $\tilde{X}^2A_1$  ground state, and 1.94 and 1.34 Å for the excited  $\tilde{C}^2B_2$  state. All values are within error of the calculated CASSCF geometries shown in Figure 1.

**TABLE 3: Rotational Constants (cm<sup>-1</sup>) Obtained from a Geometry Optimization Performed at the MRCI Level of Theory and from the Rotational Analysis<sup>a</sup>**

	MRCI	spectral fit
	$\tilde{X}^2A_1$	
A''	1.725 cm <sup>-1</sup>	1.7093(107) cm <sup>-1</sup>
B''	0.400 cm <sup>-1</sup>	0.4052(50) cm <sup>-1</sup>
C''	0.325 cm <sup>-1</sup>	0.3228(49) cm <sup>-1</sup>
	$\tilde{C}^2B_2$	
A'	1.609 cm <sup>-1</sup>	1.5621(137) cm <sup>-1</sup>
B'	0.394 cm <sup>-1</sup>	0.4028(46) cm <sup>-1</sup>
C'	0.316 cm <sup>-1</sup>	0.3201(54) cm <sup>-1</sup>
T <sub>0</sub>		22102.7 ± 0.2 cm <sup>-1</sup>

<sup>a</sup> Errors in the rotational constants represent twice the standard deviations derived from the fit.

### Conclusion

The electronic spectrum of AlC<sub>2</sub> was observed using an ablation source and laser induced fluorescence detection. The experiments demonstrated that the spectral carrier contained only Al and C atoms. The rotationally resolved spectrum was assigned to the origin band of the  $\tilde{C}^2B_2-\tilde{X}^2A_1$  system, a species that exists in a planar C<sub>2v</sub> geometry as previously calculated. A rotational analysis is consistent with the asymmetric top AlC<sub>2</sub> (C<sub>2v</sub>), further evidenced by the fact that nuclear spin effects due to two equivalent carbon atoms must be considered to properly model the experimental spectrum.

Molecular constants were estimated using a spectral simulation based on a least-squares fit to 14 individual lines. Spectroscopic constants obtained from the fit compare reasonably well with ab initio calculations performed on both the ground and excited states. The imperfect nature of the fit is attributed to an inability to account for substantial interactions with lower lying quartet and <sup>2</sup>A<sub>1</sub> states that manifest themselves as irregular perturbations in both the energy levels and their oscillator strengths. Being able to incorporate a non-Boltzmann temperature dependence for the *J*- and *K*-levels may also enable a more accurate fit. However, as it stands, the fit confirms the perpendicular nature of the  $\tilde{C}^2B_2-\tilde{X}^2A_1$  transition.

Finally, further confirmation of the carrier's identity was obtained using a resonant 2-color 2-photon ionization technique, where a spectrum of AlC<sub>2</sub> was observed in the same 452 nm region for the *m/z* 51 mass.<sup>29</sup> A more detailed analysis awaits the collection of a higher resolution spectrum.

No matches corresponding to the diffuse interstellar band literature were found for the origin band of AlC<sub>2</sub>; however, the information obtained in this study can aid further attempts to

identify this dicarbide species in interstellar space by means of its electronic spectrum. The spectroscopic constants also offer a guide for future microwave investigations.

**Acknowledgment.** We thank Professor Alan E. W. Knight for helpful discussions. This work has been supported by the Swiss National Science Foundation (Grant 200020-115864/1) and the European Office of Aerospace Research and Development (Grant FA8655-07-1-30310).

### References and Notes

- (1) Cernicharo, J.; Guélin, M. *Astron. Astrophys.* **1987**, *183*, L10.
- (2) Ziurys, L. M.; Savage, C.; Highberger, J. L.; Apponi, A. J.; Guélin, M.; Cernicharo, J. *Astrophys. J.* **2002**, *564*, L45.
- (3) Michalopoulos, D. L.; Geusic, M. E.; Langridge-Smith, P. R. R.; Smalley, R. E. *J. Chem. Phys.* **1984**, *80*, 3556.
- (4) Grev, R. S.; Schaefer, H. F. *J. Chem. Phys.* **1984**, *80*, 3552.
- (5) Douglas, A. E. *Astrophys. J.* **1951**, *114*, 466.
- (6) Clusius, K.; Douglas, A. E. *Can. J. Phys.* **1954**, *32*, 319.
- (7) Flores, J. R.; Largo, A. *Chem. Phys.* **1990**, *140*, 19.
- (8) Chertihin, G. V.; Andrews, L.; Taylor, P. R. *J. Am. Chem. Soc.* **1994**, *116*, 3513.
- (9) Yang, H.; Tanaka, K.; Shinada, M. *THEOCHEM-J. Mol. Struct.* **1998**, *422*, 159.
- (10) Zheng, X.; Wang, Z.; Tang, A. *J. Phys. Chem. A* **1999**, *103*, 9275.
- (11) Redondo, P.; Barrientos, C.; Largo, A. *Int. J. Quantum Chem.* **2004**, *96*, 615.
- (12) Green, S. *Chem. Phys. Lett.* **1984**, *112*, 29.
- (13) Steimle, T. C.; Marr, A. J.; Xin, J.; Merer, A. J.; Athanassenas, K.; Gillet, D. *J. Chem. Phys.* **1997**, *106*, 2060.
- (14) Steimle, T. C.; Bousquet, R. R.; Namiki, K. C.; Merer, A. J. *J. Mol. Spectrosc.* **2002**, *215*, 10.
- (15) Bousquet, R. R.; Steimle, T. C. *J. Chem. Phys.* **2001**, *114*, 1306.
- (16) Knight, L. B.; Cobranchi, S. T.; Herlong, J. O.; Arrington, C. A. *J. Chem. Phys.* **1990**, *92*, 5856.
- (17) Boldyrev, A. I.; Simons, J.; Li, X.; Wang, L.-S. *J. Am. Chem. Soc.* **1999**, *121*, 10193.
- (18) Werner, J.-J.; Knowles, P. J. MOLPRO; <http://www.molpro.net>.
- (19) Dunning, T. H. *J. Chem. Phys.* **1989**, *90*, 1007.
- (20) Kendall, R. A.; Dunning, T. H.; Harrison, R. J. *J. Chem. Phys.* **1992**, *96*, 6796.
- (21) Luckhaus, D.; Quack, M. *Mol. Phys.* **1989**, *68*, 745.
- (22) Thoman, J. W.; Steinfeld, J. I.; McKay, R. I.; Knight, A. E. W. *J. Chem. Phys.* **1987**, *86*, 5909.
- (23) McKay, R. I.; Uichanco, A. S.; Bradley, A. J.; Holdsworth, J. R.; Francisco, J. S.; Steinfeld, J. I.; Knight, A. E. W. *J. Chem. Phys.* **1991**, *95*, 1688.
- (24) Weisshaar, J. C.; Moore, C. B. *J. Chem. Phys.* **1980**, *72*, 5415.
- (25) Guyer, D. R.; Polik, W. F.; Moore, C. B. *J. Chem. Phys.* **1986**, *84*, 6519.
- (26) Knight, A. E. W. Rotational Involvement in Intramolecular Vibrational Redistribution. In *Excited States*; Lim, E. C., Ed.; Academic Press: New York, 1988; Vol. 7.
- (27) Peyroula, E. P.; Jost, R. *J. Mol. Spectrosc.* **1987**, *121*, 167.
- (28) Price, J. M.; Mack, J. A.; von Helden, G.; Yang, X.; Wodtke, A. M. *J. Phys. Chem.* **1994**, *98*, 1791.
- (29) Apetrei, C.; Chasovskikh, E.; Ding, H.; Jochnowitz, E. B.; Maier, J. P. In preparation.

## Chapter 7

# Electronic spectra of the $\text{MgC}_4\text{H}$ and $\text{MgC}_6\text{H}$ radical

## Electronic Spectra of the MgC<sub>4</sub>H and MgC<sub>6</sub>H Radicals

Egor Chasovskikh, Evan B. Jochowitz, and John P. Maier\*

Department of Chemistry, University of Basel, Klingelbergstrasse 80, CH-4056, Basel, Switzerland

Received: May 6, 2008; Revised Manuscript Received: June 17, 2008

Electronic transitions of the linear MgC<sub>4</sub>H and MgC<sub>6</sub>H radicals have been observed in the gas phase using laser-induced fluorescence spectroscopy. The species were prepared in a supersonic expansion by ablation of a magnesium rod in the presence of acetylene, diacetylene, or methane gas. The transitions were recorded in the 445–446 nm region and assigned to the A <sup>2</sup>Π–X <sup>2</sup>Σ<sup>+</sup> systems ( $T_0 = 22\,431.978(7)$  and  $22\,090.08(7)$  cm<sup>-1</sup>) based on previously reported mass-selective resonance-enhanced ionization spectra and the rotational structure. A spectral fit in MgC<sub>4</sub>H yields the rotational constants  $B'' = 0.04619(19)$  cm<sup>-1</sup> for the X <sup>2</sup>Σ<sup>+</sup> state and  $B' = 0.04748(20)$  cm<sup>-1</sup> for A <sup>2</sup>Π. Astrophysical implications are briefly addressed.

### 1. Introduction

Metal-containing molecules, such as MgCN, have been detected in the circumstellar envelopes of carbon-rich stars through radioastronomy.<sup>1</sup> Given the fact that Al and Mg are among the most common metallic elements found in the diffuse medium, one has to wonder whether carbon chains containing them might be responsible for the appearance of some of the diffuse interstellar bands, absorptions observed through diffuse clouds in the visible region.<sup>2</sup> In 1977 Douglas conjectured that carbon chains of size C<sub>n</sub>,  $n = 5–10$ , might be responsible as carriers for some of bands;<sup>3</sup> however, thus far all gas-phase comparisons have proved negative.<sup>4</sup> Could metal-capped chains, which absorb in the proper visible region (400–800 nm) with sufficient oscillator strengths, be likely candidates?

Recently our group has reported the A <sup>1</sup>Π–X <sup>1</sup>Σ<sup>+</sup> spectrum of AICCH in the gas phase.<sup>5</sup> Like its open-shelled counterpart, MgCCH, AICCH clearly demonstrates a linear Π–Σ transition. Previously, rotationally resolved electronic spectra of MgCCH radical were observed, yielding accurate rotational constants for the A <sup>2</sup>Π–X <sup>2</sup>Σ<sup>+</sup> system.<sup>6,7</sup> Other electronically observed metal-capped acetylides include the CaCCH and SrCCH radicals,<sup>8</sup> where detailed use of Stark spectroscopy led to determination of the dipole moment of the calcium-containing species.<sup>9</sup> As far as other metal monoacetylides are concerned, LiCCH,<sup>10</sup> NaCCH,<sup>11</sup> and KCCH<sup>12</sup> have all been shown to have linear <sup>1</sup>Σ<sup>+</sup> ground states through rotational spectroscopy.

Only within the past year were the first gas-phase spectra of MgC<sub>4</sub>H and MgC<sub>6</sub>H obtained using a mass-selective resonant 2-color 2-photon ionization (R2C2PI) method with origin bands at 445.3 and 452.5 nm, respectively.<sup>13</sup> The systems were found to have significant oscillator strengths ( $f \approx 0.1$ ) with the electronic excitation being localized on the Mg atom. Having the low-resolution R2C2PI spectra in hand, it was possible to investigate the A <sup>2</sup>Π–X <sup>2</sup>Σ<sup>+</sup> systems of MgC<sub>4</sub>H and MgC<sub>6</sub>H in more detail using the higher sensitivity afforded through laser-induced fluorescence. Note that only the origin band of the A <sup>2</sup>Π–X <sup>2</sup>Σ<sup>+</sup> MgC<sub>4</sub>H system was investigated; as shown in previous mass-selective R2C2PI studies, exciting the Mg–C bond in the A <sup>2</sup>Π state of MgC<sub>4</sub>H results in a weak overlapping band with the origin system of MgCCH.<sup>13</sup>

\* To whom correspondence should be addressed. Fax: +41-61-267-38-55. E-mail: j.p.maier@unibas.ch.

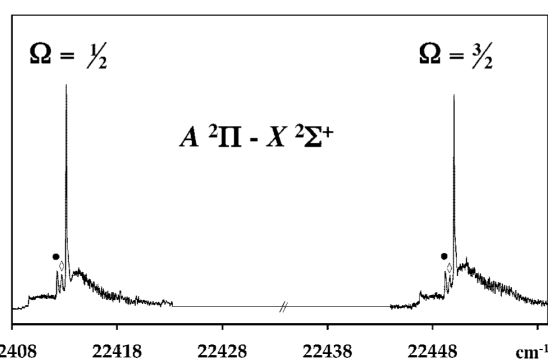


**Figure 1.** Observed  $\Omega = 1/2$  and  $3/2$  components of the origin band in the A <sup>2</sup>Π–X <sup>2</sup>Σ<sup>+</sup> electronic spectrum of MgC<sub>4</sub>H measured using laser-induced fluorescence in a supersonic molecular beam. The main peaks are assigned to the most abundant isotopomer, <sup>24</sup>MgC<sub>4</sub>H, with <sup>25</sup>MgC<sub>4</sub>H and <sup>26</sup>MgC<sub>4</sub>H denoted by  $\diamond$  and  $\bullet$ , respectively.

### 2. Experimental Section

Jet-cooled MgC<sub>n</sub>H was produced using laser vaporization (532 nm) of a pure magnesium rod in a flow of 5% acetylene, diacetylene, or methane in argon gas (10 bar) provided by a 0.3 mm orifice pulsed valve. The rod was rotated and translated so that a fresh surface was continuously exposed to the laser, which was fired to coincide with the gas flow over the target area. The vaporization plume flows through a channel (3 mm diameter by 5 mm long) before undergoing a free jet expansion. The resulting radicals are then probed through laser-induced fluorescence (LIF) using a Nd:YAG pumped dye laser (0.07 cm<sup>-1</sup>) with a wavemeter used for frequency calibration (Burleigh WA4500). The fluorescence signal was collected by an  $f/1$  lens and detected using a photomultiplier tube and a digital oscilloscope.

### 3. Results

**3.1. MgC<sub>4</sub>H. Identification of the Carrier.** Figure 1 shows the excitation spectrum obtained in the 22408–22459 cm<sup>-1</sup> region when ablating magnesium in the presence of methane. The LIF signal displayed a dependence on the presence of magnesium and hydrocarbon precursor. The general appearance of a PQR pattern with two spin–orbit components separated

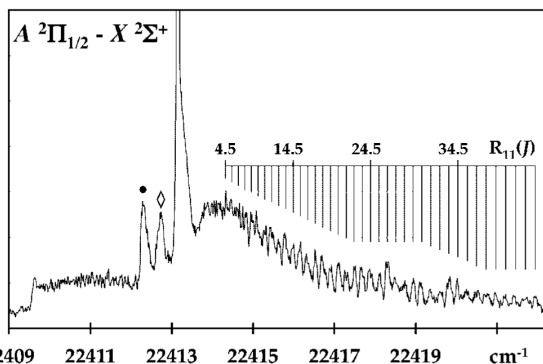


**Figure 2.**  $\Omega = 1/2$  component in the origin band of the  $A \ ^2\Pi_{1/2} - X \ ^2\Sigma^+$  electronic transition for MgC<sub>4</sub>H. (◇ and ●) Less abundant species  $^{25}\text{MgC}_4\text{H}$  and  $^{26}\text{MgC}_4\text{H}$ , respectively.

by nearly  $37 \text{ cm}^{-1}$  suggests a typical  $^2\Pi - ^2\Sigma^+$  system. Previous ab initio calculations predict a linear  $^2\Sigma^+$  ground-state structure with  $C_{\infty v}$  symmetry.<sup>13</sup> The frequency positions determined from the low-resolution R2C2PI spectra of MgC<sub>n</sub>H ( $n = 2, 4, 6$ ) allowed an assignment of the observed bands with the symmetries of the transitions known on the basis of calculation; the bands depicted in Figure 1 clearly belong to MgC<sub>4</sub>H. A band origin at 2.78 eV lies just below the vertical electronic excitation energy of 2.79 eV calculated for the  $A \ ^2\Pi - X \ ^2\Sigma^+$  transition using TD-B3LYP methods combined with a cc-pVTZ basis set.<sup>13</sup> Furthermore, the rotational constants obtained are on the order of those expected from DFT calculations.

The nature of the spin-orbit band indicates the presence of a doubly degenerate excited electronic state. This doublet splitting of about  $37 \text{ cm}^{-1}$ , similar in magnitude to the spin-orbit splittings observed in other magnesium compounds, including MgH ( $35.3 \text{ cm}^{-1}$ ),<sup>14</sup> MgCH<sub>3</sub> ( $28.6 \text{ cm}^{-1}$ ),<sup>15</sup> MgNC ( $36.9 \text{ cm}^{-1}$ ),<sup>16</sup> and MgCCH ( $36.1 \text{ cm}^{-1}$ ),<sup>7</sup> further implies that the transition is metal centered and does not vary significantly with ligand size or composition.

Labeled in Figure 1 are two additional bandheads due to less abundant isotopic isomers of Mg,  $^{25}\text{MgC}_4\text{H}$  (10%), and  $^{26}\text{MgC}_4\text{H}$  (11%). While this observation allows an assignment of their origin location and excited-state spin-orbit splitting, their weak intensities and overlapping features precludes a proper rotational analysis for these minor constituents.

**Rotational Structure.** Modest resolution spectra were obtained with a Nd:YAG pumped dye laser ( $0.07 \text{ cm}^{-1}$ ). The trace in Figure 2 shows the  $\Omega = 1/2$  spin-orbit component displayed in Figure 1. A similar profile was observed at  $22450.46 \text{ cm}^{-1}$  for  $\Omega = 3/2$ . The profile of the band fits that expected from a  $^2\Pi - ^2\Sigma^+$  transition. With the spin-orbit constant  $A \gg BJ$ , the excited state of MgC<sub>4</sub>H belongs to Hund's Case (a).

For MgC<sub>4</sub>H, the strong bandheads in the  $A \ ^2\Pi_{1/2} - X \ ^2\Sigma^+$  spin component are Q<sub>12</sub> and P<sub>11</sub>, while for the  $A \ ^2\Pi_{3/2} - X \ ^2\Sigma^+$  spin component they are Q<sub>22</sub> and P<sub>22</sub>.<sup>17</sup> Fanning out to higher energy lie the R<sub>11</sub>/R<sub>12</sub> and R<sub>21</sub>/R<sub>22</sub> branches for the  $\Omega = 1/2$  and  $3/2$  components, respectively, with the R<sub>11</sub> and R<sub>21</sub> lines being much higher in intensity and therefore suitable for rotational analysis. Also, in both the R<sub>11</sub> and R<sub>21</sub> branches line spacings are on the order of  $3B$ , allowing reasonable peak separation at the given resolution ( $0.07 \text{ cm}^{-1}$ ). In general, for such a  $^2\Pi$  (case a)  $- ^2\Sigma^+$  (case b) transition one expects to observe rotational structure with line spacings of both  $3B$

**TABLE 1: Observed Rotational Lines (in  $\text{cm}^{-1}$ ) of the Origin Band in the  $A \ ^2\Pi - X \ ^2\Sigma^+$  Electronic Transition of  $^{24}\text{MgC}_4\text{H}^a$**

$J$	$A \ ^2\Pi_{1/2} - X \ ^2\Sigma^+$		$A \ ^2\Pi_{3/2} - X \ ^2\Sigma^+$	
	R <sub>11</sub> branch		R <sub>21</sub> branch	
	$\tilde{\nu}_{\text{obs}}$	$\tilde{\nu}_{\text{obs}} - \tilde{\nu}_{\text{calcd}}$	$\tilde{\nu}_{\text{obs}}$	$\tilde{\nu}_{\text{obs}} - \tilde{\nu}_{\text{calcd}}$
4.5	22414.332	0.006		
5.5	22414.489	0.007		
6.5	22414.646	0.007		
7.5	22414.816	0.017	22451.676	-0.002
8.5	22414.956	-0.005	22451.847	0.005
9.5	22415.116	-0.010	22452.005	-0.004
10.5	22415.287	-0.007	22452.169	-0.010
11.5	22415.482	0.020	22452.345	-0.006
12.5	22415.629	-0.005	22452.528	0.002
13.5	22415.804	-0.004	22452.701	-0.004
14.5	22415.991	0.006	22452.886	0.001
15.5	22416.170	0.006	22453.071	0.003
16.5	22416.358	0.011	22453.248	-0.007
17.5	22416.531	-0.001	22453.435	-0.009
18.5	22416.715	-0.002	22453.620	-0.015
19.5	22416.901	-0.006	22453.834	0.005
20.5	22417.097	-0.002	22454.032	0.006
21.5	22417.301	0.008	22454.230	0.003
22.5	22417.486	-0.003	22454.426	-0.003
23.5	22417.669	-0.020	22454.628	-0.007
24.5	22417.899	0.009	22454.844	0.002
25.5	22418.107	0.012	22455.067	0.015
26.5	22418.301	-0.007	22455.268	0.003
27.5	22418.498	-0.012	22455.470	-0.012
28.5	22418.733	0.011	22455.709	0.008
29.5	22418.943	0.007	22455.942	0.020
30.5	22419.121	-0.031	22456.136	-0.011
31.5	22419.356	-0.015	22456.360	-0.013
32.5	22419.611	0.018	22456.606	0.003
33.5	22419.838	0.021	22456.834	-0.001
34.5	22420.022	-0.021	22457.068	-0.002
35.5	22420.270	-0.002	22457.298	-0.011
36.5	22420.538	0.034	22457.554	0.006
37.5	22420.752	0.014	22457.779	-0.013
38.5	22420.957	-0.017	22458.040	0.002
39.5	22421.201	-0.012	22458.291	0.004
40.5	22421.417	-0.037	22458.549	0.011
41.5	22421.715	0.018	22458.799	0.007
42.5	22421.940	-0.004	22459.046	-0.003
43.5	22422.216	0.024	22459.306	-0.003
44.5	22422.428	-0.016	22459.588	0.017
45.5	22422.694	-0.003	22459.845	0.009
46.5	22422.952	-0.001	22460.106	0.003
47.5	22423.198	-0.014	22460.374	0.001

<sup>a</sup> The uncertainty of the  $\tilde{\nu}_{\text{obs}}$  values given is judged to be  $\pm 0.007 \text{ cm}^{-1}$ .

(R<sub>11</sub>, R<sub>21</sub>, P<sub>12</sub>, and P<sub>22</sub>) as well as B (R<sub>12</sub>, R<sub>22</sub>, P<sub>11</sub>, and P<sub>21</sub>) in the two spin-orbit components.

A rotational fit was performed for a  $^2\Pi - ^2\Sigma^+$  transition in a linear molecule using the PGOPHER program.<sup>18</sup> The calculated spectrum was obtained by first varying the rotational parameters  $B''$  and  $B'$ , the excited state's spin-orbit coupling constant, as well as the line width, temperature, and origin assignment. At this resolution, lines belonging to the R<sub>11</sub> and R<sub>21</sub> branches could be singled out due to their greater peak separation ( $\sim 3B$ ). Rotational line assignments were made by comparing the observed spectral lines with those calculated. A spectral least-squares fit using 85 R-branch lines could be performed, allowing the determination of six varied spectroscopic parameters at a temperature of 50 K and a line width fixed at  $0.07 \text{ cm}^{-1}$  (Tables 1 and 2). Variations in line intensities of the experimental spectra are mainly due to instability in the ablation source. Higher



**TABLE 2: Constants Determined from the Analysis of the Electronic Spectrum of  $^{24}\text{MgC}_4\text{H}^a$** 

parameter	$X^2\Sigma^+$	$A^2\Pi$
$T_0/\text{cm}^{-1}$		22431.978(7)
$B/\text{cm}^{-1}$	0.04619(19)	0.04748(20)
$A/\text{cm}^{-1}$		36.964(3)

<sup>a</sup> Values in parentheses denote the  $2\sigma$  standard deviation from the fit.

**TABLE 3: Origin Band Wavenumbers and Spin–Orbit Constants for the  $A^2\Pi-X^2\Sigma^+$  Transition in the  $\text{MgC}_4\text{H}$  Isotopomers<sup>a</sup>**

	$^{24}\text{MgC}_4\text{H}$	$^{25}\text{MgC}_4\text{H}$	$^{26}\text{MgC}_4\text{H}$
$T_0/\text{cm}^{-1}$	22431.978(7)	22431.53(7)	22431.11(7)
$A/\text{cm}^{-1}$	36.964(3)	36.97(7)	36.99(7)

<sup>a</sup> Constants obtained for  $^{25}\text{MgC}_4\text{H}$  and  $^{26}\text{MgC}_4\text{H}$  from measurement of the band head positions and not from a rotational analysis.

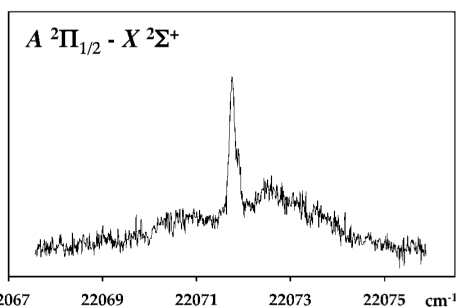


**Figure 3.**  $\Omega = 1/2$  component in the origin band of the  $A^2\Pi-X^2\Sigma^+$  electronic transition for  $\text{MgC}_6\text{H}$  measured using laser-induced fluorescence in a supersonic molecular beam, featuring the prominent  $Q_{12}/P_{11}$  bandhead.

resolution experiments will be required to identify spectroscopic terms with a larger degree of accuracy using additional weaker  $R_{12}/R_{22}$  lines which could not be distinguished currently due to the spectral density that results from their smaller spacings ( $\sim B$ ). Likewise, the shape of the bandhead and overlapping isotopic species made individual assignment of any P- and Q-branch lines impossible.

The two isotopic isomers ( $^{25}\text{MgC}_4\text{H}$  and  $^{26}\text{MgC}_4\text{H}$ ) located to the red of the major abundant species ( $^{24}\text{MgC}_4\text{H}$ ) clearly contribute to the band profile observed in the experimental spectrum in Figure 1. For these less abundant species their band origin  $T_0$  and spin–orbit constant  $A$  were varied until a reasonable visual agreement was achieved with the experiment (Table 3). A least-squares fit was not attempted due to the weakness of their overlapping features. While the presence of these isotopomers made the assignment of any P-branch lines difficult, they did not, however, interfere with lines from the  $R_{11}/R_{21}$  branches of the major  $^{24}\text{MgC}_4\text{H}$  species and thus do not lead to any discrepancies concerning its rotational fit. The ground-state rotational constant  $B''$  obtained,  $0.04619(19)\text{ cm}^{-1}$ , agrees reasonably with the literature calculated values of  $0.04612$  and  $0.04508\text{ cm}^{-1}$  for the B3LYP and RCCSD(T) methods, respectively.<sup>13</sup>

Time profiles of the fluorescence decay were measured by tuning the laser frequency to the bandhead of each spin–orbit component in the  $A^2\Pi-X^2\Sigma^+$  transition of  $\text{MgC}_4\text{H}$ , yielding fluorescence lifetimes on the order of 35 ns.

**3.2.  $\text{MgC}_6\text{H}$ .** Figure 3 shows the  $A^2\Pi_{1/2}-X^2\Sigma^+$  electronic transition for  $\text{MgC}_6\text{H}$ , located at  $22071.94\text{ cm}^{-1}$ . The less intense

**TABLE 4: Origin Band Positions and Calculated Vertical Excitation Energies (in eV) for the  $A^2\Pi-X^2\Sigma^+$  Transition in the  $\text{MgC}_n\text{H}$  Series**

	experiment	B3LYP <sup>a</sup>	RCCSD(T) <sup>a</sup>
$\text{MgC}_2\text{H}$	2.83 <sup>b</sup>	2.92	2.87
$\text{MgC}_4\text{H}$	2.78	2.79	2.84
$\text{MgC}_6\text{H}$	2.74 <sup>c</sup>	2.65	2.81

<sup>a</sup> Reference 13. <sup>b</sup> Reference 7. <sup>c</sup> From measurement of the band head positions and not from a rotational analysis.

$A^2\Pi_{3/2}-X^2\Sigma^+$  component was located at  $22108.22\text{ cm}^{-1}$ . Clearly evident is how the general shape of the  $\Omega = 1/2$  band resembles that of  $\text{MgC}_4\text{H}$ , shown in Figure 2, with a well-defined  $Q_{12}/P_{11}$  branch head. As before, tests involving the presence of magnesium and hydrocarbon precursor,  $37\text{ cm}^{-1}$  spin–orbit splitting, general appearance of a PQR pattern, and previous knowledge of the spectral region to interrogate in addition to mass-selective R2C2PI spectra<sup>13</sup> all confirmed the assignment of the spectral carrier.

The experimental band origin,  $T_0 = 22090.08\text{ cm}^{-1}$  (2.74 eV), lies a bit above the vertical excitation energy of 2.65 eV calculated for the  $A^2\Pi-X^2\Sigma^+$  transition using TD-B3LYP methods. Calculations predict a rotational constant of about  $0.019\text{ cm}^{-1}$ , making the present experimental resolution of  $0.07\text{ cm}^{-1}$  insufficient to resolve the  $B$  or even the  $3B$  spacings expected for individual lines. As far as locating the two isotopic isomers ( $^{25}\text{MgC}_6\text{H}$  and  $^{26}\text{MgC}_6\text{H}$ ), we believe that their weak bandheads must be obscured by the presence of the  $^{24}\text{MgC}_6\text{H}$  species with spectral congestion further prohibiting any clear assignment.

While individual rotational lines could not be assigned due to both the resolution used and the band's weak intensity, visually varying  $T_0$  and  $A$  in the  $A^2\Pi$  state led to an origin assignment of  $22090.08(7)\text{ cm}^{-1}$  and a spin–orbit coupling constant of  $36.28(7)\text{ cm}^{-1}$ . Decay profiles of the  $\text{MgC}_6\text{H}$  band indicate a fluorescence lifetime just shorter than  $\text{MgC}_4\text{H}$ , at about 28 ns.

#### 4. Discussion

The experimental origin band positions for the  $\text{MgC}_n\text{H}$ ,  $n = 2, 4, 6$ , are given in Table 4 along with the previously calculated vertical transition energies. Although a simple TD-DFT method assumes the same geometry in the ground and excited states, decent agreement ( $\sim 0.1\text{ eV}$ ) is found with the experimental result when compared with the entire series. Thus, the TD-DFT predictions support the spectral assignments. Moreover, the assignments are consistent with previous mass-selective R2C2PI spectra and therefore resolve any ambiguity.

Earlier, potential-energy curves were calculated for the  $X^2\Sigma^+$  ground and  $A^2\Pi$  states of  $\text{MgC}_4\text{H}$  as a function of the Mg–C coordinate using the RCCSD(T)/cc-pVTZ level of theory.<sup>13</sup> While the Mg–C bond length is shorter in the excited state, it was argued that the bonding energy in the ground state is actually stronger than that in the  $A^2\Pi$  state (dissociation energies of  $327.6$  versus  $69.0\text{ kJ mol}^{-1}$ ). Weak bonding in the excited state was partially rationalized by an avoided crossing with the  $B^2\Pi$  state. The shorter bond length can be explained using molecular orbital arguments, where excitation from an anti-bonding semioccupied MO to the LUMO leads to bond length contraction, thus accounting for the experimentally observed increase in rotational constant upon excitation.<sup>13,19</sup>

An important aspect of the magnesium-capped chains is their astrophysical significance. As stated earlier, Mg-containing

species have already been detected in carbon-rich stars. Previous calculations have investigated the oscillator strengths of these transitions, which are of interest for astrophysical observation. While the dipole moment increases monotonically with the size of the chain, the oscillator strength of the specific  $A^2\Pi-X^2\Sigma^+$  transition in MgC<sub>*n*</sub>H is calculated to decrease.<sup>13</sup> This behavior differs from that of the polyynes HC<sub>*2n+1*</sub>H chains, which has been attributed to the fact that there the *f* values arise from a delocalized  $\pi$ -electron excitation.<sup>20</sup> In the case of the magnesium-capped chains, the transition arises from promotion of a  $\sigma$ -electron localized on the metal atom. Thus, as the chain becomes larger with increasing *n*, delocalization on the chain acts to remove oscillator strength when the  $\sigma$  electron is excited.

The possibility of MgC<sub>4</sub>H being a reasonably good candidate for the unassigned B1395 lines detected in the envelope of carbon-rich star IRC+10216 has been previously addressed.<sup>21</sup> In particular, the features observed are said to originate from an unidentified linear  $^2\Sigma$  species with  $B_0 = 1.3946$  GHz. While initial considerations point to MgCCCN as the carrier, discussions suggest that MgC<sub>4</sub>H also remains viable; both species have identical ground-state  $^2\Sigma$  symmetries and similar rotational constants ( $B_0(\text{corrected}) = 1.3925$  and  $1.3972$  GHz at the B3LYP/aug-DZ level of theory for MgCCCN and MgC<sub>4</sub>H, respectively.) In the same star Mg- and Al-containing species such as MgNC,<sup>22</sup> MgCN,<sup>1</sup> AlNC,<sup>23</sup> AlCl,<sup>24</sup> and AlF<sup>25</sup> have all been previously observed. It has also been postulated that species such as C<sub>2</sub>H, C<sub>4</sub>H, and C<sub>6</sub>H could be formed in the star's outer shell as the result of photodissociation mechanisms involving CO, C<sub>2</sub>H<sub>2</sub>, and HCN.<sup>26</sup> However, the lack of detection of the smaller MgCCH radical in IRC+10216 seems to imply even lower abundances for MgC<sub>4</sub>H.<sup>21</sup>

Another important consequence of the Mg-terminated chains is the fact that their  $A^2\Pi-X^2\Sigma^+$  electronic transitions occur in the diffuse interstellar band 400–700 nm window. A comparison with the tabulations of the latter absorptions resulted in no corresponding matches.<sup>27</sup> Of note is the fact that the  $A^2\Pi-X^2\Sigma^+$  excitation in MgC<sub>4</sub>H is not the most intense transition. Calculations of the vertical excitation energies using TD-DFT have shown that there are indeed two higher lying and as of yet undetected excitations:  $A^2\Pi-X^2\Sigma^+$  (2.79 eV,  $f = 0.09$ ),  $B^2\Pi-X^2\Sigma^+$  (3.05 eV,  $f = 0.02$ ), and  $C^2\Sigma^+-X^2\Sigma^+$  (4.49 eV,  $f = 0.29$ ).<sup>13</sup>

## 5. Conclusions

The rotationally resolved laser excitation spectrum of the origin band for the  $A^2\Pi-X^2\Sigma^+$  band of MgC<sub>4</sub>H has been observed and analyzed. A spectral fit yields rotational constants for the ground and first excited states, allowing for further investigations into this important class of metal-capped carbon chains, which may aid the search for the millimeter-wave spectrum of MgC<sub>4</sub>H in the laboratory. Weak electronic absorp-

tion for the larger MgC<sub>6</sub>H radical has been observed. Poor production and a smaller oscillator strength as well as line spacings which are unresolvable at the current resolution prohibited a proper rotational analysis; however, the origin band location and spin-orbit splitting could be estimated. These data provide the means of identifying the MgC<sub>*n*</sub>H,  $n = 4$  and 6, species in various environments by electronic spectroscopy.

**Acknowledgment.** This work was supported by the Swiss National Science Foundation (project no. 200020115864/1) and the European Office of Aerospace Research and Development (Grant FA8655-07-1-30310) and is part of the European Union project "Molecular Universe" (MRTN-CT-2004-512303).

## References and Notes

- (1) Ziurys, L. M.; Apponi, A. J.; Guelin, M.; Cernicharo, J. *Astrophys. J.* **1995**, *445*, L47.
- (2) Herbig, G. H. *Annu. Rev. Astron. Astrophys.* **1995**, *33*, 19.
- (3) Douglas, A. E. *Nature* **1977**, *269*, 130.
- (4) Maier, J. P.; Walker, G. A. H.; Bohlender, D. A. *Astrophys. J.* **2004**, *602*, 286.
- (5) Apetrei, C.; Ding, H.; Maier, J. P. *Phys. Chem. Chem. Phys.* **2007**, *9*, 3897.
- (6) Corlett, G. K.; Little, A. M.; Ellis, A. M. *Chem. Phys. Lett.* **1996**, *249*, 53.
- (7) Tokaryk, D. W.; Adam, A. G.; Hopkins, W. S. *J. Mol. Spectrosc.* **2005**, *203*, 54.
- (8) Dick, M. J.; Sheridan, P. M.; Wang, J. G.; Bernath, P. F. *J. Mol. Spectrosc.* **2005**, *233*, 197–202.
- (9) Marr, A. J.; Perry, J.; Steimle, T. C. *J. Chem. Phys.* **1995**, *103*, 3861.
- (10) Apponi, A. J.; Brewster, M. A.; Ziurys, L. M. *Chem. Phys. Lett.* **1998**, *298*, 161.
- (11) Grotjahn, D. B.; Apponi, A. J.; Brewster, M. A.; Xin, J.; Ziurys, L. M. *Angew. Chem., Int. Ed.* **1998**, *37*, 2678.
- (12) Xin, J.; Ziurys, L. M. *Astrophys. J.* **1998**, *501*, L151.
- (13) Ding, H.; Apetrei, C.; Chacaga, L.; Maier, J. P. *Astrophys. J.* **2008**, *627*, 348.
- (14) Huber, K. P.; Herzberg, G. *Constants of diatomic molecules*; Van Nostrand-Rheinhold: Princeton, 1979.
- (15) Rubino, R.; Williamson, J. M.; Miller, T. A. *J. Chem. Phys.* **1995**, *103*, 5964.
- (16) Wright, R. R.; Miller, T. A. *J. Mol. Spectrosc.* **1999**, *194*, 219.
- (17) Herzberg, G. *Spectra of Diatomic Molecules*; Van Nostrand-Rheinhold: New York, 2nd ed., 1950.
- (18) Western, C. M. *PGOPHER, a Program for Simulating Rotational Structure*; University of Bristol, 2007; <http://pgopher.chm.bris.ac.uk>.
- (19) Woon, D. E. *Chem. Phys. Lett.* **1997**, *274*, 299.
- (20) Ding, H.; Schmidt, T. W.; Pino, T.; Boguslavskiy, A. E.; Güthe, F.; Maier, J. P. *J. Chem. Phys.* **2003**, *119*, 814.
- (21) Petrie, S.; Kagi, E.; Kawaguchi, K. *Mon. Not. R. Astron. Soc.* **2003**, *343*, 209.
- (22) Kawaguchi, K.; Kagi, E.; Hirano, T.; Takano, S.; Saito, S. *Astrophys. J.* **1993**, *406*, L39.
- (23) Ziurys, L. M.; Savage, C.; Highberger, J. L.; Apponi, A. J.; Guelin, M.; Cernicharo, J. *Astrophys. J.* **2002**, *564*, L45.
- (24) Cernicharo, J.; Guelin, M. *Astron. Astrophys.* **1987**, *183*, L10.
- (25) Ziurys, L. M.; Apponi, A. J.; Philips, T. G. *Astrophys. J.* **1994**, *433*, 729.
- (26) Cherchneff, I.; Glassgold, A. E. *Astrophys. J.* **1993**, *419*, L41.
- (27) Jenniskens, P.; Desert, F. X. *Astron. Astrophys.* **1994**, *106*, 39.

JP803969A

## Chapter 8

# Rotationally resolved $A^2\Pi - X^2\Sigma^+$ electronic transition of $\text{MgC}_4\text{D}$

Magnesium containing species such as  $\text{MgCN}$  have been identified in the circumstellar envelopes of carbon rich stars through pure rotational spectroscopy.[96] Because of this astrophysical interest magnesium capped carbon chains have been the topic of many recent spectroscopic studies, including both  $\text{MgCH}_3$  and  $\text{MgCCH}$  in the mm-wave.[97, 98] The first assigned electronic gas phase spectrum of a magnesium chain species dates back to 1996, when laser induced fluorescence studies reported the  $A^2\Pi - X^2\Sigma^+$  origin band of  $\text{MgCCH}$ . [99] In subsequent studies bands due to  $\text{MgC}_4\text{H}$  and  $\text{MgC}_6\text{H}$  were observed.[100, 101] However, the  $\text{MgC}_4\text{D}$  isotope has not been studied spectroscopically so far. In this note the line positions and a rotational analysis for the origin band of the  $A^2\Pi - X^2\Sigma^+$  transition of this molecule are presented.

The  $\text{MgC}_4\text{D}$  radicals were generated in a plasma expansion through laser ablation of a magnesium rod in the presence of 0.1% DCCD in argon. Laser induced fluorescence was used to observe the species with a Nd:YAG pumped dye laser ( $0.08\text{ cm}^{-1}$ ) used for excitation with a wavemeter allowing for frequency calibration. The fluorescence signal was collected by an  $f/1$  lens and detected using a photomultiplier tube and a digital oscilloscope.

Figure 1 shows the  $\Omega = \frac{3}{2}$  spin orbit component for the origin band of the  $A^2\Pi - X^2\Sigma^+$  transition in  $\text{MgC}_4\text{D}$ , with the observable line assignments provided above. This

is located  $37\text{ cm}^{-1}$  to the blue of the accompanying  $\Omega = \frac{1}{2}$  portion (not shown), allowing the determination of the spin orbit splitting,  $A_{SO}$ , in the upper  $A^2\Pi$  state. Also observed in Figure 1 are two features assigned as the lesser abundant isotopic species  $^{25}\text{MgC}_4\text{D}$  (10%) and  $^{26}\text{MgC}_4\text{D}$  (11%), labeled with a bullet and diamond, respectively.

As with  $\text{MgC}_4\text{H}$ , the profile of the band resembles that expected from a  $A^2\Pi - X^2\Sigma^+$  transition.[101] For  $\text{MgC}_4\text{D}$ , the strong bandheads in the  $A^2\Pi_{1/2} - X^2\Sigma^+$  spin component are  $Q_{12}$  and  $P_{11}$ , while for the  $A^2\Pi_{3/2} - X^2\Sigma^+$  spin component they are  $Q_{22}$  and  $P_{22}$ . [78] Stretching out to the blue are the  $R_{11}/R_{12}$  and  $R_{21}/R_{22}$  branches for the  $\Omega = \frac{1}{2}$  and  $\frac{3}{2}$  components, indicating that  $B' > B''$ . Reasonable peak separation in the  $R_{11}$  and  $R_{21}$  branches, on the order of  $3B$ , allow an assignment of the these two series at the given resolution of  $0.07\text{ cm}^{-1}$ .

A combined analysis of the two spin orbit bands with 50 lines provides a determination of the rotational parameters. The analysis of the data was performed using the PGopher program.[79] Line assignments were made by comparing the observed spectral lines with those calculated. The frequencies were fitted with an effective Hamiltonian for a  $^2\Pi - ^2\Sigma^+$  transition in a linear molecule, where both spin-orbit components in the excited state were considered simultaneously. The band origin, spin orbit constant and rotational values were varied while the temperature was held at 50 K and a linewidth fixed at  $0.07\text{ cm}^{-1}$ . Line positions, assignments, and the fit residuals are given in Table 1. The resulting spectroscopic constants are listed in Table 2, compared with those derived from the nondeuterated species.[101] One notices that in both the case of the deuterated and nondeuterated species, the reported rotational constants increase by approximately 2.65% upon excitation (2.5 and 2.8% for  $\text{MgC}_4\text{D}$  and  $\text{MgC}_4\text{H}$ , respectively), allowing further confidence in the derived fit. This observed increase in rotational constant reflects a decrease in the overall length of the chain upon electronic excitation.

While this observation of the lesser abundant isotopic species allows an assignment of their origin location and excited state spin-orbit splitting, their weak intensities and overlapping features precludes a proper rotational analysis for these minor constituents. A least squares fit for the two species was not attempted due to the weakness of their overlapping features. Table 3 summarizes the data concerning the origin band values and

spin orbit constants obtained for the three isotopomers studied.

Table 8.1: Observed rotational lines (in  $\text{cm}^{-1}$ ) of the origin band in the  $A^2\Pi - X^2\Sigma^+$  electronic transition of  $^{24}\text{MgC}_4\text{D}$ . The uncertainty of the  $\tilde{\nu}_{\text{obs}}$  values given is judged to be  $\pm 0.007 \text{ cm}^{-1}$ .

$J$	$A^2\Pi_{1/2} - X^2\Sigma^+$ R <sub>11</sub> Branch		$A^2\Pi_{3/2} - X^2\Sigma^+$ R <sub>21</sub> Branch	
	$\tilde{\nu}_{\text{obs}}$	$\tilde{\nu}_{\text{obs}} - \tilde{\nu}_{\text{calc}}$	$\tilde{\nu}_{\text{obs}}$	$\tilde{\nu}_{\text{obs}} - \tilde{\nu}_{\text{calc}}$
7.5	22419.514	-0.008		
8.5	22419.686	0.007		
9.5	22419.848	0.010	22456.753	-0.002
10.5	22420.002	0.023	22456.929	0.013
11.5	22420.184	0.021	22457.059	-0.024
12.5	22420.331	0.002	22457.252	-0.002
13.5	22420.516	0.018	22457.423	-0.002
14.5	22420.670	0.002	22457.604	0.006
15.5	22420.862	0.021	22457.782	0.007
16.5	22421.017	0.002	22457.937	-0.017
17.5	22421.194	0.002	22458.146	-0.005
18.5	22421.368	-0.004	22458.298	-0.021
19.5	22421.535	-0.018	22458.510	0.005
20.5	22421.743	0.006	22458.681	-0.013
21.5	22421.897	-0.026	22458.882	-0.003
22.5	22422.091	-0.020	22459.067	-0.011
23.5	22422.308	0.007	22459.285	0.011
24.5	22422.486	-0.008	22459.473	0.002
25.5	22422.678	-0.010	22459.655	-0.019
26.5	22422.898	0.013	22459.907	0.030
27.5	22423.087	0.003	22460.093	0.010
28.5	22423.279	-0.007	22460.304	0.013
29.5	22423.477	-0.012	22460.495	-0.007
30.5	22423.695	0.002	22460.702	-0.013
31.5	22423.900	-0.003	22460.962	0.032
32.5			22461.149	0.002
33.5			22461.375	0.006

Table 8.2: Constants determined from the analysis of the electronic spectrum of  $^{24}\text{MgC}_4\text{D}$ , compared with values obtained for  $^{24}\text{MgC}_4\text{H}$  (Ref. [101]). Values in parentheses denote the  $2\sigma$  standard deviation from the fit.

Parameter	$^{24}\text{MgC}_4\text{D}$		$^{24}\text{MgC}_4\text{H}$	
	$X^2\Sigma^+$	$A^2\Pi$	$X^2\Sigma^+$	$A^2\Pi$
$T_0 / \text{cm}^{-1}$		22436.735(8)		22431.978(7)
$B / \text{cm}^{-1}$	0.04576(12)	0.0469(10)	0.04619(19)	0.04748(20)
$A / \text{cm}^{-1}$		36.982(8)		36.964(3)

Table 8.3: Origin band wavenumbers and spin orbit constants for the  $A^2\Pi - X^2\Sigma^+$  transition in the  $\text{MgC}_4\text{D}$  isotopomers.<sup>a</sup>

	<sup>24</sup> MgC <sub>4</sub> D	<sup>25</sup> MgC <sub>4</sub> D	<sup>26</sup> MgC <sub>4</sub> D
$T_0 / \text{cm}^{-1}$	22436.735(8)	22436.30(7)	22435.87(7)
$A / \text{cm}^{-1}$	36.982(8)	36.93(7)	36.92(7)

<sup>a</sup>Constants obtained for <sup>25</sup>MgC<sub>4</sub>D and <sup>26</sup>MgC<sub>4</sub>D from measurement of the band head positions and not from a rotational analysis.

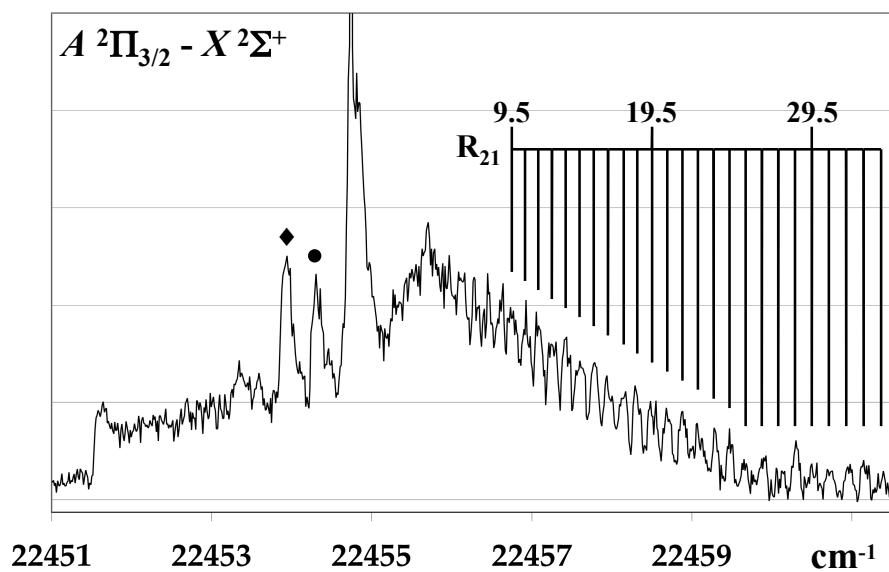


Figure 8.1: The observed  $\Omega = \frac{3}{2}$  component of the origin band in the  $A^2\Pi - X^2\Sigma^+$  electronic spectrum of  $\text{MgC}_4\text{D}$  measured using laser induced fluorescence in a supersonic molecular beam. The main peak is assigned to the most abundant isotopomer,  $^{24}\text{MgC}_4\text{D}$ , with  $^{25}\text{MgC}_4\text{D}$  and  $^{26}\text{MgC}_4\text{D}$  denoted by a  $\bullet$  and  $\diamond$ , respectively.



# Bibliography

- [1] A.E. Douglas. *Nature*, 269:130, 1977.
- [2] D. K. James and J. M. Tour. *Curr. Chem.*, 257:33, 2005.
- [3] H. Ding, A. E. Bogulavskiy, T. W. Schmidt, and J. P. Maier. *Chem. Phys. Lett.*, 392:255, 2004.
- [4] X. Cui, A. Primak, X. Zarate, J. Tomfohr, O. F. Sankey, A. L. Moore, T. A. Moore, D. Gust, G. Harris, and S. M. Lindsay. *Science*, 294:571, 2001.
- [5] R. M. Mezger. *Acc. Chem. Res.*, 32:952, 1999.
- [6] <http://www.nobel.se/chemistry/laureates/2000/index.html>.
- [7] P. Loubeyze, F. Occelli, and R. LeToullec. *Nature*, 416:613, 2002.
- [8] J.H. Hsu, M. Hayashi, S.H. Lin, W. Fann, L. J. Rothberg, G. Y. Perng, and S.A. Chen. *J. Phys. Chem.*, B 106:8582, 2002.
- [9] M. D. Morse. *Chem. Rev.*, 86:1049, 1986.
- [10] M.M. Kappes. *Chem. Rev.*, 88:369, 1988.
- [11] H. Ding, T.W. Schmidt, T. Pino, A.E. Boguslavskiy, F. Güthe, and J.P. Maier. *J. Chem. Phys.*, 119:814, 2003.
- [12] A. Denisov, T. W. Schmidt, A. E. Bogulavskiy, M. Araki, and J. P. Maier. *J. Mass. Spectrom.*, 233:131, 2004.
- [13] C.Y. Cha, G. Ganteför, and W. Eberhardt. *J. Chem. Phys.*, 100:995, 1994.

- [14] G. Ganteför, H.R. Siekmann, H.O. Lutz, and K.H. Meiwes-Broer. *Chem. Phys. Lett.*, 165:293, 1990.
- [15] X. Li, H. Wu, X.B. Wang, and L.S. Wang. *Phys. Rev. Lett.*, 81:1909, 1998.
- [16] L. Spitzer. *Physical Processes in the Interstellar Medium*. J. Wiley & Sons, Inc., 1978.
- [17] P. Moore. *The Guinness book of astronomy facts and feats*. Guinness World Records, 1992.
- [18] W.W. Morgan P.C. Keenan. *Ann. Rev. Astron. Astrophys.*, 11:29, 1973.
- [19] H. Karttunen, P. Kroger, H. Oja, M. Poutanen, and K. J. Donner. *Fundamental Astronomy*. Springer Verlag, Berlin, 1994.
- [20] C. Leinert and E.Gruen. *Phys. Chem. Space.*, page 204, 1990.
- [21] *The Messier Catalog: Diffuse Nebulae*. University of Illinois SEDS, 2007.
- [22] F. H. Shu. *The Physical Universe*. University Science Books. Mill Valley, California, 1982.
- [23] S. McMillan E. Chaisson. *Astronomy: a beginner's guide to the universe*. Benjamin-Cummings Pub. Co., 1995.
- [24] M. Morris R. Sahai, C. S. Contreras. *Astrophys. J.*, 620:948, 2005.
- [25] G.H. Herbig. *Ann. Rev. Astron. Astrophys.*, 11:309, 1973.
- [26] S.P. Theodore. *Mol. Biomol. Spectrosc.*, 57:615, 2001.
- [27] P.W. Merrill. *Publ.Astr.Soc.Pac.*, 46:206, 1934.
- [28] P.W. Merrill. *Publ.Astr.Soc.Pac.*, 86:174, 1937.
- [29] R. Lallement, P. Bertin, E. Chassefiere, and N. Scott. *Astron. Astrophys.*, 86:174, 1937.

- [30] G.H. Herbig. *Astrophys. J.*, 271:734, 1993.
- [31] S.O. Tuairisg, J. Cami, B.H. Foing, P. Sonnentrucker, and P. Ehrenfreund. *Ast. Astrophys. Suppl.*, 142:225, 2000.
- [32] G.H. Herbig. *Ann. Rev. Astron. Astrophys.*, 33:19, 1995.
- [33] J. Krelowski, C. Sneden, and D. Hiltgen. *Planet. Sci.*, 43:1195, 1995.
- [34] C. S. Beals and G. H. Blanchet. *Publ.Astr.Soc.Pac.*, 49:224, 1937.
- [35] N.L.J. Cox, L. Kaper, B.H. Foing, and P. Ehrenfreund. *Astron. Astrophys.*, 438:187, 2005.
- [36] G. Wallerstein, K. Sandstrom, and R. Gredel. *Publ.Astr.Soc.Pac.*, 119:1268, 2007.
- [37] P. Jenniskens, P. Ehrenfreund, and F. X. Desert. *Astron. Astrophys.*, 256:1, 1992.
- [38] R.L. Snell and P.A. Van den Bout. *Astrophys. J.*, 244:844, 1981.
- [39] I. Porceddu, P. Benvenuti, and J. Krelowski. *Astron. Astrophys.*, 260:391, 1992.
- [40] T.J. Deeming and G.A.H. Walker. *Z. Astrophys.*, 66:175, 1992.
- [41] J. Krelowski. *Astron. Nach.*, 4:255, 1988.
- [42] J. Krelowski and G.A. Walker. *Astrophys. J.*, 312:860, 1987.
- [43] J.A. Thorburn, L.M. Hobbs, B.J. McCall, T. Oka, D. E. Welty, S.D. Friedman, T.P. Snow, P. Sonnentrucker, and D.G. York. *Astrophys. J.*, 584:339, 2003.
- [44] P.R. Shapiro and A.G.G.M. Tielens. *Int. Astron. Union Coll.*, 137:253, 1995.
- [45] J. Krelowski. *Adv. Space Res.*, 30:1395, 2002.
- [46] P.J. Sarre. *Nature.*, 351:356, 1991.
- [47] P.J. Sarre, J. R. Miles, T.H. Kerr, R.E. Hibbins, S.J. Fossey, and W. B. Somerville. *Astr. Soc.*, 277:41, 1995.

- [48] J. Fulara, M. Jakobi, and J. P. Maier. *Chem. Phys. Lett.*, 206:203, 1993.
- [49] P. Freivogel, J. Fulara, and J. P. Maier. *Astrophys. J.*, 431:151, 1994.
- [50] T. Motylewski, H. Linnartz, O. Vaizert, J. P. Maier, G. A. Galazutdinov, F. A. Musaev, J. Krelowski, G. A. H. Walker, and D. A. Bohlender. *Astrophys. J.*, 531:312, 2000.
- [51] A. Leger and J. Puget. *Astron. Astrophys.*, 137:L5, 2002.
- [52] V. Wakelam and E. Herbst. *Astrophys. J.*, 680:371, 2008.
- [53] F. Boulanger, E. Falgarone, J.L. Puget, and G. Helou. *Astrophys. J.*, 364:136, 2008.
- [54] C. Joblin M. Rapacioli and P. Boissel. *Astron. Astrophys.*, 429:193, 2005.
- [55] F. Salama, E. L. O. Bakes, L. J. Allamandola, and A. G. G. M. Tielens. *Astrophys. J.*, 458:621, 1996.
- [56] K. Sellgren. *Mol. Biomol. Spectrosc.*, 57:627, 2001.
- [57] Z. Gasyna, P.M. Schatz, J. P. Hare, T. J. Dennis, H. W. Kroto, R. Taylor, and D. R. M. Walton. *Chem. Phys. Lett.*, 183:238, 1991.
- [58] J. Fulara, M. Jakobi, and J. P. Maier. *Chem. Phys. Lett.*, 211:227, 1993.
- [59] A. Leger, L. DHendecourt, L. Verstraete, and W. Schmidt. *Astron. Astrophys.*, 203:145, 1988.
- [60] B.H. Foing and P. Ehrenfreund. *Astron. Astrophys.*, 317:L59, 1997.
- [61] M. Guelin, J. Cernicharo, C. Kahane, and J. Gomezgonzalez. *Astron. Astrophys.*, 157:L17, 1986.
- [62] M. Anderson and L.M. Ziurys. *Astrophys. J.*, 452:L157, 1993.
- [63] F.X. Sunahory and D.J. Clouthier J. Wei. *J. Am. Chem. Soc.*, 129:960, 2007.

- [64] N. Oliphant, A. Lee, P.F. Bernath, and C.R. Brasier. *J. Chem. Phys.*, 92:2244, 1990.
- [65] H. Abe, M. Mukai, M. Fujitake, and N. Ohashi. *J. Mol. Spectrosc.*, 195:317, 1999.
- [66] A.J. Schoeffler, H. Koguchi, K. Hoshima, Y. Ohshima, and Y. Endo. *J. Chem. Phys.*, 114:6142, 2001.
- [67] Y. Sumiyoshi, T. Ueno, and Y. Endo. *J. Chem. Phys.*, 119:1426, 2003.
- [68] E. Chasovskikh, E.B. Jochnowitz, E. Kim, and J.P. Maier. *J. Phys. Chem.*, 111:11986, 2007.
- [69] D.L. Michalopoulos, M.E. Geusic, P.R.R. Langridge-Smith, and R.E. Smalley. *J. Chem. Phys.*, 80:3556, 1984.
- [70] Y. Ohshima and Y. Endo. *J. Mol. Spectrosc.*, 153:627, 1992.
- [71] A. Vogel and V. Venugopalan. *Chem. Rev.*, 103:577, 2003.
- [72] R.F. Wood D.B. Geohegan J.M. Donato C.L. Liu K.R. Chen, J.N. Leboeuf and A.A. Puretzky. *Phys. Rev. Lett.*, 75:4706, 1995.
- [73] A.D. Sappey and T.K. Gamble. *App. Phys.*, 72:5095, 1992.
- [74] A.A. Puretzky and D. B. Geohegan. *Phys. Rev.*, 65:245425, 2002.
- [75] G Bollen P.A. Lofy J. Ottarson D. A. Davies, D. J. Morrissey and S. C. Schwarz. *J. Phys.*, 59:136, 2007.
- [76] M. Jugroot and B.A. Collings. *App. Phys.*, 37:1289, 2004.
- [77] A. Kantrowitz and J. Grey. *Rev. Sci. Instr.*, 22:333, 1951.
- [78] G. Herzberg. *Molecular Spectra and Molecular Structure. I. Spectra of Diatomic Molecules*. D. van Nostrand, 1950.
- [79] PGOPHER, a Program for Simulating Rotational Structure, C. M. Western, University of Bristol.

- [80] K. S. Kini and M. I. Savadatti. *J. Phys.*, 10:1977, 2004.
- [81] D. H. Levy R. E. Smalley, B. L. Ramakrishna and L. Wharton. *J. Chem. Phys.*, 61:4363, 1974.
- [82] Lagerqvist L. Gausset, G. Herzberg. and B. Rose. *Discuss. Faraday Soc.*, 35:113, 1963.
- [83] K. Aiuchi and K. Shibuya. *J. Mol. Spectrosc.*, 209:92, 2001.
- [84] C.R. Brazier. *J. Chem. Phys.*, 98:2790, 1993.
- [85] J.D. Watts, J. Gauss, and R.J. Barlet. *J. Chem. Phys.*, 98:8718, 1993.
- [86] A.D. Becke. *J. Chem. Phys.*, 98:5648, 1993.
- [87] D.E. Woon and T.H. Dunning. *J. Chem. Phys.*, 98:1358, 1993.
- [88] X. Zheng, Z. Wang, and A. Tang. *J. Phys. Chem.*, 103:9275, 1999.
- [89] P.J. Knowles H.J. Werner. *J. Chem. Phys.*, 82:5053, 1985.
- [90] H.J. Werner and P.J. Knowles. *J. Chem. Phys.*, 89:5803, 1988.
- [91] M.J. Frish, G.W. Trucks, H.B. Schlegel, G.E. Scuseria... GAUSSIAN 98 (revision a.7) gaussian Inc.(1998) Pittsburg P.A.
- [92] Molpro is a package of ab initio programs written by H.J. Werner and P. J. Knowles and R. Lindh and F. R. Manby and M. Schutz and P. Celani and T. Korona and G. Rauhut and R. D. Amos and A. Bernhardsson and A. Berning and D. L. Cooper and M. J. O. Deegan and A. J. Dobbyn and F. Eckert and C. Hampel and G. Hetzer and A. W. Lloyd and S. J. McNicholas and W. Meyer and M. E. Mura and A. Nickla and P. Palmieri and R. Pitzer and U. Schumann and H. Stoll and A. J. Stone and R. Tarroni and T. Thorsteinsson.,.
- [93] W.C. Wiley and I.H. McLaren. *Rev. Sci. Inst.*, 26:1150, 1955.

- [94] J. L. Highberger L. M. Ziurys, C. Savage and A. J. Apponi. *Astrophys. J. Lett.*, 564:L45, 2006.
- [95] H. Ding C. Apetrei and J. P. Maier. *Phys. Chem. Chem. Phys.*, 9:3897, 2007.
- [96] L. M. Ziurys, A. J. Apponi, M. Guelin, and J. Cernicharo. *Astrophys. J.*, 445:L47, 1995.
- [97] M. A. Anderson and L. M. Ziurys. *Astrophys. J.*, 439:L25, 1995.
- [98] M. A. Anderson and L. M. Ziurys. *Astrophys. J.*, 452:L157, 1995.
- [99] G. K. Corlett, A. M. Little, and A. M. Ellis. *Chem. Phys. Lett.*, 249:53, 1996.
- [100] H. Ding, C. Apetrei, L. Chacaga, and J. P. Maier. *Astrophys. J.*, 627:348, 2008.
- [101] E. Chasovskikh, E. B. Jochnowitz, and J. P. Maier. *J. Phys. Chem. A*, 112:8686, 2008.

# Egor A. Chasovskikh

---

## Work:

Institut für Physikalische Chemie  
Klingelbergstrasse 80  
Universität Basel  
CH-4056 Basel  
Switzerland

## Home:

Bärenfelsenstr 9  
CH-4057 Basel

Home: +41 76 572 75 11

Office: +41 61 267 38 14

Egor.Chasovskikh@unibas.ch

born on September 27, 1978

Russian Federation citizen, single

## Education

Universität Basel

*Ph.D. in physical chemistry*

*Thesis title:* Electronic spectra of metal terminated carbon chains.

*Supervisor:* Prof. Dr. J.P. Maier

Basel, Switzerland

*Jun. 2004 – Dec. 2008*

Novosibirsk State University

*M.Sc. in physics*

(specialization in nonequilibrium processes)

*Thesis title:* The study of arc discharge thermophysical properties in a double transferred arc torch with molten metal electrodes.

*Supervisor:* Prof. Dr.M.Predtechensky

Novosibirsk, Russia

*Jun. 2001 - 1. Jul. 2003*

Novosibirsk State University

*B.A. in physics*

Novosibirsk, Russia

*Sept.1995 – 2. Jun. 2001*

## Research Experience

Universität Basel

*Ph.D. Research*

Measured the electronic spectra of astrophysically relevant molecules using laser based methods, including Laser Induced Fluorescence, Resonant 2-color 2-photon Ionization, and Cavity Ring Down Spectroscopy. Laser Ablation and electrical discharge sources allowed the synthesis of various unstable and transient species. The research was conducted under the supervision of Prof. Dr. John P. Maier, F.R.S.

Basel, Switzerland

*Jun. 2004 – Dec. 2008*

Novosibirsk State University

*Master's Research*

Work was devoted to the experimental investigation of arc discharge thermophysical properties in double transferred arc torch (DTAT). Experiments were conducted on a prototype plasma chemical reactor with the capacity of 200kW. The dependencies of voltampere characteristics on the properties and parameters on the flow of plasma forming gas were obtained.

Novosibirsk, Russia

*Jun. 2001 - Jul. 2003*



Novosibirsk State University  
*Undergraduate Research*

Novosibirsk, Russia  
*Sept. 1995 – Jun. 2001*

Investigate the vapor pressure, density and P-V-T properties of heptafluoropropane (R227ea), using a gamma densitometer.

## **Teaching Experience**

Universität Basel

*Jun. 2004 – Dec. 2008*

*Teaching assistant in 'physical chemistry practicum' with undergraduate students.*

## **Other Skills**

LabView, SolidWorks, GaussView, Molden, C++, Linux

## **Languages**

Russian (*native*), English (*fluent*)

## References

Prof. Dr.  
J. P. Maier, F.R.S.  
Universität Basel  
Inst. für phys. Chemie  
Klingelbergstrasse 80  
CH-4056 Basel  
Switzerland  
Tel: +41 61 267 38 26  
j.p.maier@unibas.ch

Prof. Dr.  
Alan Knight  
Griffith Chemistry

Brisbane,  
Australia  
Tel: +61 7 3875 7478  
A.Knight@griffith.edu.au

## Publications

Vibronic analysis of the  $\tilde{C}^2B_2 - \tilde{X}^2A_1$  band system of  $AlC_2$  C.Apetrei, **E. Chasovskikh**, E. B. Jochnowitz, H. Ding, A. E. Knight, and J. P. Maier. J. Phys. Chem. A (2008) In Preparation.

The Electronic Spectrum of the  $MgC_4H$  Radical. **E. Chasovskikh**, E. B. Jochnowitz, and J. P. Maier. J. Phys. Chem. A (2008) Submitted.

Electronic Spectrum of the  $AlC_2$  Radical. **E. Chasovskikh**, E. B. Jochnowitz, and J.P. Maier. J. Phys. Chem. A 111 (2007) 11986